

University of Nottingham
UK | CHINA | MALAYSIA

Engineering the Interactions and Dynamics of Ultracold Atom Gases

Submitted in Nov 2020, in partial fulfillment of
the conditions for the award of the degree **PhD Physics.**

Yijia Zhou
14284238

Supervised by Prof. Mark Fromhold
Dr Weibin Li

School of Physics and Astronomy
University of Nottingham

I hereby declare that this thesis is all my own work, except as indicated in the text.

Signature _____

Date _____ / _____ / _____

I hereby declare that I have all necessary rights and consents to publicly distribute this thesis via the University of Nottingham's e-Theses archive.

Abstract

Ultracold atoms are used to study various fundamental physics, including many-body system, nonequilibrium dynamics, and find many applications in quantum computing and quantum sensing. In this thesis, we studied the dynamics of ultracold atom gases with controllable two-body interactions. One of the major concerns is to manipulate the atomic states with electromagnetic fields. Here, we will show four projects associated with this topic.

The first project is about the Sagnac interferometer based on trapped Bose-Einstein condensate. We explored the dynamics of the atoms and their relation to the sensitivity. We came up with an optimised driving field, and the performance is examined with interactions taken into consideration.

The second project is about the quantum dynamics of bosonic atoms in an optical lattice with long-range interactions by Rydberg-dressing. It has been widely studied due to its controllable strength, length and anisotropy, which paves the new approach to engineering exotic quantum states and improving the performance of quantum devices. We found that phase transitions of Mott-insulator, superfluid supersolid, and density wave during a quench process. The correlation of the atoms is studied which reveals the properties of long-range interactions.

The third project shows new designs of the magneto-optical trap for atom cooling. They are proposed to be manufactured by 3D printing technology. We simulated their performance and optimised the geometric parameters. The time-response and impedance have also been analysed.

The fourth project studies the ground state of Rydberg-dressed fermions from the perspective of Fermi surface deformation. We calculated the deformation manifested by the aspect ratio and the appearance of Cooper pairs. The power-law scaling relations have been found with respect to the laser field, atom density and the quantum number of Rydberg states.

List of Publications

1. Y. Zhou, I. Lesanovsky, T. Fernholz, and W. Li, Controlling the dynamical scale factor in a trapped atom Sagnac interferometer, *Phys. Rev. A* **101**, 012517 (2020).

2. Y. Zhou, Y. Li, R. Nath, and W. Li, Quench dynamics of Rydberg-dressed bosons on two-dimensional square lattices, *Phys. Rev. A* **101**, 013427 (2020).

3. R. Saint, W. Evans, Y. Zhou, T. Barrett, T. M. Fromhold, E. Saleh, I. Maskery, C. Tuck, R. Wildman, F. Oručević, and P. Krüger, 3D-printed components for quantum devices, *Sci. Rep.* **8**, 8368 (2018).

4. Y. Zhou, N. Welch, R. Crawford, F. Oručević, F. Wang, P. Krüger, R. Wildman, C. Tuck, and T. M. Fromhold, Design of Magneto-Optical Traps for Additive Manufacture by 3D Printing, arXiv:1704.00430 (2017).

Acknowledgements

Firstly, I would like to express my deepest appreciation to my supervisors Prof. Mark Fromhold and Dr Weibin Li. They gave me the opportunity to study in Nottingham and are both very generous and supportive of my study. I feel that I have plenty of freedom to embrace the topics I am interested in, and I can always get their guidance when I feel lost.

Next, I would like to thank fellows at the University of Nottingham. I have learnt a lot from Prof. Igor Lesanovsky, Dr Thomas Fernholz, Dr Lucia Hackermüller, Prof. Ricky Wildman, Prof. Christopher Tuck, Dr Richard Campion, as well as their postdocs and students. They created an open and warm atmosphere for study. We have worked together with many outputs, which I hope can be carried on in the future.

I am also grateful to Dr Rejish Nath (IISER, Pune), Prof. Yongqiang Li, Dr Yanli Zhou (NUDT), Prof. Dong Yan (Changchun), Prof. Huaizhi Wu (Fuzhou), Prof. Lin Li, Prof. Yiqiu Ma (HUST), Prof. Yan Xue (Jilin), Dr Zhiping Wang (Anhui), Prof. Haibin Wu (ECNU), Prof. Saijun Wu (Fudan), Prof. Peter Kruger and Dr Fedja Oručević (Sussex). We had many fruitful discussions, and they provided a great amount of constructive suggestions for my research.

Then, I would like to extend my sincere thanks to my office mates and friends in Nottingham, Dr Zhengyang Bai, Dr Filippo Gambetta, Dr Matthew Jessop, Mr Gary McCormack, Dr Mark Greenaway, Dr Xuedong Tian, Dr Feiran Wang, Dr Rosemary Crawford, Dr Christopher Morley, Mr Michael Packer, Ms Hannah Coleman, Dr Nathan Welsh, Dr Nathan Cooper, Ms Vineetha Naniyil, Mr Fabio Gentile, Dr Reece Saint, Dr William Evans, Dr Ehab Saleh, Dr Ian Maskery and Dr Meisam Abdi. They are not only helpful to the academic problems, but also helped me a lot in daily life. It is not easy to live 10,000 km away from home, but they made me feel that there is nothing to worry about.

Finally, I would like to thank all of my friends who may not have academic contact with me, but definitely they encouraged me to be what I am.

2020 is a memorable year. While this thesis was being written up, the COVID-19 pandemic swept across the world. Until the date of submission, the numbers of infections and deaths are still hitting the record. It is undoubtedly that a scientific mindset is the key to a sustainable modern society. Hence, the value of pursuing a PhD is far more

than accomplishing a few projects and papers. An optimistic attitude towards the unknown things and a general concern of the human-nature relationship that developed during my study will ever last in my life.

In June, my grandfather passed away in peace. I was unable to stay with him due to the lock-down policies and the difficulty of international flights. I will regret this tragedy forever. My family has always been my staunch supporter, and I am aware that I can never do too much in return.

Contents

Abstract i

List of Publications ii

Acknowledgements iii

1 Introduction 1

2 Bose-Einstein Condensate of Ultracold Atoms 3

2.1 From Bose statistics to ultracold atoms . . . 3

2.2 Interacting Bose gas . . . 6

2.2.1 Gross-Pitaevskii equation . . . 6

2.2.2 Thomas-Fermi approximation . . . 8

2.2.3 Feshbach resonance . . . 8

2.2.4 Length scales of correlation and coherence . . . 10

2.2.5 Elementary excitation . . . 10

2.3 Bosons trapped in optical lattices . . . 11

2.3.1 Optical lattice . . . 12

2.3.2 Mott-insulator-superfluid transition . . . 13

2.3.3 Universal class . . . 16

2.3.4 Extended Bose-Hubbard model . . . 17

2.4 Beyond mean-field approximation . . . 17

3 Rydberg Interactions 19

3.1 Rydberg atom . . . 19

3.1.1 Alkali atom model . . . 20

3.1.2 Novel scaling relations . . . 21

3.2 Rydberg pair interaction . . . 23

3.2.1 Diagonalisation method . . . 24

3.2.2 Perturbation method . . . 25

3.2.3 Anisotropic interactions . . . 25

3.3 Rydberg dressing . . . 26

3.3.1 Rydberg-dressing schemes . . . 27
3.3.2 Rydberg-dressed interaction . . . 28

4 Project: Trapped Atomic Sagnac Interferometer 30
4.1 Sagnac effect . . . 31
4.2 BEC-based atomic Sagnac interferometer . . . 32
4.2.1 Pseudospin model . . . 32
4.2.2 Manipulating the internal state . . . 34
4.2.3 Dynamical scale factor and sensitivity . . . 35
4.3 Non-interacting BEC . . . 35
4.3.1 Analytical solution to the 1D model . . . 36
4.3.2 Analytical solution to the 2D model . . . 37
4.3.3 Optimisation of the driving field . . . 40
4.4 Interacting BEC . . . 41
4.4.1 Numerical solver for GPE . . . 41
4.4.2 Effects of interactions and asymmetric trap . . . 43

5 Project: Quench Dynamics of Extended Bose-Hubbard Model 46
5.1 Gutzwiller ansatz . . . 47
5.2 Phase diagram of the extended Bose-Hubbard model . . . 49
5.2.1 Roton instability . . . 50
5.3 Kibble-Zurek mechanism . . . 51
5.3.1 Novel power-law scalings . . . 52
5.3.2 Dynamics of superfluid fraction and density variance . . . 54
5.3.3 Vortex nucleation and Kibble-Zurek scaling . . . 55
5.4 Correlations in the quench process . . . 58
5.4.1 Correlation measurement and time-of-flight interference . . . 58
5.4.2 First-order correlation . . . 60
5.4.3 Second-order correlation . . . 61
5.4.4 Emergence of the density wave and supersolidity . . . 62

6 Project: Trapping Atoms with 3D Printing Technology 65
6.1 Magneto-optical trap . . . 66
6.2 New designs for 3D printing manufacture . . . 68
6.2.1 Twisted metal bars design . . . 69
6.2.2 Compact conductor design . . . 71
6.2.3 Two-piece conductor design . . . 74
6.3 Time response . . . 76
6.4 Experimental test . . . 78
6.5 Conclusion and discussions . . . 80

7 Project: Fermi Surface Deformation of Rydberg-Dressed Atoms **81**
7.1 Hartree-Fock-Bogoliubov approximation 81
7.2 Anisotropic Rydberg-dressed interaction 83
7.3 Ground state of ultracold ^{6}Li gas 83
7.3.1 Self-consistent approach 84
7.3.2 Scaling relations of the Fermi surface deformation 88
7.4 Discussions and outlook 89

8 Summary **90**

Appendices **92**

A Atomic Sagnac Interferometer **92**
A.1 1D case 92
A.2 2D case 94

B Quenched Bose-Hubbard Model **97**
B.1 Derivations for the E.O.M. of the coefficients of GWF 97
B.2 Derivations for correlation functions under GWF 98

C Hartree-Fock-Bogoliubov Approximation **102**

Bibliography **103**

List of Figures

2.1 Thomas-Fermi Approximation . . . 9
2.2 Feshbach Resonance . . . 9
2.3 Illustration of Wannier wave functions in optical lattice . . . 12
2.4 Phase Diagram of BHM . . . 15

3.1 Wave function of Rydberg states . . . 21
3.2 Decay rates of Rydberg state . . . 23
3.3 Rydberg pair interaction of ^{40}K . . . 24
3.4 Anisotropic C_6 parameter . . . 26
3.5 Rydberg-dressing scheme . . . 27
3.6 Rydberg-dressing level diagram . . . 28
3.7 Rydberg-dressed interaction . . . 29

4.1 Sketch of a Mach-Zehnder interferometer . . . 31
4.2 Sagnac Interferometer . . . 32
4.3 Demonstration of the dynamical scale factor . . . 39
4.4 Parametric optimisation of the driving function . . . 41
4.5 Wave functions of various interacting BECs on the ASI for interference 43
4.6 Dynamical scale factors of ASI with interactions . . . 44

5.1 Quench scheme . . . 46
5.2 Phase diagrams of the extended Bose-Hubbard Model . . . 50
5.3 Bogoliubov spectrum and roton instability . . . 51
5.4 Kibble-Zurek Mechanism . . . 52
5.5 Dynamics of superfluid fraction and density variance . . . 55
5.6 Vortex nucleation of quenched eBHM . . . 56
5.7 Quench dynamics for KZM . . . 56
5.8 Principle of time-of-flight interference. . . . 59
5.9 Time-of-flight snapshots at $Ut = 17.5$ . . . 62
5.10 Time-of-flight snapshots at $Ut = 28$ . . . 63
5.11 $n(k)$ and $C(q)$ for various LRIs . . . 63

6.1 Principle of Magneto-optical trap 66
6.2 Twisted metal bars design 70
6.3 Compact conductor design 72
6.4 Fields of compact conductor design 73
6.5 Two-piece conductor design 74
6.6 Fields of two-piece conductor design 75
6.7 Time response 77
6.8 Experiment outcome 79

7.1 C_6 parameters of ^{6}Li and ^{40}K for nS, nP, nD Rydberg states 84
7.2 Ratios of $C_6(0)/C_6(\pi/2)$ for ^{6}Li and ^{40}K 85
7.3 Examples of Fermi surface deformation of ^{6}Li 87
7.4 Aspect ratio and variance of the Fermi surface deformation for ^{6}Li under various dressing parameters 88

List of Tables

3.1 Scaling of several atomic quantities with respect to n^* for Rydberg states 22

Chapter 1

Introduction

Ultracold atoms are of great interest to physicists for their extraordinary properties. With the lowest temperature ever achieved, it is ideal for engineering many-body quantum states in a sizeable parametric space. This is not only an attractive feature for the studying of fundamental physics but also gives birth to numerous applications in quantum computing and quantum sensing. This thesis aims to probe the nature of interacting ultracold atoms by focusing on their dynamics.

The ultracold atoms can be loaded in a single or double well trap, a ring-shaped trap, or a periodic trap. The single-well harmonic trap is the simplest case but is suitable to unveil the interactions between atoms. The ring trap can be used for measuring external rotation by the Sagnac effect. The periodic trap realised by optical lattices is widely applied to mimic many-body physics in solid-state materials. The interactions are usually divided into short-range and long-range types. The former may come from the collision and scattering process. The latter can be caused by the dipole-dipole interactions, or excitation to Rydberg states.

Rydberg states are highly excited states with large orbital radius. Their use in experiments represents a significant advantage because both the interaction strength and length are controllable. One can also engineer the anisotropy of the interactions, which leads to exotic quantum states with angular dependency. It widely broadens the domain of ultracold atom-based quantum technologies.

In Chapter 2, I will present a review of some basic theories of Bose-Einstein condensates (BEC). I will focus on the interactions and dynamics of BECs and calculate the dynamics with the Gross-Pitaevskii equation. A BEC loaded on a standing wave of lasers gives rise to an optical lattice, which can be described by the Bose-Hubbard model. Its most important feature is the quantum phase transition between Mott-insulator and superfluid.

In Chapter 3, I will give a short review of Rydberg atoms and their interactions. The wave functions of Rydberg states are solved with the model potential, and various scaling relations can be derived. The interactions between a pair of Rydberg atoms, known

as the Rydberg pair interaction, are solved via diagonalisation and perturbation methods. Another type of interactions by Rydberg-dressing is also introduced, where the atoms are prepared in Rydberg-dressed states.

Chapter 4 is based on Ref. [1]. We investigated the dynamical scale factor of a Sagnac interferometer using trapped BECs. The dynamical scale factor is a key element of the sensitivity, and is determined by the motions of the atoms. We explored the dynamics analytically and numerically. The solutions inspired us to optimise the driving field for maximising the interference signal. We also examined the effects of interactions that potentially inhibit the best performance of the interferometer.

Chapter 5 is based on Ref. [2]. We explored the quantum dynamics of bosonic atoms in an optical lattice with long-range interactions obtained by Rydberg-dressing. The equilibrium phases include Mott-insulator, density wave, superfluid and supersolid. By quenching the lattice depth from the Mott-insulator phase, we found that the evolution of the system satisfies the Kibble-Zurek mechanism, and the emergence of superfluidity and supersolidity can be observed. The correlation in the system is also studied in the scenario of time-of-flight interference, which connects to the long-range interaction properties.

Chapter 6 is based on Ref. [3, 4]. We presented three designs of magneto-optical traps for atom cooling experiments, which can be realised by 3D printing technology. The idea starts with the skeleton structures followed by 3D modelling. The performance has been verified using finite element analysis with the optimised geometric parameters. One of the designs, capable of trapping $\sim 10^8$ atoms, has been printed and tested. The time-response and impedance under AC current have been analysed as well.

Chapter 7 is an ongoing project, where we explored the Fermi surface deformation of cold fermions with Rydberg-dressed interactions. Based on Hartree-Fock-Bogoliubov approximation, we found the deformation of the Fermi sphere and the appearance of Cooper pairs. The power-law scaling relations between the aspect ratio and density variance have been achieved numerically. Deeper understanding from the perturbative perspective will be carried out in our future work.

Chapter 2

Bose-Einstein Condensate of Ultracold Atoms

In this chapter, we will start with the concept of BEC, which plays a central role in cold atom physics. It is a novel state of matter which can be achieved at extremely low temperatures. It exhibits significant quantum coherence, so it is particularly valuable for the study of fundamental physical principles and manifests great potential to applications in quantum technology. It has been shown that BEC can help to study exotic behaviours in quantum optics [5, 6] and many-body physics [7, 8]. BEC-based matter-wave interferometers can be applied to create the next-generation of sensors for high-precision measurement [9, 10], or used for quantum information and computation [11]. Therefore, it is now a critical issue to understand the dynamics of BECs, how it is affected by the atomic interactions and how to control them.
This chapter is organised as follows. Section 2.1 will give a brief overview of BEC from a historical perspective, from the theoretical prediction in 1925 [12] to the realisation in ultracold atoms in 1995 [13–15]. Section 2.2 will introduce the role of short-range interactions in BEC, and then the mean-field description based on Gross-Pitaevskii equation. We will also mention the Feshbach resonance, which enables the scattering length to be tuned from $-\infty$ to $+\infty$ [16]. Section 2.3 will introduce optical lattices. They are very important platforms to mimic condensed matter physics and study quantum dynamics. Section 2.4 will introduce several methods beyond the mean-field approximation.

2.1 From Bose statistics to ultracold atoms

The BEC is one of the most fascinating phenomena in physics. It was predicted by Albert Einstein in calculating the statistical distribution of a monoatomic gas [12, 17, 18] following Nath Bose's *new approach* to the Planck's law of photons [19]. The BEC is a state of matter where a large fraction of bosons in an N-particle system occupy one of the single particle state at extremely low temperature. In the ultracold atoms, the BEC is on the premise that the off-diagonal long-range order (ODLRO) exists.

The underlying requirement to get a BEC is that the particles are identical and allowed to occupy the same states. This kind of particle is called boson. According to quantum mechanics, the wave function of a system of bosons must be symmetric. As a comparison, the particle with antisymmetric wave function is called fermion, which cannot occupy any single-state with two or more particles. The major difference between whether the multiplicative occupation is allowed or not plays an important role in their statistical behaviours, and the forbidden case is called the Pauli exclusion principle. The bosons follow Bose-Einstein statistics, and the fermions follow Fermi-Dirac statistics.

For thermal equilibrium states, the statistical observables can be all generated from the partition function $\mathcal{Z}$ [20]. For bosons in the grand canonical ensemble, where the system is connected to a heat bath with fixed temperature T and a particle bath with fixed chemical potential μ, $\mathcal{Z}$ reads

$$\mathcal{Z} = \prod_s \sum_{n_s=0}^{\infty} e^{-\beta n_s(\varepsilon_s-\mu)} = \prod_s \frac{1}{1-e^{-\beta(\varepsilon_s-\mu)}}, \tag{2.1}$$

where s denotes all the available states whose energy is ε_s, $\beta = 1/(k_B T)$ and n_s is the occupation in equilibrium. The Bose-Einstein distribution of a non-degenerate gas can be acquired by $n_s = -1/\beta\partial \ln \mathcal{Z}/\partial\varepsilon_s$, which yields

$$n_s = \frac{1}{e^{\beta(\varepsilon_s-\mu)}-1}. \tag{2.2}$$

For free bosons [1], we can replace s by momentum $\mathbf{k}$, and the dispersion relation $\varepsilon(\mathbf{k}) = \hbar^2|\mathbf{k}|^2/(2m)$, where m is the mass of the particle, gives rise to energetic degeneracy, or density of states, $a_\varepsilon = \Omega_d k^{d-1}(\partial\varepsilon/\partial k)^{-1}$. Here d is the dimension of the gas and Ω_d is the total solid angle. Specifically, $\Omega_1 = 2$, $\Omega_2 = 2\pi$, $\Omega_3 = 4\pi$, and generally $\Omega_d = 2\pi^{d/2}/\Gamma(d/2)$. In the normal phase, the particle number conservation determines the chemical potential such that

$$N = \int_0^\infty n_\varepsilon a_\varepsilon \mathrm{d}\varepsilon = \frac{\mathcal{V}}{\lambda_{\mathrm{th}}^d} g_{d/2}\left(e^{\frac{\mu}{k_B T}}\right), \tag{2.3}$$

where $\mathcal{V}$ is the mode volume, $\lambda_{\mathrm{th}} = h/\sqrt{2\pi m k_B T}$ is the thermal wavelength, d is the dimension and $g_\nu(z)$ is the Bose-Einstein function which is defined as

$$g_\nu(z) = \frac{1}{\Gamma(\nu)}\int_0^\infty \frac{x^{\nu-1}\mathrm{d}x}{z^{-1}e^x-1} = z + \frac{z^2}{2^\nu} + \frac{z^3}{3^\nu} + \cdots. \tag{2.4}$$

To resolve Eq. (2.3), one can notice that μ is a monotonic function of T. The zero

[1] Here "free bosons" means that we ignore the external trapping potential, and assume that the density of gas is homogeneous in real space. This represent an approximation for a system of N bosons contained in a certain volume $\mathcal{V}$.

point of μ is the critical temperature T_c, below which μ vanishes and Bose-Einstein condensation occurs. This happens at the special value $z = 1$ with $g_\nu(1) = \zeta(\nu)$ being the Riemann Zeta function. Accordingly, the critical temperature for a 3D gas is

$$T_c = \frac{h^2}{2mk_B}\left(\frac{N/\mathcal{V}}{\zeta(3/2)}\right)^{2/3}. \tag{2.5}$$

For a 2D gas, T_c is equal to 0, and in 1D it does not exist, which means that a free gas does not have BEC in low dimensions. Furthermore, other thermal quantities can be generated by $\mathcal{Z}$ as well. For a 3D gas, the internal energy is continuous around the critical temperature, but the specific heat is discontinuous, which suggests that the phase transition to BEC is of the second order.

Besides, we make a comparison with the case in which bosons are trapped in a harmonic trap $V(x,y,z) = \frac{1}{2}\hbar^2\omega_x^2x^2 + \frac{1}{2}\hbar^2\omega_y^2y^2 + \frac{1}{2}\hbar^2\omega_z^2z^2$, where ω_x, ω_y, ω_z are the trapping frequencies along with the three directions. The density of states is not strictly analytical, but has an asymptotic approximation for large energies $a_\varepsilon \approx \varepsilon^2/(2\hbar^3\omega_x\omega_y\omega_z)$. The critical temperature can be obtained via the same method, and the result is [21]

$$T_c = \frac{\hbar\omega_0}{k_B}\left(\frac{N}{\zeta(3)}\right)^{1/3}, \tag{2.6}$$

where $\omega_0 = \sqrt[3]{\omega_x\omega_y\omega_z}$. Note that it is different from that in free space, most notably the exponent. Similar critical temperatures exist in 2D, where $T_c = \hbar\omega_0/k_B[N/\zeta(2)]^{1/2}$, and in 1D, where $T_c = 0$.

To directly observe an atomic BEC had been a difficult task. After 70 years from its theoretical prediction, it has first been realised with laser cooling technology [22]. The main challenge is that T_c is extremely low. To have a qualitative impression, one can consider the air at room temperature and 1 atm pressure. Its density is approximately 10^{19} cm^{-3}, and according to Eq. (2.5), the critical temperature is ~ 1 mK, which is far below the boiling point of nitrogen gas (77 K). In practice, a dilute gas of alkali atoms under laser cooling can reach sub-micro Kelvin, but the density also drops to $\sim 10^{13}$ cm^{-3}. In this case, we can find that $T_c \sim 0.1$ μK, which is the temperature to realise the first atomic BEC [13].

The techniques and theories of laser cooling and trapping are many and varied [23, 24]. Here cooling refers to reducing the speed of atoms, and trapping refers to confining atoms in real space. The velocity-dependent interactions between light and atoms can slow down the motions of atoms due to the Doppler effect, and the cooling mechanism bounded by the balance of Doppler effect and recoils is known as Doppler cooling. However, the cooling limit can go below the Doppler limit when the details of the spatial properties of the light field are taken into consideration, as it happens for instance in the Sisyphus cooling (also called the polarisation gradient cooling). The overall cool-

ing mechanism can be summarised in the context of optical molasses. In the standard recipe, six orthogonal laser beams create a *molasses* area where atoms can be cooled down to mK or μK. The laser beams can also trap atoms due to the dipole force created by the gradient of the laser intensity. However, more efficient trapping can be acquired by a magnetic field via the Zeeman effect. The combination of a magnetic field and optical molasses gives birth to magneto-optical trap (MOT), which finally *confines* atoms in both real and momentum space. In Chapter 6, I will show some recent progress in designing new devices of MOT using 3D printing technology. It offers more possibility to transfer the laboratory experiments to industrial use.

However, MOT is still not enough to get a BEC. In order to hit the lowest temperature required for a BEC, usually one more step, known as evaporative cooling, is implemented. Here, the *hot* atoms, i.e., atoms in the highest energetic states, are released by lowering the height of the trap. This will also reduce the density of atoms along with T_c. Therefore, the evaporating process eventually makes only a few atoms prepared in a BEC state.

The idea of BEC had also been applied to explain other important phenomena. For example, the condensation of ^{4}He atoms gives rise to superfluidity, and the condensation of paired electrons (Cooper pair) gives rise to superconductivity [25]. This does not imply that BEC must lead to superfluidity or superconductivity. For example, ideal free bosons can be a BEC but not a superfluid. However, in general, quantum coherence in cold matter dominates various exotic many-body phenomena. The importance of studying cold atoms becomes thereby conspicuous: it bridges the gap of physics between few-body and many-body systems in the quantum world and paves the way to state-of-the-art applications in quantum technology.

2.2 Interacting Bose gas

The previous section provides a bird's-eye view of BEC from the perspective of an ideal gas, where interactions are ignored. In this section, I will give an overview of some essential features of an interacting Bose gas at zero temperature. I will focus on the short-range interaction and the corresponding dynamics which are related to my projects.

2.2.1 Gross-Pitaevskii equation

First of all, we consider the atomic gas being very dilute, such that the average spacing between particles, or mean free path, is much larger than any long-range interaction length scales of, e.g., van der Waals interaction. However, interactions may still exist when two atoms collide. Under this scenario, we can impose a model potential for

on-site (short-range) interactions, which reads [26]

$$V(\mathbf{r},\mathbf{r}') = g\delta(\mathbf{r}-\mathbf{r}'), \tag{2.7}$$

where g is the interaction strength. This will provide a (total) scattering cross-section σ together with scattering length a, and $\sigma = 4\pi a^2$ (for attractive interaction, $\sigma < 0$, and define $a < 0$). The relation between g and a can be derived from scattering theory and is given by

$$g = \frac{4\pi\hbar^2}{m}a. \tag{2.8}$$

The dynamics of non-interacting bosons is governed by the single-body Schrödinger equation. For interacting bosons with a δ-type model potential, we still look for a single-body evolution equation, which is known as the Gross-Pitaevskii equation (GPE). To derive the GPE, we start from the original Hamiltonian of the many-body system,

$$\begin{aligned}\hat{H} &= \int \mathrm{d}^3\mathbf{r}\hat{\psi}^\dagger(\mathbf{r})\hat{H}_0(\mathbf{r})\hat{\psi}(\mathbf{r}) + \frac{1}{2}\int \mathrm{d}^3\mathbf{r}\int \mathrm{d}^3\mathbf{r}'\hat{\psi}^\dagger(\mathbf{r})\hat{\psi}^\dagger(\mathbf{r}')V_{\mathrm{int}}(\mathbf{r}-\mathbf{r}')\hat{\psi}(\mathbf{r}')\hat{\psi}(\mathbf{r}) \\ &= \int \mathrm{d}^3\mathbf{r}\hat{\psi}^\dagger(\mathbf{r})\hat{H}_0(\mathbf{r})\hat{\psi}(\mathbf{r}) + \frac{g}{2}\int \mathrm{d}^3\mathbf{r}\hat{\psi}^\dagger(\mathbf{r})\hat{\psi}^\dagger(\mathbf{r})\hat{\psi}(\mathbf{r})\hat{\psi}(\mathbf{r}),\end{aligned} \tag{2.9}$$

where $\hat{H}_0(\mathbf{r}) = -(\hbar^2/2m)\nabla^2 + V_{\mathrm{ext}}(\mathbf{r})$ is the kinetic energy plus the external potential, $\hat{\psi}(\mathbf{r})$ is the bosonic field operator, whose commutation relation reads

$$\begin{aligned}\left[\hat{\psi}(\mathbf{r}),\hat{\psi}^\dagger(\mathbf{r}')\right] &= \delta(\mathbf{r}-\mathbf{r}'), \\ \left[\hat{\psi}(\mathbf{r}),\hat{\psi}(\mathbf{r}')\right] &= \left[\hat{\psi}^\dagger(\mathbf{r}),\hat{\psi}^\dagger(\mathbf{r}')\right] = 0.\end{aligned}$$

Then we use the Heisenberg equation to derive the equation of motion of $\hat{\psi}(\mathbf{r})$

$$\begin{aligned}&\mathrm{i}\hbar\frac{\partial}{\partial t}\hat{\psi}(\mathbf{r}) = \left[\hat{\psi}(\mathbf{r}),\hat{H}\right] \\ &= \int \mathrm{d}^3\mathbf{r}'\left\{\hat{\psi}^\dagger(\mathbf{r}')\left[\hat{\psi}(\mathbf{r}),\hat{H}_0(\mathbf{r}')\hat{\psi}(\mathbf{r}')\right] + \left[\hat{\psi}(\mathbf{r}),\hat{\psi}^\dagger(\mathbf{r}')\right]\hat{H}_0(\mathbf{r}')\hat{\psi}(\mathbf{r}')\right\} \\ &\quad + \frac{g}{2}\int \mathrm{d}^3\mathbf{r}'\left\{\hat{\psi}^\dagger(\mathbf{r}')\hat{\psi}^\dagger(\mathbf{r}')\left[\hat{\psi}(\mathbf{r}),\hat{\psi}(\mathbf{r}')\hat{\psi}(\mathbf{r}')\right] + \left[\hat{\psi}(\mathbf{r}),\hat{\psi}^\dagger(\mathbf{r}')\hat{\psi}^\dagger(\mathbf{r}')\right]\hat{\psi}(\mathbf{r}')\hat{\psi}(\mathbf{r}')\right\} \\ &= \int \mathrm{d}^3\mathbf{r}'\left\{\delta(\mathbf{r}-\mathbf{r}')\hat{H}_0(\mathbf{r}')\hat{\psi}(\mathbf{r}') + g\delta(\mathbf{r}-\mathbf{r}')\hat{\psi}^\dagger(\mathbf{r}')\hat{\psi}(\mathbf{r}')\hat{\psi}(\mathbf{r}')\right\} \\ &= \left(\hat{H}_0(\mathbf{r}) + g\hat{\psi}^\dagger(\mathbf{r})\hat{\psi}(\mathbf{r})\right)\hat{\psi}(\mathbf{r}).\end{aligned} \tag{2.10}$$

Finally, one can neglect the correlation of the last three-operator term and achieve the equation for the order parameter $\phi(\mathbf{r}) = \langle\hat{\psi}(\mathbf{r})\rangle$, which leads to the mean-field GPE,

$$\mathrm{i}\hbar\frac{\partial}{\partial t}\phi(\mathbf{r}) = \left(-\frac{\hbar^2}{2m}\nabla^2 + V_{\mathrm{ext}}(\mathbf{r}) + g\left|\phi(\mathbf{r})\right|^2\right)\phi(\mathbf{r}). \tag{2.11}$$

Here the order parameter is normalised to the total number of atoms, i.e., $\int |\phi(\mathbf{r})|^2 \mathrm{d}^3\mathbf{r} = N$. If $\phi(\mathbf{r})$ is normalised to 1 like an ordinary wave function, the interaction strength g should be multiplied by N, such that $g \to gN$, which reveals the bosonic enhancement of two-body interactions in a BEC.

2.2.2 Thomas-Fermi approximation

In general, the ground state of the GPE is different from that of the Schrödinger equation of non-interacting particles. The former can be obtained via a functional approach with the Gaussian ansatz [27]. However, if the interaction strength is strong enough, the Gaussian ansatz will fail as the shape of the ground state wave function deviates from the Gaussian function. In such a strongly interacting limit, the Thomas-Fermi approximation (TFA) is usually applied.

If the scattering interaction strength g is much larger than the kinetic energy, the derivative terms in Eq. (2.11) can be eliminated. Then the ground state can be obtained approximately from the identity

$$V_{\mathrm{ext}}(\mathbf{r}) + gn(\mathbf{r}) = \mu n(\mathbf{r}), \tag{2.12}$$

where $n(\mathbf{r}) = |\phi(\mathbf{r})|^2$ is the atom density. To avoid negative values, the solution outside the classical boundary $\mu < V_{\mathrm{ext}}(\mathbf{r})$ is trimmed off, and the final solution reads

$$n(\mathbf{r}) = \begin{cases} \frac{1}{g}\left[\mu - V_{\mathrm{ext}}(\mathbf{r})\right] & V_{\mathrm{ext}}(\mathbf{r}) \leqslant \mu \\ 0 & V_{\mathrm{ext}}(\mathbf{r}) > \mu \end{cases}. \tag{2.13}$$

Eq. (2.13) is known as the TFA [28, 29]. As an example, the density distributions of the ground states of an infinite square potential and a harmonic potential are plotted in Fig. 2.1. In the square potential case, the density $n(x)$ of non-interacting particles is a cosine function, but is a constant for strongly interacting particles. In the harmonic potential case, $n(x)$ is a Gaussian function for non-interacting particles but becomes parabolic in the strongly interacting case. Generally, the TFA captures the main feature that the repulsive interactions can flatten the BEC distribution in real space.

2.2.3 Feshbach resonance

In order to control the interactions between the atoms, one commonly used technique is based on the Feshbach resonance (FR, or Feshbach-Fano resonance) [16]. It can alter the scattering length from negative infinity to positive infinity by applying a static magnetic field. FR is a resonance of a scattering state of an open channel and a bound state (molecular state) of a closed channel, where the two channels refer to two spin configurations. Usually, both the two channels have Lennard-Jones interaction profile, but their gap can be tuned by a magnetic field via the Zeeman effect. For cold atoms,

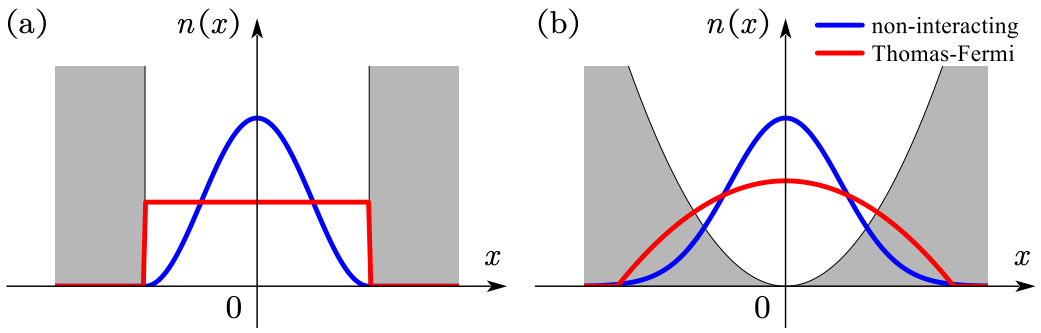


Figure 2.1: Illustration of ground states of BEC without (blue) and with strong (red) interactions. (a) In an infinite square potential, the Thomas-Fermi approximation (TFA) results in a homogeneous distribution. (b) In harmonic trap, the TFA results in a parabolic density distribution.

the far separated atoms are usually in the open channel configuration with nearly-zero energy, compared to the gap between the two channels.

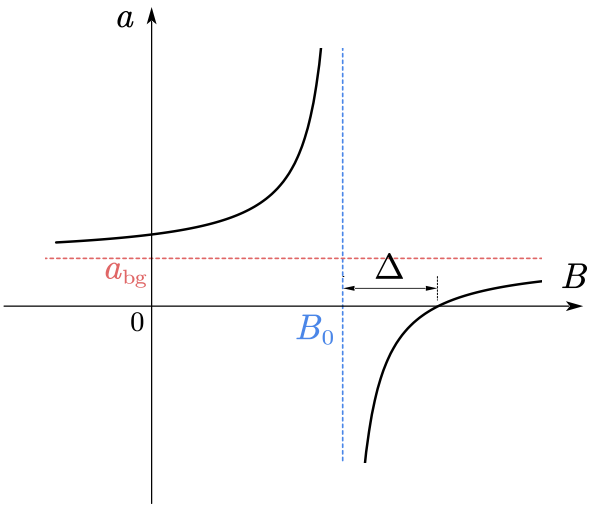


Figure 2.2: Scattering length as a function of the magnetic field near the Feshbach resonance.

Near the resonance point B_0, the scattering length is approximately

$$a(B) = a_{bg}\left(1 - \frac{\Delta}{B - B_0}\right), \tag{2.14}$$

where Δ is the width of the FR, B_0 is the resonant field strength, and a_{bg} is the background scattering length.

The value of B_0 is determined by the Zeeman shift that makes the bound state energy E_c equal to zero plus the coupling between the two channels. The width Δ mainly depends on the spontaneous decay from the bound state. The biased background a_{bg} is dominated by the open channel, and the resonance is due to the narrow scattering process

embedded in the continuum. The scattering phase will flip by π across the resonance. This results in the breaking of the scattering length in two diverging branches.

2.2.4 Length scales of correlation and coherence

To quantitatively describe the spatial correlation and coherence of BEC, there are mainly two length scales.

The first one is the correlation length ξ_{corr}. Generally, it describes how fast a correlation function exponentially decays in space. As for BEC, we can consider the correlation function $C(\mathbf{r},\mathbf{r}') = \langle \hat{\psi}^\dagger(\mathbf{r})\hat{\psi}(\mathbf{r}')\rangle$, and in the long-range limit,

$$\lim_{|\mathbf{r}-\mathbf{r}'|\to\infty} C(\mathbf{r},\mathbf{r}') \sim e^{-|\mathbf{r}-\mathbf{r}'|/\xi_{\text{corr}}}. \tag{2.15}$$

The correlation length is important in phase transitions. As Laudau's mean-field theory suggests, it diverges in the vicinity of the phase boundary.

The second one is the coherence length, or the healing length, ξ_{coh}. For highly repulsive BEC, the wave function is flat in the centre, or in other words, the density is relatively homogeneous and equal to the bulk value. Under the effects of local perturbations or of boundaries, the density of BEC becomes inhomogeneous. ξ_{coh} is a characteristic length that denotes the turning point where the density begins to return to the bulk value. So the wave function is *healed* in a distance ξ_{coh} away from the perturbed centre or the hard boundary. Phenomenologically, ξ_{coh} is estimated by comparing the interaction strength and the kinetic energy according to $\hbar^2/(2m\xi_{\text{coh}}^2) \equiv ng$, where n is the average density. Then we have

$$\xi_{\text{coh}} = \frac{\hbar}{\sqrt{2mng}}. \tag{2.16}$$

This formula tells that when the repulsive interaction is stronger, the global wave function is more resistant against local perturbations. For example, if a vortex is formed in a BEC, the density vanishes at the vortex centre and grows to the bulk value over a distance of ξ_{coh}. Therefore, ξ_{coh} can be used to estimate the size of vortices, and they are expected to be smaller in BECs with stronger repulsive interactions.

2.2.5 Elementary excitation

In the linear Schrödinger equation, the full excitation spectrum can be achieved by diagonalising the Hamiltonian. In the GPE, however, the linearity is broken by the interaction term. One of the basic solutions to this problem is to linearise the non-linear equation in the perturbation regime. This offers a picture of the elementary excitation spectrum, which usually accounts for the collective modes and that can be observed in experiments.

Here we show an example of elementary excitations in free space, where $V_{\text{ext}}(\mathbf{r}) = 0$

which results in the Bogoliubov spectrum. We assume ϕ_0 to be the (unperturbed) ground state of the GPE, and we substitute $\phi = \phi_0 + \delta\phi$ into Eq. (2.11). Keeping the linear term of $\delta\phi$, we get

$$\mathrm{i}\frac{\partial}{\partial t}\delta\phi = H_{\mathrm{GP}}\delta\phi + g\left|\phi_0\right|^2\delta\phi + g\phi_0^2\delta\phi^*, \tag{2.17}$$

where $H_{\mathrm{GP}} = -\frac{\hbar^2}{2m}\nabla^2 + V_{\mathrm{ext}} + g\left|\phi_0\right|^2$. As there is a dependence from $\delta\phi^*$, we can take the conjugation of both sides and derive the equation of motion for the spinor $(\delta\phi, \delta\phi^*)^\top$, which reads

$$\mathrm{i}\frac{\partial}{\partial t}\begin{pmatrix}\delta\phi\\ \delta\phi^*\end{pmatrix} = \begin{pmatrix}H_{\mathrm{GP}} + g\left|\phi_0\right|^2 & g\phi_0^2\\ -g\phi_0^{*2} & -H_{\mathrm{GP}} - g\left|\phi_0\right|^2\end{pmatrix}\begin{pmatrix}\delta\phi\\ \delta\phi^*\end{pmatrix}. \tag{2.18}$$

Now we consider the non-trapped gas ($V_{\mathrm{ext}} = 0$) with homogeneous density. We can try to substitute the plane wave solution $(\delta\phi, \delta\phi^*)^\top = \exp\left[\mathrm{i}(\mathbf{k}\cdot\mathbf{r} - \omega_{\mathbf{k}}t)\right](u_{\mathbf{k}}, v_{\mathbf{k}})^\top$ into Eq. (2.18), where $u_{\mathbf{k}}$ and $v_{\mathbf{k}}$ are the amplitude of the plane waves where we get

$$\omega_{\mathbf{k}}\begin{pmatrix}u_{\mathbf{k}}\\ v_{\mathbf{k}}\end{pmatrix} = \begin{pmatrix}\frac{\hbar^2|\mathbf{k}|^2}{2m} + 2g\left|\phi_0\right|^2 & g\phi_0^2\\ -g\phi_0^{*2} & -\frac{\hbar^2|\mathbf{k}|^2}{2m} - 2g\left|\phi_0\right|^2\end{pmatrix}\begin{pmatrix}u_{\mathbf{k}}\\ v_{\mathbf{k}}\end{pmatrix}. \tag{2.19}$$

Finally, we get the dispersion relation for the elementary excitation which reads

$$\omega_k = \sqrt{\frac{\hbar^2k^2}{2m}\left(\frac{\hbar^2k^2}{2m} + 4g\left|\phi_0\right|^2\right)}. \tag{2.20}$$

This is the Bogoliubov spectrum, and we will see it again in optical lattices in the next section.

2.3 Bosons trapped in optical lattices

The motion of particles in periodic potentials is a fascinating subject in physics. An optical lattice is a system in which atoms are trapped in the standing wave of lasers, and their motion can be precisely controlled. It provides a nearly ideal environment to engineer exotic quantum states of many-body physics. Thus, the atoms in optical lattices can mimic the electrons in solid-state materials, and be used to realise the effects that are difficult to be observed in solid-state systems.

In this work, we will focus on the bosonic atoms trapped in optical lattices. We will start to explain how the atoms are trapped, and how to describe their dynamics with the Bose-Hubbard model (BHM). Then we will introduce the most important phase transition of the BHM, namely the Mott insulator-superfluid transition, followed by the comparison to other models as a universal class. The modification of the BHM with long-range interactions assisted with Rydberg-dressing leads to richer physics, and its dynamics under a quantum quench consists of the project discussed in Chapter 5.

2.3.1 Optical lattice

Similar to the electrons in crystals, it is convenient to depict the atoms either in Bloch representation (momentum space) or Wannier representation (real space). The Wannier representation is suitable for deep lattices, where the dynamics of atoms can be described by their occupation and tunnelling between the lattice sites. But unlike systems in which a single atom occupies a single state, the atoms in the lattice *share* their wave function

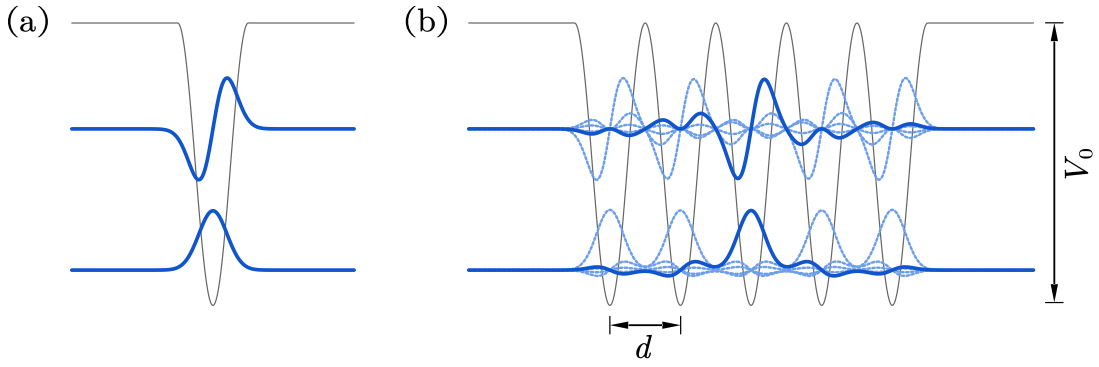


Figure 2.3: Illustrative wave functions (blue curves) for (a) the discrete eigenstates of a single well, (b) the Wannier states of a lattice. The black curve represents the trapping potential. The Wannier states are derived by orthogonalisation of the bound states of a single well, and keep the locality around the lattice points.

In the spirit of the tight-binding model, we can start with an array of isolated sites whose eigenstates are $\psi_{n,\mathbf{R}_i}(\mathbf{r})$, where n is the orbital quantum number and $\mathbf{R}_i$ is the position of the i-th lattice site. In general, one has $\langle \psi_{n_1,\mathbf{R}_i} | \psi_{n_2,\mathbf{R}_i} \rangle = \delta_{n_1,n_2}$, but $\langle \psi_{n,\mathbf{R}_i} | \psi_{n,\mathbf{R}_j} \rangle \neq \delta_{R_i,R_j}$. Wannier wave function $w_{n,\mathbf{R}}(\mathbf{r})$ can be regarded as a set of orthogonalised states, such that $\langle w_{n_1,\mathbf{R}_i} | w_{n_2,\mathbf{R}_j} \rangle = \delta_{n_1,n_2}\delta_{R_i,R_j}$. By doing so, the wave functions of the energetic eigenstates of individual sites will be broadened. In quantum field theory, the connection between the field operator of atoms $\hat{\psi}(\mathbf{r})$ and the Wannier states $\hat{b}_{n,i}$ reads

$$\hat{\psi}(\mathbf{r}) = \sum_{n,i} w_{n,\mathbf{R}_i}(\mathbf{r}-\mathbf{R}_i)\hat{b}_{n,i}. \tag{2.21}$$

In this work, we consider the lowest band only, and we omit the quantum number index n. The Wannier function is highly localised in real space, and its Fourier transform is thereby flat. In theory, we will treat $w_{\mathbf{R}}(\mathbf{r}) \approx \delta(\mathbf{r}-\mathbf{R})$, but in experiment, it can be retrieved by the Gaussian envelope $w_{\mathbf{R}}(\mathbf{r}) \sim \exp\left[-|\mathbf{r}-\mathbf{R}|^2/(2r_0^2)\right]$.
There are two energy scales in an optical lattice, the lattice depth V_0 and the recoil energy $E_r = \frac{\hbar^2}{2m}\left(\frac{2\pi}{d}\right)^2$. The width of the Wannier function is approximately

$$r_0 = \frac{\hbar}{\sqrt{2m\sqrt{V_0 E_r}}}. \tag{2.22}$$

When $r_0 \ll d$, the Wannier envelope is highly localised and thereby the picture of occupation and tunnelling is valid. Intuitively, the tunnelling, or hopping, reflects the kinetic term and multiplicative occupations lead to on-site interaction. One can use the Hamiltonian which is known as the Bose-Hubbard model (BHM) to describe the dynamics of the Wannier particles,

$$H = -J \sum_{\langle i,j \rangle} \hat{b}_i^\dagger \hat{b}_j + \frac{U}{2} \sum_i \hat{n}_i(\hat{n}_i - 1) - \mu \sum_i \hat{n}_i, \tag{2.23}$$

where μ is the chemical potential. The hopping and interaction parameters J and U can also be derived from V_0 and E_r. We quote the results for the deep lattice [8], which reads

$$J = \frac{4}{\sqrt{\pi}} \left(\frac{V_0}{E_r}\right)^{3/4} e^{-2\sqrt{V_0/E_r}} E_r, \tag{2.24a}$$

$$U = 4\sqrt{2\pi} \frac{a_s}{d} \left(\frac{V_0}{E_r}\right)^{3/4} E_r, \tag{2.24b}$$

where a_s is the scattering length. Therefore

$$J/U = \frac{\sqrt{2}}{2\pi} \frac{d}{a_s} e^{-2\sqrt{V_0/E_r}}, \tag{2.25}$$

and

$$r_0 = \hbar \left(m E_r \ln \frac{\sqrt{2}}{2\pi} \frac{U}{J} \frac{d}{a_s} \right)^{-1/2}. \tag{2.26}$$

To flatten the Wannier envelope with fixed J/U and lattice constant d, one needs to deepen the lattice depth V_0. But meanwhile, the tunnelling J will also be suppressed, and therefore, the scattering length a_s shall be tuned lower as well. This can be achieved by the aforementioned Feshbach resonance. To conclude, an ideal BHM should be expected in the presence of a deep optical lattice, created by a high-power laser, and relatively weakly interacting atoms.

2.3.2 Mott-insulator-superfluid transition

The most novel physics of the BHM is the phase transition between the Mott-insulator phase (MI) and the superfluid phase (SF). The order parameter for the MI-SF transition is $\phi_i := \langle \hat{b}_i \rangle$ (locally defined). In the MI phase, $\langle \phi_i \rangle = 0$, but in the SF phase $\langle \phi_i \rangle \neq 0$.
A more subtle definition of the superfluid fraction, however, is derived from the perspective of a two-fluid model. The idea comes from a thought experiment [30], that a moving microtube can make the normal phase fluid stick to it and move at the same speed, but the superfluid component remains at rest in the lab frame. In the microtube frame, on the contrary, the normal phase is at rest whilst the superfluid is moving. As

an analogue in optical lattices, one can introduce a small twisting phase which acts as a microtube creating a moving reference frame. The phase will be added to the hopping term such that $J \to Je^{i\phi}$. The result is that the total energy of the ground state (in SF phase) will be lifted, and the amount of the change leads to the fraction of SF. To summarise, the definition of the SF fraction reads [31, 32]

$$\rho_s = \frac{1}{M} \sum_{\langle i,j \rangle} \phi_i^* \phi_j. \tag{2.27}$$

The factor $\phi_i^* \phi_j$ is associated with the flow operator, literally referring to the flux of particles. Apparently, the mean value of $|\phi_i|$ being non-zero is necessary for the occurrence of ρ_s, but insufficient. In a chequerboard lattices, for example, one can have non-zero SF order in the A-sublattice and zero SF order in the B-sublattice. Thus, $\sum_i |\phi_i| \neq 0$ but $\rho_s = 0$, where the latter is a more preferred quantity to signify the superfluidity strictly. In the MI phase, the atoms are localised in their sites, and the tunnelling is suppressed. The ground state wave function can be expressed as $|\mathrm{MI}\rangle = \prod_i (\hat{b}_i^\dagger)^{\bar{n}} |0\rangle$, where $\bar{n}$ is the mean occupation number. The SF phase is coherent, and its wave function is $|\mathrm{SF}\rangle = (\sum_i \hat{b}_i^\dagger)^{\bar{n}} |0\rangle$. The difference appears as the local $U(1)$ symmetry breaking. Let there be a twisted phase applied to a local operator $\hat{b}_i^\dagger \to e^{i\varphi} \hat{b}_i^\dagger$, the change of $|\mathrm{MI}\rangle$ is a global phase modulation, but the change of $|\mathrm{SF}\rangle$ is not. This leads to the possibility to choose a proper gauge in which the local wave functions, if applicable, of $|\mathrm{SF}\rangle$ are in-phase, but are out-of-phase for $|\mathrm{MI}\rangle$. Under the Gutzwiller ansatz [33], we shall expect $|\mathrm{MI}\rangle$ to be a product of local Fock states with random phase, and $|\mathrm{SF}\rangle$ to be a product of coherent states with the same phase.

For simplicity, we use the perturbation method to show the phase diagram of the BHM with the mean-field approximation. We assume the ground state to be homogeneous, and simplify the many-body Hamiltonian to a single-body one. By doing that, the product of creation/annihilation operators is simplified by $\hat{b}_i^\dagger \hat{b}_j \approx \phi_i^* \hat{b}_j + \phi_j \hat{b}_i^\dagger - \phi_i^* \phi_j$. The sum of the nearest neighbour for the hopping term ends up with a coordination number z, which for example, is equal to 4 for a 2D square lattice. Then the single-body Hamiltonian reads

$$H = -zJ\phi \left(\hat{b}^\dagger + \hat{b} \right) + zJ\phi^2 + \frac{U}{2} n(n-1) - \mu n. \tag{2.28}$$

We have assumed ϕ to be real, which can always be done by applying a global phase without impairing the generality. If we start with the MI state with mean occupation $\bar{n}$ as the unperturbed state, the Hamiltonian can be separated as $H = H_0 + H_1$ where

$$H_0 = \frac{U}{2} \hat{n}(\hat{n}-1) - \mu \hat{n} \tag{2.29a}$$

$$H_1 = -zJ\phi \left(\hat{b}^\dagger + \hat{b} \right) + zJ\phi^2. \tag{2.29b}$$

It is easy to find that the Fock state $|\bar{n}\rangle$ is an eigenstate of H_0 with energy $E_0 = \frac{U}{2}\bar{n}(\bar{n}-1) - \mu\bar{n}$, and the perturbed energy can be worked out to be

$$E_1 = \sum_m \frac{|\langle\bar{n}|H_1|m\rangle|^2}{E_m - E_0} = \left[zJ + (zJ)^2\left(\frac{\bar{n}U}{(\bar{n}-1)U-\mu} - \frac{(\bar{n}+1)U}{\bar{n}U-\mu}\right)\right]\phi^2. \tag{2.30}$$

According to Landau's mean-field theory, the total energy is $E = E_0 + E_1 = a_0 + a_2\phi^2$, where the flip of the sign of a_2 determines the phase transition. For different unperturbed occupation $\bar{n}$, we can get the corresponding phase boundaries

$$zJ/U = \left(\frac{\bar{n}}{\bar{n}-1-\mu/U} - \frac{\bar{n}+1}{\bar{n}-\mu/U}\right)^{-1}. \tag{2.31}$$

The phase diagram with the lowest three lobes of the MI states is shown in Fig.2.4.

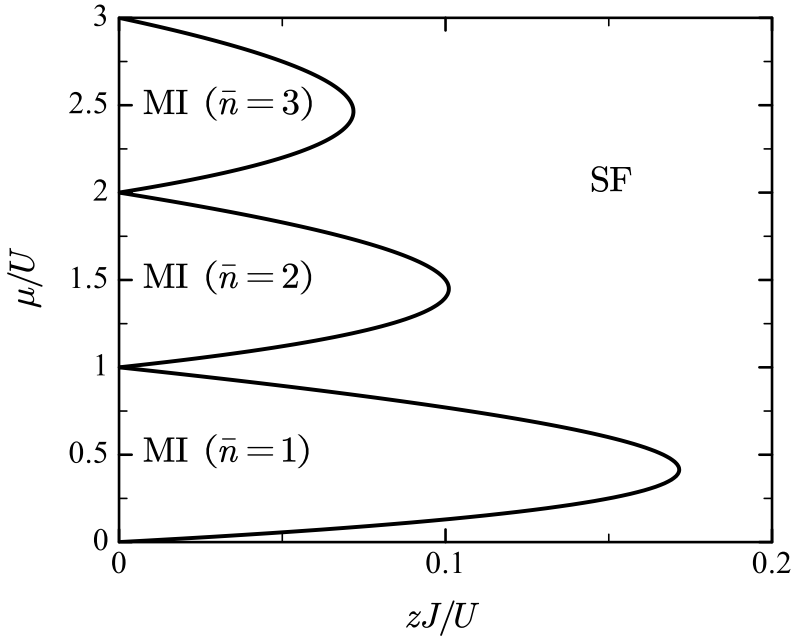


Figure 2.4: The phase diagram of the BHM within perturbation theory. The three lobes stand for the Mott-insulator phases where the occupation varies from 1 to 3 for each lobe. The superfluid phase applies to the large J regime, where the occupation grows smoothly with increasing μ.

Here, we make a few remarks about the perturbation method. First, it is based on mean-field theory, which is expected to be true for $z \to \infty$, or high-dimensional space. Other methods like density-matrix renormalisation group (DMRG) show that the lobes are not round in their tips, which, however, is not much different for a 2D square lattice [34] Second, the unperturbed state is assumed to be homogeneous, which is valid for the ordinary BHM. However, if long-range interactions are taken into consideration, the assumption may fail. If the long-range part is presumed to be nearest-neighbour-only, the assumption is that an A-B lattice can be adopted to reveal the emergence of density modulation, and is relatively consistent with the numerical results from the general case.

However, if longer-range interactions are considered, most pre-assumptions will fail. This will be discussed further in Chapter 5. The realisation of long-range interactions can be introduced by Rydberg-dressing, which is presented in Chapter 3.
Third, the phase diagram in Fig. 2.4 is obtained within the grand canonical ensemble, where μ can be controlled to change the total number of particles. In the quantum quench experiments, however, the dynamics of an optical lattice is usually depicted by a closed system, where the total number of atoms is fixed. Therefore, if one wants to see a phase diagram in $\bar{n}-J$ parametric space, μ becomes floating. One can still use, e.g., imaginary time evolution, plus Nelder-Mead algorithm [35].

2.3.3 Universal class

The BHM has been frequently compared with spin models, in the regime where that only a few Fock states are occupied. For example, if we project the full Hilbert space to only two states $|0\rangle$ and $|1\rangle$, which is suitable for strongly repulsive bosons, or known as hard-core bosons, then we can introduce the spin operators

$$\hat{b} = \hat{S}^{+} = \hat{S}^{x} + \mathrm{i}\hat{S}^{y}, \tag{2.32a}$$

$$\hat{b}^{\dagger} = \hat{S}^{-} = \hat{S}^{x} - \mathrm{i}\hat{S}^{y}, \tag{2.32b}$$

$$\hat{n} = \hat{b}^{\dagger}\hat{b} = \frac{1}{2} - \hat{S}^{z}, \tag{2.32c}$$

where $\hat{S}^{x,y,z} = \frac{1}{2}\hat{\sigma}^{x,y,z}$ and $\hat{\sigma}$ are Pauli matrices. It can be found that the creation and annihilation operators can be translated as spin flips, such as $\hat{b}\,|1\rangle = |0\rangle \to \hat{S}^{+}(0,1)^{\top} = (1,0)^{\top}$, $\hat{b}^{\dagger}\,|0\rangle = |1\rangle \to \hat{S}^{-}(1,0)^{\top} = (0,1)^{\top}$, $\hat{n}\,|0\rangle = 0\,|0\rangle \to (1/2-\hat{S}^{z})(1,0)^{\top} = 0(1,0)^{\top}$, $\hat{n}\,|1\rangle = |1\rangle \to (1/2-\hat{S}^{z})(0,1)^{\top} = (0,1)^{\top}$. By substituting the spin operators into the Hamiltonian (2.23), we can get a new Hamiltonian

$$H^{\mathrm{spin}} = -J\sum_{\langle i,j\rangle}\left(\hat{S}_i^{x}\hat{S}_j^{x} + \hat{S}_i^{y}\hat{S}_j^{y}\right) + \mu\sum_{i}\hat{S}_i^{z}. \tag{2.33}$$

A constant value $\mu M/2$ has been dropped out. Here, due to the fact that the contribution of the selected Fock states $|0\rangle$ and $|1\rangle$ to the interaction energy is zero, the on-site interaction term disappears.
Often we consider the addition of long-range interactions given by the interacting Hamiltonian $H_{\mathrm{LR}} = V\sum_{\langle i,j\rangle}\hat{n}_i\hat{n}_j$ to Eq 2.33, which, in the spin representation, reads

$$H_{\mathrm{LR}}^{\mathrm{spin}} = V\sum_{\langle i,j\rangle}\hat{S}_i^{z}\hat{S}_j^{z} - 2V\sum_{i}\hat{S}_i^{z}. \tag{2.34}$$

This leads to the whole Hamiltonian $H^{\mathrm{tot}} = H^{\mathrm{spin}} + H_{\mathrm{LR}}^{\mathrm{spin}}$ equal to that of an XXZ model. It is heuristic to build up a connection between the BHM and XXZ models or other equivalent spin models, because they share the universal critical behaviours in the vicin-

ity of the phase transitions. Landau pointed out that various physical observables have a power-law dependence to the parameter for continuous phase transitions [20]. For example, if we find that the critical point for the MI-SF transition is J_c, then the distance parameter is $\varepsilon = J/J_c - 1$ ($|\varepsilon| \ll 1$). In the literature [36], we focus on the (mean) order parameter ϕ, the correlation length ξ, and the relaxation time τ, which scale as

$$\phi \sim |\varepsilon|^{-\alpha}, \quad \xi \sim |\varepsilon|^{-\nu}, \quad \tau \sim |\nu|^{-z\nu} \tag{2.35}$$

where α, ν, z are the critical exponents. In general, the exponents may also depend on the sign of ε, but this is not important in our case.

2.3.4 Extended Bose-Hubbard model

Lattice bosons have many features beyond the BHM. For example, if the optical lattice has disordered local chemical potential and hopping parameter [37, 38], the ground state will not be homogeneous.

Another significant change is the long-range (density-density) interaction, which transforms the BHM to the extended Bose-Hubbard model (eBHM) [39],

$$H = -J \sum_{\langle i,j \rangle} \hat{b}_i^\dagger \hat{b}_j + \frac{U}{2} \sum_i \hat{n}_i(\hat{n}_i - 1) - \mu \sum_i \hat{n}_i + \sum_{i,j} V_{ij} \hat{n}_i \hat{n}_j. \tag{2.36}$$

There are two major consequences when V_{ij} is relatively larger than J and U. For the ground state, the translational symmetry may be broken with density waves or supersolid phases [40]. For the elementary excitation, it can make the dispersion relation non-monotonic with roton minima [41]. We will discuss this in detail in chapter 5.

2.4 Beyond mean-field approximation

The interests in the quantum nature of a BEC in free space, harmonic trap or optical lattice requires more advanced methods beyond the mean-field approximation. The numerical methods include, for instance, exact diagonalisation [42], quantum Monte-Carlo methods [43], dynamical mean-field theory [44], density-matrix renormalisation group [34] and phase space methods [45]. Under the scope of phase space, one popular method is called the truncated Wigner approximation (TWA) [46]. It is not only suitable for calculating the ground states, but it is also powerful in solving the dynamics.

The idea of TWA starts from the Fokker-Planck equation (FPE) of the Wigner function, which is a pseudo-probability distribution function in the phase space. By eliminating the high-order time-derivative terms of the Wigner function, one can find that the FPE becomes classical. Hence, we get the TWA which contains two ingredients. First, the evolution of physical variables follows a classical equation. Second, the initial states of

the system is randomly chosen with the probability described by the Wigner function. Then one needs to cast a large number of trajectories from different initial states, and their average derives the mean values of the observables. The detailed connection between TWA and the Gutzwiller ansatz will be discussed in Chapter 5. It is particularly suited to simulate the dynamics of the eBHM.

Chapter 3

Rydberg Interactions

The realisation of various exotic many-body quantum states, such as supersolid, anisotropic Fermi liquid, squeezing [8], requires strong and tunable atom-atom interactions. In this chapter, we will present a popular approach from the last decade that is based on the Rydberg atoms [47]. It has outstanding controllability, in term of interaction strength and length along with the coherence time.

In Section 3.1, we will show some basic properties of Rydberg atoms. In Section 3.2, we will discuss the interaction between two Rydberg atoms. In Section 3.3, we will introduce the interactions induced by Rydberg-dressing. It inherits the advantages of strong interaction strength, and also resolves the problem of its relatively short lifetime. Therefore, Rydberg-dressed ultracold gas can be used to study spatially correlated many-body states.

3.1 Rydberg atom

Rydberg atoms are highly excited atoms. In 1885, Johann Balmer noticed a novel relation of the fluorescence spectra of hydrogen atoms [48]. The positions of the spectral peaks are marked with two integers which are now known as the quantum numbers. In 1913, Niels Bohr came up with a primitive model to explain those integers n by quantising the orbital angular momentum of the electrons [49]. The model successfully describes the energy levels and orbital radii of a sequence of quantum states, such that

$$E_n = -\frac{Z^2}{n^2}\mathrm{Ry}, \tag{3.1a}$$

$$r_n = \frac{n^2}{Z}a_0, \tag{3.1b}$$

where Z is the charge of the atomic core and is equal to 1 for hydrogen or hydrogen-like atoms, $\mathrm{Ry} = \frac{e^4 m_e}{8\varepsilon_0^2 h^2}$ is the Rydberg energy unit, and $a_0 = \frac{4\pi\varepsilon_0\hbar^2}{e^2 m_e}$ is the Bohr radius. Eq. (3.1) can be further corrected by replacing the electron mass m_e by the reduced mass $m_{\mathrm{red}} = m_e m_c/(m_e + m_c)$, where m_c is the mass of the atomic core.

The states with $n \gg 1$ are called Rydberg states. These scaling relations in Eq. (3.1) can be applied to alkali atoms including lithium, sodium, potassium, rubidium and caesium. As for other atoms and ions with single valence electron, these formulae are also valid. Nevertheless, due to the effect of core electrons, there should be a slight change in the scenario of the quantum defect by replacing $n \to n^* = n - \delta_{n,l,j}$, which was initially suggested by Johannes Rydberg in 1890 [50]. The defect factor $\delta_{n,l,j}$ is dependent to the angular momentum l and total spin j including the spin-orbit coupling.
In the following, we will first show a more rigorous approach to getting the wave functions and energies of Rydberg states with model potentials. Then we will show the scaling relationship between various physical quantities and the quantum number n^*.

3.1.1 Alkali atom model

The energy spectra and ground state wave functions of alkali atoms can be obtained by the time-independent Schrödinger equation

$$\left[-\frac{\hbar^2}{2m}\nabla^2 + V(\mathbf{r})\right]\psi(\mathbf{r}) = E\psi(\mathbf{r}), \tag{3.2}$$

where ∇ is the Laplace operator, E is the energy and $\hbar$ is the reduced Planck constant. Eq. (3.2) can be simplified by separating the radial and angular parts. If $V(\mathbf{r})$ is isotropic, one can let $\psi(\mathbf{r}) = R(r)Y_l^m(\theta,\phi)$ with Y_l^m being the spherical harmonics and reduce Eq. (3.2) to a one-dimensional equation

$$\left[-\frac{\hbar^2}{2m}\left(\frac{\mathrm{d}^2}{\mathrm{d}r^2} + \frac{2}{r}\frac{\mathrm{d}}{\mathrm{d}r} + \frac{l(l+1)}{r^2}\right) + V(r)\right]R(r) = ER(r). \tag{3.3}$$

The model potential $V(\mathbf{r})$ is slightly different from the Coulomb force $V_C \sim 1/r$, which reveals the effect of the core electrons. It is widely accepted to use the following parametric function [51]

$$V(r) = -\frac{e^2}{4\pi\varepsilon_0}\left[\frac{Z_{nl}(r)}{r} + \frac{\alpha_c}{2r^4}\left(1 - e^{-(r/r_c)^6}\right)\right]. \tag{3.4}$$

$Z_{nl}(r) = 1 + (Z-1)e^{-a_1 r} - r(a_3 + a_4 r)e^{-a_2 r}$. Compared to the hydrogen model, the effective charge deviating from 1 is due to the screening of the core electrons and the penetration of the valance electron into the atomic core. The static polarisability of the atomic core, α_c, is also included, and its contribution is set to zero in the vicinity of the atom centre. The parameters $a_1, a_2, a_3, a_4, \alpha_c, r_c$ are usually acquired from experiments, and are dependent on the orbital quantum number l [51]. We made a comparison of the model potential for ^{87}Rb atoms at $40S_{1/2}$ state and the that for hydrogen model (Coulomb potential) as shown in Fig. 3.1(a). It can be found that the model potential is deeper, due to the valance electron penetrating into the atom core which feels more

positive charge from the nuclei. The wave function of ^{87}Rb [Fig. 3.1(b)] is also more squeezed towards the centre compared to the hydrogen model, although their oscillatory shapes are very similar.

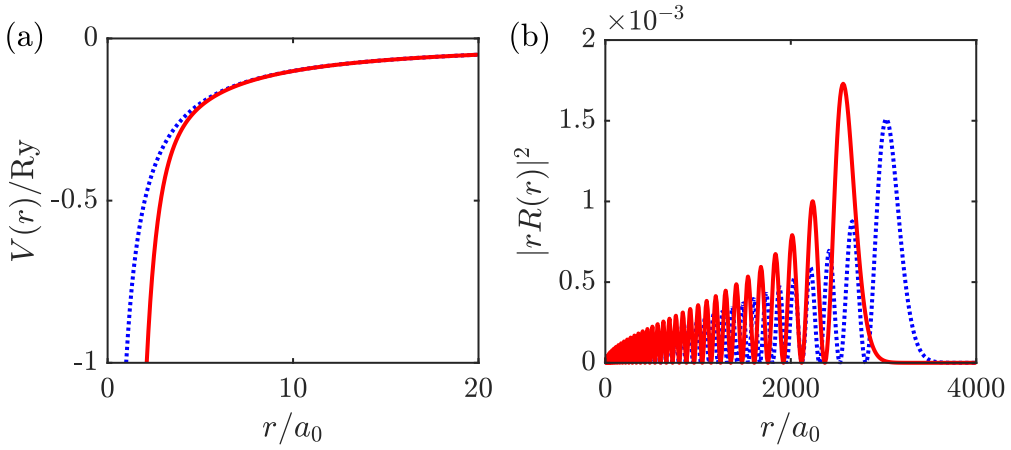


Figure 3.1: Comparison between ^{87}Rb atoms at $40S_{1/2}$ state (solid red line), and the hydrogen model (dotted blue line). (a) The model potential in the unit of Ry. (b) The corresponding radial probability distribution manifesting the wave function.

If the spin of the valance electron is taken into consideration, one needs to insert a spin-orbit coupling (SOC) term, $H_{so}(r) = \frac{1}{4\pi\varepsilon_0 m_e^2 c^2}\frac{e^2}{2r^3}\hat{\mathbf{L}}\cdot\hat{\mathbf{S}}$, to Eq. (3.2) where $\mathbf{L}$ is the angular momentum operator of the valence electron, and $\mathbf{S}$ is its spin. The wave function becomes a spinor with two components standing for the electron spin $m_s = \pm\frac{1}{2}$. After the diagonalisation of the electron-spin part, one gets the representation under the total spin operator $\hat{\mathbf{J}} = \hat{\mathbf{L}} + \hat{\mathbf{S}}$, whose eigenvalue is $\hat{\mathbf{J}}^2\left|j,m_j\right\rangle = j(j+1)\left|j,m_j\right\rangle$, and its z-component $\hat{J}^z\left|j,m_j\right\rangle = m_j\left|j,m_j\right\rangle$. Here $j = |l-s|, |l-s|+1, ..., l+s$, and $m_j = -j, -j+1, ..., j$, $s = 1/2$. For $nS_{1/2}$ state, where $l = 0$, j has a unique choice equal to $1/2$, and SOC can be eliminated.

Eq. (3.2) can be numerically solved by exact diagonalisation [52] or by using the Numerov method [53]. The latter has been integrated with the Alkali Rydberg Calculator (ARC) package for python [54, 55], together with the solvers for Rydberg interactions. In this thesis, the parameters related to Rydberg atoms are all carried out with the ARC package.

3.1.2 Novel scaling relations

As the principal quantum number of the Rydberg states grows, one can find various quantities follow power-law relations with respect to n^*. We conclude some crucial results for S and P Rydberg states as in Table 3.1 [56, 57].

The energy and radius are the same as that of Bohr model as shown in Eq. (3.1) with n simply replaced by n^*. The level spacing is approximately $\sim n^{*-2} - (n+1)^{*-2}$, whose leading term gives rise to n^{*-3}.

energy	n^{*-2}
level spacing	n^{*-3}
orbital radius	n^{*2}
dipole moment with ground state	$n^{*-1.5}$
dipole moment with (n^*+1) state	n^{*2}
lifetime (0 K)	n^{*3}
polarisability	n^{*7}
van der Waals coefficient (C_6)	n^{*11}
dipole-dipole coupling coefficient (C_3)	n^{*4}

Table 3.1: Scaling of several atomic quantities with respect to n^* for Rydberg states with low orbital angular momentum, $l = 0, 1$.

The lifetime of Rydberg atoms at 0 K is only dominated by spontaneous emission. This process consists of many channels because multiple states below the Rydberg state can serve as the final state for the spontaneous decay. The decay rate can be calculated with Fermi's golden rule [58]

$$\Gamma_f = \frac{\omega_{rf}^3}{12\pi\hbar c^3\varepsilon_0}\left|\langle f|\hat{\mathbf{d}}|r\rangle\right|^2, \tag{3.5}$$

where $\hbar\omega_{rf} = E_r - E_f$ is the energy gap between the Rydberg state and the final state, $\hat{\mathbf{d}} = (-e)\mathbf{r}$ is the dipole operator and this formula has already considered the polarisation of the emitted photons. The total decay rate involving all possible $|f\rangle$ reads $\Gamma = \sum_f \Gamma_f$. From Fig. 3.2, we can find that the major contributor to spontaneous decay is the channel directly from the Rydberg state to the ground state (if it is forbidden by the selection rule, the preferred state should be the lowest excited state that is allowed). In this case, $0 \approx |E_r| \ll |E_f|$ and $\omega_{rf} \approx |E_f|/\hbar$ which is independent of n^*. Then Γ only relies on the dipole moment, which is dominated by the overlap of the wave function of the Rydberg state and the ground state. Although the relation between the dipole moment and n^* is not obvious, the analytical solutions to hydrogen model do reveal the leading term $\sim n^{*-3/2}$ holds for S and P states. Then the lifetime becomes $\tau \sim n^{*3}$. Furthermore, we note that the dipole moment between n and $n+1$ Rydberg states follows the scaling n^{*2} for low-l ones.

The polarisability is also dominated by the neighbouring coupling. According to the perturbation theory, the polarisability $\alpha \sim \sum_f |\langle f|\hat{\mathbf{d}}|r\rangle|^2/(E_f - E_r)$. For $|f\rangle$ being low-n states, the contribution is equal to $\sim n^{*-3}$, which decays for growing n^*. But for $|f\rangle$ being the neighbouring Rydberg states, the contribution to α is $\sim n^{*4}/n^{*-3} = n^{*7}$ [59]. Therefore, the transitions to neighbouring Rydberg states dominate the total polarisability, which follows n^{*7}.

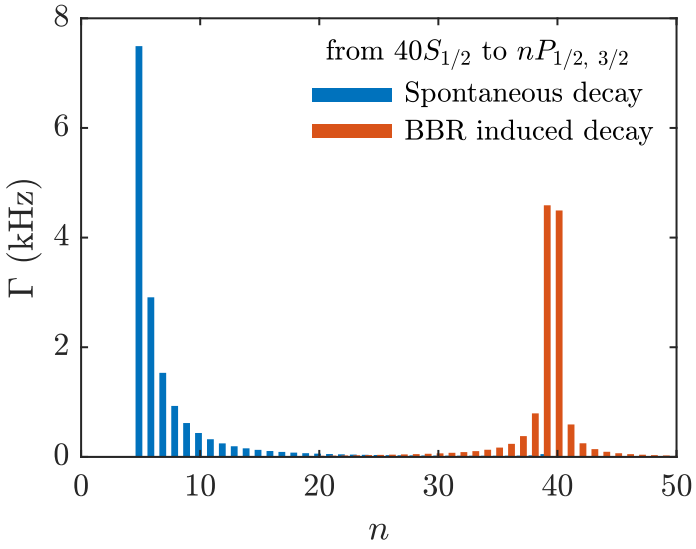


Figure 3.2: The decay rates of ^{87}Rb atoms from $40S_{1/2}$ to $nP_{1/2,\ 3/2}$ states. The blue bars are via spontaneous decay, and the orange for black-body-radiation induced decay at 300 K.

In addition, we need to mention that the scaling relationships are different for circular Rydberg states ($l,\ m \lesssim n$). First, the large l suppresses the transitions from circular Rydberg states to small n states, and only the neighbouring Rydberg states are important. Second, the transitions between neighbouring circular Rydberg states depend on the polarisation. For example, from $|n,l,m\rangle$ state to $|n+1,l+1,m'\rangle$, the scaling relation is $n^*, n^{*3/2}, n^{*2}$ for $m' = m-1,\ m,\ m+1$, respectively. To $|n+1,l-1,m-1\rangle$, the scaling is n^{*2}, and to $|n,l-1,m-1\rangle$, the scaling is $n^{*3/2}$. Then considering the level spacing $\sim n^{*-3}$, one finally gets the transition rate $\Gamma \sim (n^{*-3})^3(n^{*2})^2 = n^{*-5}$ and the lifetime $\tau \sim n^{*5}$ [56].

In Fig. 3.2, we can also find the influence of black body radiation (BBR), which induce the decay from the Rydberg states to their neighbouring states. This part will be substantially suppressed under low temperature, and we can usually ignore the BBR effect only in cryogenic environments.

3.2 Rydberg pair interaction

In classical electrodynamics, we know that the interaction between two separated electric dipoles is given by [60]

$$V(\mathbf{R}) = \frac{1}{4\pi\varepsilon_0}\left(\frac{\mathbf{p}_1\cdot\mathbf{p}_2}{R^3} - \frac{3(\mathbf{p}_1\cdot\mathbf{R})(\mathbf{p}_2\cdot\mathbf{R})}{R^5}\right). \tag{3.6}$$

In quantum mechanics, the classical interaction should be replaced by an operator. The interaction operator $\hat{V}(\mathbf{R})$ is similar to Eq. (3.6) with $\mathbf{p}_i \to \hat{\mathbf{p}}_i = (-e)r|k_i\rangle\langle j_i|$

where $i = 1,2$ and $|j_i\rangle$, $|k_i\rangle$ are the eigenstates of a single atom. When the atom has a dipole moment, we can calculate their dipole-dipole interaction by inserting the two-atom basis $\hat{V}_{12} = \sum_{j_1,j_2}\sum_{k_1,k_2}|j_1,j_2\rangle\langle j_1,j_2|\hat{V}(\mathbf{R})|k_1,k_2\rangle\langle k_1,k_2|$. The matrix elements $\langle j_1,j_2|\hat{V}(\mathbf{R})|k_1,k_2\rangle$ determines the coupling strength. In Rydberg states, the dipole-dipole interaction couples the neighbouring Rydberg states strongly, where $\langle j_1,j_2|\hat{V}(\mathbf{R})|k_1,k_2\rangle \propto n^4$ with n being the principal quantum number.

3.2.1 Diagonalisation method

Without the external fields, an electronic state typically does not possess permanent dipole moment. Hence, the dipole-dipole interaction between two atoms vanishes. The van der Waals interactions, however, can not be neglected. The van der Waals interaction can be obtained by diagonalising the Hamiltonian $\hat{H}$. In the Hilbert space based on $\{|j_1,j_2\rangle\}$, the diagonal terms are the sum of the eigenenergies of $|j_1\rangle$ and $|j_2\rangle$, $H_{j_1j_2,j_1j_2} = E_{j_1} + E_{j_2}$, and the off-diagonal terms are the matrix elements of the interaction $H_{k_1k_2,j_1j_2} = \langle j_1,j_2|\hat{V}(\mathbf{R})|k_1,k_2\rangle$.
In Fig. 3.3, we show a diagonalisation result of ^{40}K atoms around $50S_{1/2}$ state. In the long-range regime, the energy shift perfectly fits a scaling relation $V \sim R^{-6}$. At short-ranges, however, it deviates from the R^{-6} relation, and more importantly, $50S_{1/2}$ state intersects with other states and the Rydberg atoms are no longer stable.

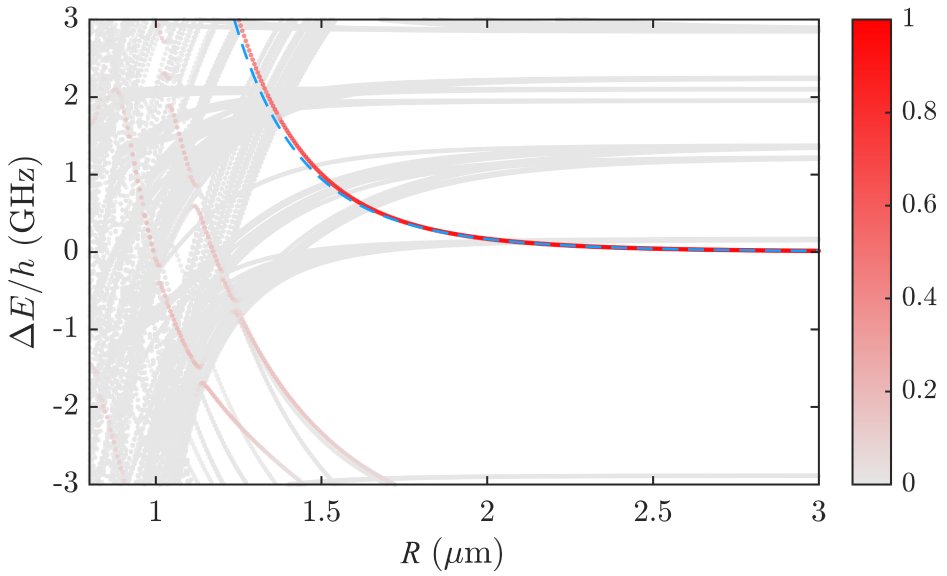


Figure 3.3: The Rydberg pair interaction of ^{40}K by diagonalisation method. The redness of the scatters is the population of $50S_{1/2}$ state. The dashed blue curve is calculated via perturbation method with $C_6 = -10.75$ GHz μm^6.

The R^{-6} scaling relation can be acquired via a simplified model. We can reduce the complicated interaction matrix to a simple 2-by-2 matrix, such that only one channel is considered. Suppose the target Rydberg pair state is $|rr\rangle$, which is coupled to $|r'r''\rangle$,

their energy gap being Δ, interaction strength $V(\mathbf{R})$, the Hamiltonian reads

$$H = \begin{pmatrix} 0 & V(\mathbf{R}) \\ V(\mathbf{R}) & \Delta \end{pmatrix}. \tag{3.7}$$

The eigenenergies are

$$E = \frac{1}{2}\left(\Delta \pm \sqrt{\Delta^2 + 4V(\mathbf{R})^2}\right), \tag{3.8}$$

and we should take the minus sign for the $|rr\rangle$ branch. According to Eq. (3.6), the leading term of $V(\mathbf{R})$ is $\sim R^{-3}$. Then we can find that (a) in the long-range limit, $V(\mathbf{R}) \ll \Delta$, the energy shift is approximately $E \approx -V(\mathbf{R})^2/\Delta = -C_6/R^6$, (b) in the short-range limit, $V(\mathbf{R}) \gg \Delta$, and $E \approx -V(\mathbf{R}) = -C_3/R^3$.
The long-range limit is also known as van der Waals regime, and the difference compared to the conventional van der Waals interaction of ground state atoms is mainly due to the large polarisability of Rydberg states.

3.2.2 Perturbation method

The diagonalisation method is often costly for computation. So it is important to introduce the perturbation method such that we can get the interaction parameters approximately. However, its accuracy is not always guaranteed in the short-range regime.
According to the second-order perturbation theory, the energy shift is given by $\Delta E = \sum_j \left|\langle j|\hat{V}|i\rangle\right|^2/(E_i - E_j)$, where $|i\rangle$ is the unperturbed state, $|j\rangle$ is the coupled state. According to Eq. (3.6), $\hat{V} \propto R^{-3}$, which must lead to $\Delta E \propto R^{-6}$. Then we can get the C_6 parameter

$$C_6 = \sum_{r'r''} \frac{R^6 \left|\langle r'r''|\hat{V}(\mathbf{R})|rr\rangle\right|^2}{E_{r'} + E_{r''} - 2E_r}. \tag{3.9}$$

The length of $\mathbf{R}$ has been cancelled, but its direction is still important. If the wave function of $|rr\rangle$ is not isotropic, C_6 may be angular dependent. In Fig. 3.3, we show the results of the energy spectrum of ^{40}K atom around $50S_{1/2}$ state. In short-range regime, we can find a lot of anti-crossing patterns. In long-range regime, the energy shift fits well with the R^{-6} law.

3.2.3 Anisotropic interactions

The previous example for $nS_{1/2}$ state is isotropic, which is not valid for other Rydberg states in general. Here we will just show some examples, and more details can be found in Chapter 7.
In Fig. 3.4, we made a comparison between $50S_{1/2}$ and $50P_{3/2}$ state, where we let $m_j = j$ for the maximal dipole moment. In spherical coordinate where the 3D angle with respect to the quantum axis is (θ, ϕ), one can find that the azimuthal symmetry is

always guaranteed. Therefore, we plot the C_6 parameter versus the polar angle θ. The result of S state is indeed isotropic, but the P state shows a nearly "8"-shaped profile.

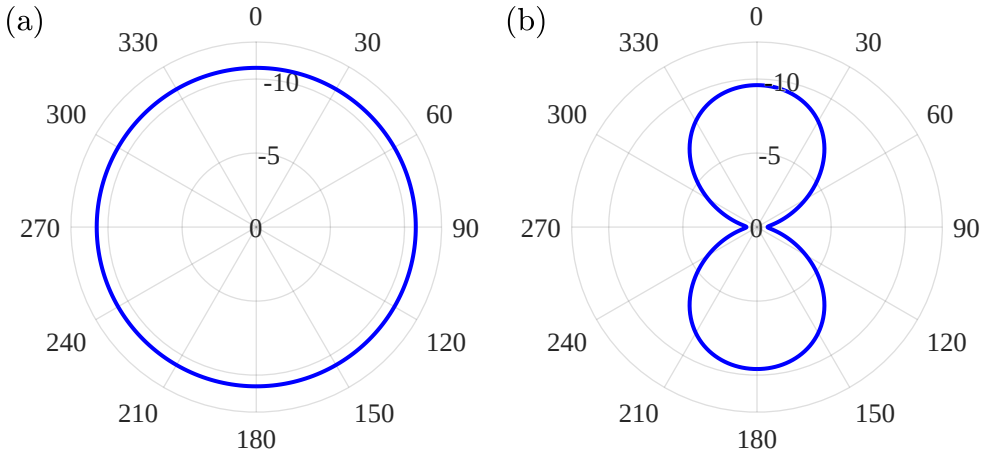


Figure 3.4: The C_6 parameter versus polar angle θ for ^{40}K pairs in nS and nP states. (a) $n = 50$, $l = 0$, $j = \frac{1}{2}$, $m_j = \frac{1}{2}$, (b) $n = 50$, $l = 1$, $j = \frac{3}{2}$, $m_j = \frac{3}{2}$. unit: GHz μm^6.

3.3 Rydberg dressing

The Rydberg atoms are strongly interacting particles but are also unstable for various reasons. First, the Rydberg pair interaction is so strong that usually only one atom within the interaction length can be excited, which is known as the blockade, and it limits the density of the interacting atoms. Second, the lifetimes of Rydberg states are usually in the order of microseconds to milliseconds, which is not sufficiently long for many quantum operations. Third, the collisions between Rydberg atoms and local fluctuations of electromagnetic fields can easily ionise the valence electron, which destroys the Rydberg states. Therefore, another type of interaction, called Rydberg-dressing, attracts lots of attention which resolves many problems.

The Rydberg-dressing means weakly pumping the atom from its ground state to the Rydberg state with a minuscule probability, such that the internal state of the atom is a superposition $|\Psi\rangle \approx |g\rangle + \eta\,|r\rangle$, where $|\eta| \ll 1$. The advantage lies on that all the atoms in the gas can be dressed. Their interaction lengths are dominated by both the Rydberg states $|r\rangle$ and the driving lasers, which are in the order of micrometres. The lifetimes of such dressed states are also significantly longer than the bare Rydberg states. Despite the relatively smaller interaction strengths when compared to the Rydberg-pair interactions, the former is still stronger than most other interactions in neutral atoms.

3.3.1 Rydberg-dressing schemes

Here we show two schemes to prepare Rydberg-dressed atoms with one-photon and two-photon approaches, respectively. However, later we will also simplify the two-photon scheme to an equivalent one-photon scheme for convenience.

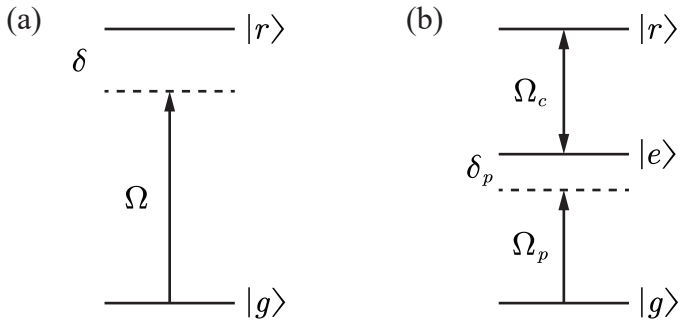


Figure 3.5: (a) One-photon dressing (b) Two-photon dressing

For the one-photon dressing scheme [Fig. 3.5(a)], the Hamiltonian under rotating wave approximation (RWA) reads [61, 62]

$$H_1 = \begin{pmatrix} 0 & \Omega/2 \\ \Omega/2 & \delta \end{pmatrix}. \tag{3.10}$$

The eigenenergies are $E = \frac{1}{2}(\delta \pm \sqrt{\delta^2+\Omega^2})$, which results in the ground state $|g'\rangle \approx \left[1, (\delta - \sqrt{\delta^2+\Omega^2})/\Omega\right]^\top$. Under weak-coupling approximation, $\Omega \ll |\delta|$, the ground state wave function becomes $|g'\rangle \approx [1, \Omega/(2\delta)]^\top$, and the occupation of Rydberg state is $P(|r\rangle) = |\eta|^2 \approx \Omega^2/(4\delta^2)$.

Another common scheme is two-photon dressing, or referred to as electromagnetically induced transparency (EIT) scheme [Fig. 3.5(b)]. It is necessary for dressing atoms from their ground S-state ($l = 0$) to Rydberg D-states ($l = 2$), and the use of two photons are usually in the visible light regime, unlike one-photon scheme where the coupling laser is ultraviolet. Here we write down the three-level RWA Hamiltonian

$$H_2 = \begin{pmatrix} 0 & \Omega_p/2 & 0 \\ \Omega_p/2 & \delta_p & \Omega_c/2 \\ 0 & \Omega_c/2 & \delta_p \end{pmatrix}. \tag{3.11}$$

The lifetime of the intermediate excited state is 2 to 3 orders smaller than Rydberg states, and its occupation is very small under large detuning condition, so we will try to remove it and reduce H_2 to an effective H_1. We find the eigenstate $|g'\rangle$ up to the leading terms of $|\Omega|$ is approximately

$$|g'\rangle \approx |g\rangle - \frac{\Omega_p}{2\delta_p}|e\rangle + \frac{\Omega_c\Omega_p}{4\delta_p^2}|r\rangle. \tag{3.12}$$

Dropping the intermediate state $|e\rangle$, we can find the effective Rabi frequency coupling $|g\rangle$ and $|r\rangle$ is $\Omega_{\text{eff}} = \Omega_c\Omega_p/(2\delta_p)$, and the effective detuning is equal to the two-photon detuning δ_p [63, 64].
The lifetime of Rydberg-dressed state, γ', is longer than the Rydberg states, γ. According to Fermi's golden rule, the transition rate for Rydberg-dressed state to the ground state is $\gamma' \sim \left|\langle g'|\hat{\mathbf{d}}|g\rangle\right|^2 = |\eta|^2\left|\langle r|\hat{\mathbf{d}}|g\rangle\right|^2$. Therefore, $\gamma'/\gamma \approx |\eta|^{-2} \approx 4\delta^2/\Omega^2$.

3.3.2 Rydberg-dressed interaction

Now we turn to the interaction between two Rydberg-dressed atoms. For simplicity, we assume the two atoms are identical and dressed via (effective) one-photon scheme. Using two atom basis, $\{|gg\rangle, |gr\rangle, |rg\rangle, |rr\rangle\}$, the Hamiltonian reads

$$H = \begin{pmatrix} 0 & \Omega/2 & \Omega/2 & 0 \\ \Omega/2 & \delta & 0 & \Omega/2 \\ \Omega/2 & 0 & \delta & \Omega/2 \\ 0 & \Omega/2 & \Omega/2 & 2\delta + V_{rr}(\mathbf{R}) \end{pmatrix}. \tag{3.13}$$

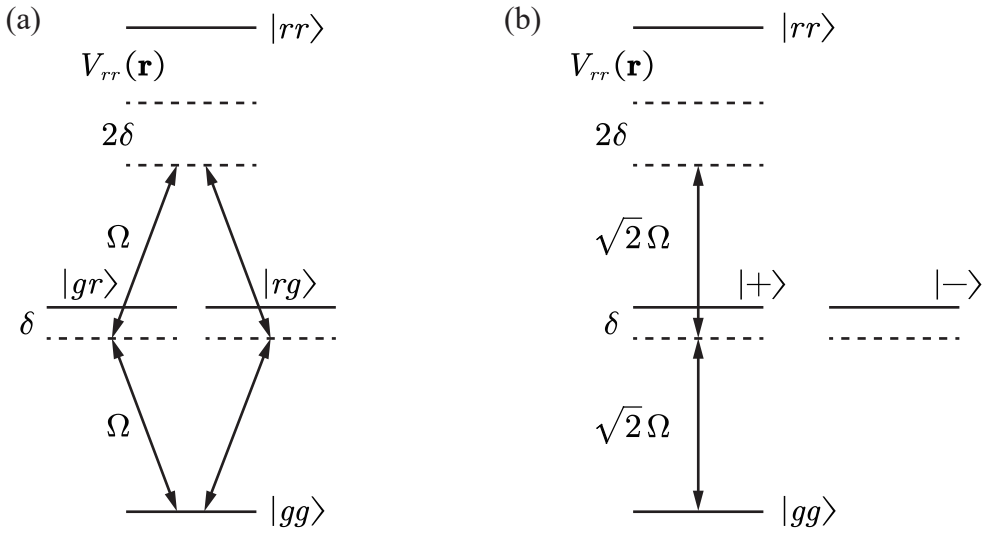


Figure 3.6: (a) Level diagram for two Rydberg-dressed atoms. (b) Level diagram under transformation from $\{|gr\rangle, |rg\rangle\}$ to $\{|+\rangle, |-\rangle\}$.

It is found that this Hamiltonian can be partitioned by transforming the basis to another set $\{|gg\rangle, |+\rangle, |-\rangle, |rr\rangle\}$, where the symmetric (antisymmetric) state $|\pm\rangle = 1/\sqrt{2}(|gr\rangle \pm |rg\rangle)$. The new Hamiltonian is

$$H = \begin{pmatrix} 0 & \Omega/\sqrt{2} & 0 & 0 \\ \Omega/\sqrt{2} & \delta & 0 & \Omega/\sqrt{2} \\ 0 & 0 & \delta & 0 \\ 0 & \Omega/\sqrt{2} & 0 & 2\delta + V_{rr}(\mathbf{R}) \end{pmatrix}. \tag{3.14}$$

Then one can find that the subset basis, $\{|gg\rangle, |+\rangle, |rr\rangle\}$, is uncoupled with the anti-symmetric state $|-\rangle$. The difference lies on that the effective coupling in the two-atom basis is enhanced by a factor of $\sqrt{2}$ compared to the original basis.

Then we consider the ground state and energy spectrum of the Hamiltonian exclusive for $|-\rangle$, which tells us the interaction strength. One can expect a perturbative solution such that the occupation in $|+\rangle$ and $|rr\rangle$ states is relatively small. For the non-interacting case $V_{rr}(\mathbf{R}) = 0$, the *exact* eigenenergies are $E_g = \delta - \sqrt{\delta^2 + \Omega^2}$, $E_+ = \delta$, $E_r = \delta + \sqrt{\delta^2 + \Omega^2}$. Here we can see that the energy of $|+\rangle$ is unchanged, but $|gg\rangle$ and $|rr\rangle$ are shifted by the AC Stark effect. On top of that, as we introduce $V_{rr}(\mathbf{R})$, the energy E_g is further shifted. Under the condition that $|\delta| \gg \Omega$, one can find $E_g \approx \delta - \sqrt{\delta^2 + \Omega^2} + \Omega^4/(8\delta^3)V_{rr}(\mathbf{R})/[2\delta + V_{rr}(\mathbf{R})]$. By substituting $V_{rr}(\mathbf{R}) = -C_6/R^6$, the Rydberg-dressed interaction finally reads

$$V_{\mathrm{RDI}}(R) = \frac{\Omega^4}{8\delta^3} \frac{r_B^6}{R^6 + r_B^6}, \tag{3.15}$$

where $r_B = \sqrt[6]{-C_6/(2\delta)}$. This result can be straightforwardly extended to anisotropic cases where $C_6(\theta, \phi)$ is angular dependent that results in anisotropic $r_B(\theta, \phi)$.

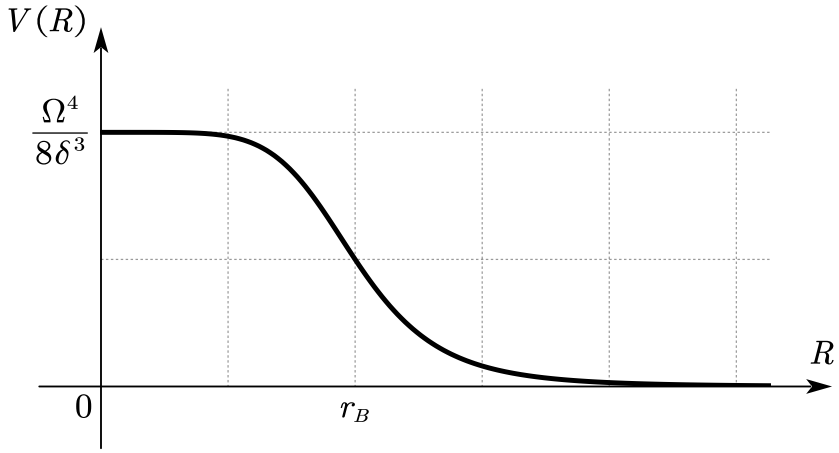


Figure 3.7: Profile of the Rydberg-dressed interaction.

In order to ensure that r_B is real, the sign of C_6 and δ should be opposite, which means the attractive interaction requires blue detuned dressing laser whilst the repulsive interaction needs red detuned laser. On the other hand, the sign of V_{RDI} also depends on δ, such that the attractive (repulsive) pair interaction is expected to produce attractive (repulsive) dressed interaction.

Chapter 4

Project: Trapped Atomic Sagnac Interferometer

The nature that atoms, electrons and other massive particles can propagate like waves leads to the presence of matter-wave interferometers. Despite playing as an analogy to the light interferometer, a matter-wave interferometer also has broad applications to high precision measurements. The most common outcomes include the linear acceleration and rotation [9, 65–68], the gravitation force and its gradient [69–73] as well as the magnetic field [74–76]. It is also applied to fundamental physics research, including measuring Newtonian gravity constant [77–80], relativity effects [81–84], fine structure constant [85, 86], etc. The astonishing high precision is achieved using Ramsey fringes, which shares the same principles as that in the atomic clocks [87–90].

In this work, we focus on the atomic Sagnac interferometer (ASI), which measures the external rotation. With the development of laser optics, vacuum technologies and nano fabrications, the apparatus of ASIs have been created in various architectures. For example, in the 1990s, ASIs are performed mainly in atom beams. The split methods include mechanical double-slit [91], optical gratings [92], two-photon Raman transitions [88, 89], etc. However, the trapped ultracold atom is becoming more appealing for better control of velocity, longer lifetime, and higher compatibility [93]. The newest protocols of guided ASI using time-averaged-adiabatic potential (TAAP) traps [94–99] have great prospect to compete with the state-of-the-art beam interferometers and conventional optical sensors. We will study the dynamics of Bose-Einstein condensate (BEC) in TAAP and the optimal sensitivities of ASI. The interactions between atoms are also analysed with numerical methods.

In Section 4.1, we will give a brief overview of the general principles of the Sagnac effect. In Section 4.2, we will introduce the ASI based on BEC and the mathematical models. We will show the basic procedure to operate an ASI, and the corresponding formalism for each step. In Section 4.3, we will show the analytical solutions to the ASI with non-interacting particles. These results inspire us to optimise the driving

function. In Section 4.4, we offer some numerical results for interacting particles. The influences of the atomic interactions are studied quantitatively.

4.1 Sagnac effect

The general view of the Sagnac effect can be understood by a Mach-Zehnder interferometer (MZI), as shown in Fig. 4.1. A wave (either optical or atomic) is split into two paths and interfere for detection. If the MZI is rotating, the phase accumulation on the two paths will differ and results in a shift of the interference fringes. This corresponding phase is called the Sagnac phase ϕ_s.

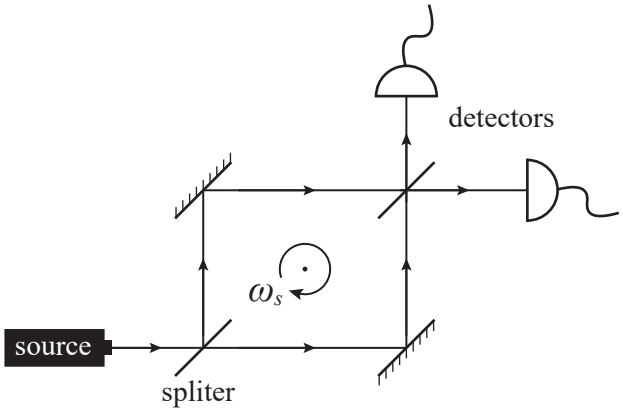


Figure 4.1: Sketch of a Mach-Zehnder interferometer for measuring the Sagnac effect.

For point-wise particles, the interference phase is given by

$$\phi = \frac{1}{\hbar}\left(\int_{C_1} \mathbf{p}_1 \cdot \mathrm{d}\mathbf{r} - \int_{C_2} \mathbf{p}_2 \cdot \mathrm{d}\mathbf{r}\right), \tag{4.1}$$

where $C_1 + C_2$ forms a closed loop with area A. In the laboratory frame, the Sagnac effect takes place by altering the momentum $\mathbf{p}_1 \to \mathbf{p}_1 + m\boldsymbol{\omega}_s \times \mathbf{r}$, and $\mathbf{p}_2 \to \mathbf{p}_2 - m\boldsymbol{\omega}_s \times \mathbf{r}$, where m is the mass of the particles. The Sagnac phase is thereby achieved using Stokes' theorem [100]

$$\phi_s = \frac{1}{\hbar}\oint_{C_1+C_2} m(\boldsymbol{\omega}_s \times \mathbf{r}) \cdot \mathrm{d}\mathbf{r} = \frac{m}{\hbar}\iint_A \nabla \times (\boldsymbol{\omega}_s \times \mathbf{r}) \cdot \mathrm{d}\mathbf{A} = \frac{2m}{\hbar}\boldsymbol{\omega}_s A. \tag{4.2}$$

One can also revisit the interferometry in the rotating frame of the MZI, where the phase difference becomes the frequency shift under the concept of heterodyne interferometry. For optical Saganc interferometer, regardless of the relativity effects, the leading term of ϕ_s can be simply achieved by substituting the relativistic mass $m = \hbar\nu/c^2$ into Eq. (4.2), and $\phi_s = 4\pi/(\lambda c)\omega_s A$ [101] (some other literature may show 8π because they let the light travels the whole loop for each path).

4.2 BEC-based atomic Sagnac interferometer

The atomic versions of Sagnac interferometers have evolved for a few generations. For example, the earliest demonstration was accomplished with atom beams [89]. The use of confined BECs is attracting more attention for higher sensitivity. It may appear to be two BECs in a double-well, or a ring trap, or, in this work, trapped atoms on a ring path. We illustrate the geometric set-up in Fig.4.2(a).

The basic idea consists of three steps. First, start with a BEC in a harmonic trap at $\theta_p = 0$ and then split into two hyperfine states $|1\rangle$ and $|2\rangle$. Second, drive the two parts of atoms separately along the ring whose radius is R_p. Third, recombine the two cloud on the other side of the ring for measurement. Under the lab frame, if the apparatus is rotating at angular frequency ω_s, and the integration driving time is T, one can expect the path difference of the two components to be $2\omega_s T$, which is our target.

For measurement, the favoured quantity is the occupation of the atoms in a particular atomic state, or the population difference between the state $|1\rangle$ and $|2\rangle$. In the first step, we split the atoms into equal probability. In the third step, we generate a population difference which encodes the Sagnac effect. Another critical issue is the *external state* of the atoms. Just like a cup of coffee which sloshes around when moved, the BECs will also vibrate during the transport. Here, the vibration of BECs is a collective phenomenon, and should be described by a dynamical equation.

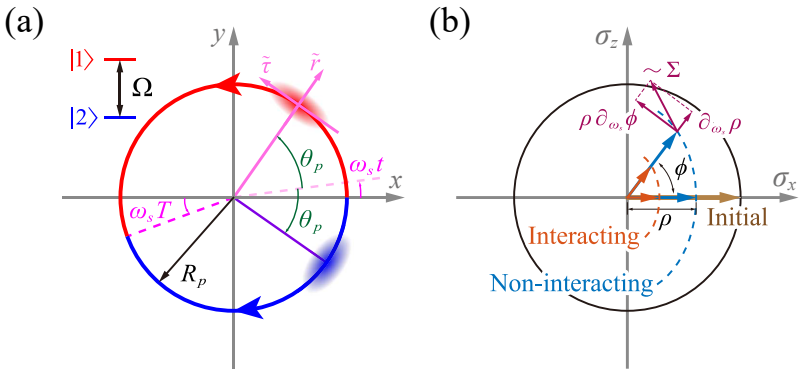


Figure 4.2: (a) Geometry of Sagnac interferometer. The two-component BEC are coupled by Rabi frequency Ω, and driven along the ring paths separately. Under the laboratory frame of reference, the lengths of the two paths differ by $2R_p\omega_s T$. (b) Mapped internal state of the two-component BEC after the interference.

4.2.1 Pseudospin model

To model the ASI, we assume the quantum state of the atoms is a product of spacial wave function in 2D space (external state) and pseudospin state encoded by the hyperfine levels (internal state). By doing that, only the condensate atoms are taken into consideration.

The model of the interferometer is described by a two-component wave function and is written as a spinor $|\Psi\rangle = [\psi_1(\mathbf{r}), \psi_2(\mathbf{r})]^\top$. By integrating the spacial part, the system can be mapped to a two-state model with its state vector located in the Bloch sphere. By integrating the spatial part, we can get the expectation value of the Pauli matrices by $\langle\sigma_i\rangle = \iint \langle\Psi(\mathbf{r})|\sigma_i|\Psi(\mathbf{r})\rangle \, \mathrm{d}^2\mathbf{r}$ which yields

$$\langle\sigma_x\rangle = \iint \mathrm{Re}\left[\psi_1^*(\mathbf{r})\psi_2(\mathbf{r})\right] \mathrm{d}^2\mathbf{r} \tag{4.3a}$$

$$\langle\sigma_y\rangle = \iint \mathrm{Im}\left[\psi_1^*(\mathbf{r})\psi_2(\mathbf{r})\right] \mathrm{d}^2\mathbf{r} \tag{4.3b}$$

$$\langle\sigma_z\rangle = \iint \left[|\psi_1(\mathbf{r})|^2 - |\psi_2(\mathbf{r})|^2\right] \mathrm{d}^2\mathbf{r} \tag{4.3c}$$

The length of the Bloch vector unveils the overlap of the two wave packets in real space, which is equal to 1 if they are fully overlapped.
The procedure to operate the Sagnac interferometer is summarised below:

1. Prepare a ground state in $|1\rangle$ state $|\Psi\rangle = [\psi_g(\mathbf{r}), 0]^\top$.
2. A $\pi/2$-pulse transfers the system to a coherent superposition state $|\Psi\rangle = \frac{1}{\sqrt{2}}[\psi_g(\mathbf{r}), \psi_g(\mathbf{r})]^\top$.
3. Let the two components of atoms propagate and recombine at $t = T$.
4. Apply another $\pi/2$-pulse to tilt the Bloch vector and generate population difference between the two spin-states.

The manipulation of the external states of the two-component BECs can be described by coupled Gross-Pitaevskii equations. In the pseudospin picture, the Hamiltonian reads

$$H = \begin{pmatrix} h_1 + g_{11}|\psi_1|^2 + g_{12}|\psi_2|^2 & \Omega/2 \\ \Omega^*/2 & h_2 + g_{21}|\psi_1|^2 + g_{22}|\psi_2|^2 \end{pmatrix}, \tag{4.4}$$

where $h_i = -\frac{\hbar^2}{2m}\nabla^2 + V_i(\mathbf{r};t)$, $i = 1,2$. Ω is the Rabi frequency of the laser pulse which flips the internal state, and is applied to the aforementioned second and fourth steps. We assume they are sufficiently short and will not affect the spatial (external) dynamics. g_{ij} are spin-dependent short-range interaction parameters caused by s-wave scattering. In 3D, $g_{ij} = 4\pi\hbar^2 N a_{ij}/m$, where a_{ij} is the scattering length and N is the particle numbers. In 2D, however, g_{ij} is scaled by a factor of $1/\sqrt{2\pi l_z^2}$ presuming the confinement along z-direction is harmonic and the trapping length is l_z [102, 103]. The external trap $V_i(\mathbf{r};t)$ is achieved by expanding around trapping centre to the second order, which will be discussed in the next section. As a model, we have

$$V_i(\mathbf{r};t) = \frac{1}{2}m\omega_r\tilde{r}_i(t)^2 + \frac{1}{2}m\omega_\tau\tilde{\tau}_i(t)^2, \tag{4.5}$$

where $(\tilde{r}_i, \tilde{\tau}_i)$ are local coordinates shown in Fig.4.2a, and

$$\tilde{r}_i(t) = (x - R_p\cos\Theta_i)\cos\Theta_i - (y - R_p\sin\Theta_i)\sin\Theta_i \tag{4.6a}$$

$$\tilde{\tau}_i(t) = (x - R_p\cos\Theta_i)\sin\Theta_i + (y - R_p\sin\Theta_i)\cos\Theta_i \tag{4.6b}$$

$$\Theta_i(t) = \pm\theta_p(t) + \omega_s t \quad (+ : i = 1,\ - : i = 2) \tag{4.6c}$$

$\theta_p(t)$ is driving function which satisfies $\theta_p(0) = 0$ and $\theta_p(T) = \pi$, such that the trap centres will travel from one point on the ring to the opposite side.

4.2.2 Manipulating the internal state

To maximise the sensitivity of the Sagnac interferometer, one shall expect the polarisations of the pulses in Step 2 and 4 to be perpendicular. For example, if the first $\pi/2$-pulse is along the σ_x direction, the second one should be along σ_y direction.
Let the direction of the pulse be denoted by (θ_r, ϕ_r). Generally, the generator of a pulse is defined as

$$\hat{X} = \frac{\Omega}{2}\left(\sin\theta_r\cos\phi_r\sigma_x + \sin\theta_r\sin\phi_r\sigma_y + \cos\theta_r\sigma_z\right). \tag{4.7}$$

The rotation angle is given by $\Theta_r = \Omega T_r$, which is equal to $\pi/2$ in our cases. The rotation operator $\hat{R}$ is the matrix exponential of the generator, then applies to the spinor yielding the rotated state. It reads

$$\hat{R}_{\theta_r,\phi_r}(\Theta_r) = e^{-\mathrm{i}T_r\hat{X}} = \begin{pmatrix} \cos\frac{\Theta_r}{2} - \mathrm{i}\sin\frac{\Theta_r}{2}\cos\theta_r & -\mathrm{i}\sin\frac{\Theta_r}{2}\sin\theta_r e^{-\mathrm{i}\phi_r} \\ \mathrm{i}\sin\frac{\Theta_r}{2}\sin\theta_r e^{\mathrm{i}\phi_r} & \cos\frac{\Theta_r}{2} + \mathrm{i}\sin\frac{\Theta_r}{2}\cos\theta_r \end{pmatrix}. \tag{4.8}$$

Without loss of generality, let the first $\pi/2$-pulse points along the σ_y direction, its rotation operator reads

$$\hat{R}_{\pi/2,\pi/2}(\pi/2) = \frac{1}{\sqrt{2}}\begin{pmatrix} 1 & -1 \\ 1 & 1 \end{pmatrix}, \tag{4.9}$$

which maps the spin-polarised ground state $[\psi_g(\mathbf{r}), 0]^\top$ to the equipartition state $|\Psi(0)\rangle = [\psi_g(\mathbf{r}), \psi_g(\mathbf{r})]^\top/\sqrt{2}$ as we desired.
After Step 3, we find the state becomes $|\Psi(T)\rangle = [\psi_1(\mathbf{r}), \psi_2(\mathbf{r})]^\top$. It is also expected that $\iint \langle\Psi(T)|\sigma_z|\Psi(T)\rangle\,\mathrm{d}^2\mathbf{r} = 0$, and if $\omega_s = 0$, one can also have $\iint \langle\Psi(T)|\sigma_y|\Psi(T)\rangle\,\mathrm{d}^2\mathbf{r} = 0$. The optimal measurement should be achieved by maximising the output of $\langle\sigma_z\rangle$, i.e., to maximise $\iint \langle\hat{R}\Psi(T)|\sigma_z|\hat{R}\Psi(T)\rangle\,\mathrm{d}^2\mathbf{r}$. The integrand yields

$$\langle\sigma(\mathbf{r})\rangle = \frac{1}{2}\cos^2\theta_r\left(|\psi_1(\mathbf{r})|^2 - |\psi_2(\mathbf{r})|^2\right) + \mathrm{Re}\left[(1 - \mathrm{i}\cos\theta_r)(\mathrm{i}\sin\theta_r e^{\mathrm{i}\phi_r})\psi_1(\mathbf{r})\psi_2^*(\mathbf{r})\right]. \tag{4.10}$$

Considering $\iint |\psi_1(\mathbf{r})|^2\,\mathrm{d}^2\mathbf{r} = \iint |\psi_2(\mathbf{r})|^2\,\mathrm{d}^2\mathbf{r}$, The final measurement of $\langle\sigma_z\rangle$ reads

$$\langle\sigma_z\rangle = \rho\sin\theta_r\left[\cos\theta_r\cos(\phi_r - \phi) - \sin(\phi_r - \phi)\right], \tag{4.11}$$

where ρ and ϕ are both real, and defined by the overlap

$$\iint \psi_1(\mathbf{r})\psi_2^*(\mathbf{r})\mathrm{d}^2\mathbf{r} \stackrel{!}{=} \rho e^{-\mathrm{i}\phi}. \tag{4.12}$$

The importance lies in that ρ tells the overlap and the contrast of the two atom clouds, and it is expected to have $\rho = 1$ for best interference. ϕ is close to the Sagnac phase $\phi_s = 2(m/\hbar)A\omega_s$, but there are still some small differences which will be discussed later.

4.2.3 Dynamical scale factor and sensitivity

Eq. (4.11) should be optimised for proper (θ_r, ϕ_r). As for an interferometer, our target is to maximise its sensitivity, which is defined as [104]

$$S = \frac{\sqrt{T}}{\sqrt{N}\Sigma(\omega_s)}. \tag{4.13}$$

For correlated atoms, the sensitivity can be improved to the Heisenberg limit which reads $S_{\mathrm{HL}} = \sqrt{T}/[N\Sigma(\omega_s)]$. For the sake of high precision measurement by minimising S, we expect to have large Σ, N, and short interrogation time T. Here Σ is called the dynamical scale factor, defined as

$$\Sigma = \frac{\partial}{\partial\omega_s}\langle\sigma_z\rangle = \frac{\langle\sigma_z\rangle}{\rho}\frac{\partial\rho}{\partial\omega_s} + \rho\sin\theta_r\left[\cos\theta_r\sin(\phi_r-\phi)+\cos(\phi_r-\phi)\right]\frac{\partial\phi}{\omega_s}. \tag{4.14}$$

Considering the symmetry of $\omega_s \to -\omega_s$, $\langle\sigma_z\rangle \to -\langle\sigma_z\rangle$, we have $\frac{\partial\rho}{\partial\omega_s} = 0$ and $\phi = 0$ for $\omega_s = 0$. Therefore, to maximise Σ, (θ_r, ϕ_r) should be chosen to be $(\pi/2, 0)$, and the dynamical scale factor is

$$\Sigma = \rho\cos\phi\frac{\partial\phi}{\partial\omega_s}. \tag{4.15}$$

4.3 Non-interacting BEC

In Eq. (4.12), to let $\phi = \phi_s = 2(m/\hbar)A\omega_s$, one should assume that the trajectories of atoms exactly follow the centre of the trap. This will be violated when the driving speed is so fast that the atoms are *dragged* away from the centre. To correct the enclosed area of the interferometer, we introduced a quasi-static condition balancing centrifugal force and the restoration force of the trap, such that

$$\begin{aligned} & m\omega_p^2 r = m\omega^2(r - R_p) \\ \Rightarrow \quad & A = R_p^2\int_0^T \omega_p(t)\left(\frac{1}{1-[\omega_p(t)/\omega]^2}\right)^2 \mathrm{d}t. \end{aligned} \tag{4.16}$$

When $\omega_p \to 0$, the integral yields $A_\infty = \pi R_p^2$ as expected.

4.3.1 Analytical solution to the 1D model

The analytical solution is important to capture the main features of a system. Conventionally the 1D model on a circle is applied, which goes well when the ring trap geometry is large, atoms are tightly confined, and the driving speed is slow. We start with the 1D model, and its solution inspires us to get the solution to the 2D model shown in the next section.

We start from the simplified the 1D Schrödinger equation

$$\mathrm{i}\frac{\partial}{\partial t}\psi_{1,2}(t,\theta) = \left[-\frac{1}{2R_p^2}\frac{\partial^2}{\partial\theta^2} + \frac{R_p^2}{2}\left(\theta - \Theta_{1,2}(t)\right)^2\right]\psi_{1,2}(t,\theta), \tag{4.17}$$

where $\Theta_{1,2}(t) = \omega_s t \pm \theta_p(t) \mp \pi$ and we let $\hbar = m = \omega \equiv 1$. Here the $\mp\pi$ in $\Theta_{1,2}(t)$ is manually introduced to make the atom clouds move from $\theta = \mp\pi$ to $\theta = 0$ and interfere. As the centre of trap is moving, it is not easy to calculate the ground state before the BECs are splitted. To get rid of this, we need a rotation transformation by introducing unitary operator $\hat{U}_{1,2}(t) = \exp\left[\omega_s t\frac{\partial}{\partial\theta}\right]$. The wavefunction and Hamiltonian will be transformed into

$$\psi'_{1,2}(t,\theta) = \hat{U}_{1,2}(t)\psi_{1,2}(t,\theta), \tag{4.18}$$

$$\hat{H}'_{1,2}(t) = \hat{U}_{1,2}(t)\hat{H}_{1,2}(t)\hat{U}^\dagger_{1,2}(t) + \mathrm{i}\left(\frac{\partial}{\partial t}\hat{U}_{1,2}(t)\right)\hat{U}^\dagger_{1,2}(t). \tag{4.19}$$

This leads to the Hamiltonian in a rotating frame

$$\hat{H}'_{1,2} = -\frac{1}{2R_p^2}\frac{\partial^2}{\partial\theta^2} + \frac{R_p^2}{2}\theta^2 \mp R_p^2\left(\theta_p(t) - \pi\right)\theta + \frac{1}{2}\left(\theta_p(t) - \pi\right)^2 + i\omega_s\frac{\partial}{\partial\theta}. \tag{4.20}$$

Then we introduce the creation and annihilation operators

$$\hat{a} = \frac{1}{\sqrt{2}}\left(R_p\theta + \frac{\partial}{R_p\partial\theta}\right), \quad \hat{a}^\dagger = \frac{1}{\sqrt{2}}\left(R_p\theta - \frac{\partial}{R_p\partial\theta}\right), \tag{4.21}$$

which simplifies Eq. (4.20) to

$$\hat{H}'_{1,2} = \hat{a}^\dagger\hat{a} + \lambda_{1,2}(t)\hat{a}^\dagger + \lambda^*_{1,2}(t)\hat{a} + \xi(t), \tag{4.22}$$

where

$$\lambda(t) = \frac{R_p}{\sqrt{2}}\left[\mp\left(\theta_p(t) - \pi\right) - i\omega_s\right],$$
$$\xi(t) = \frac{1}{2}R_p^2\left[\theta_p(t) - \pi\right]^2 + \frac{1}{2}.$$

We can find that Eq.4.22 generates a coherent state $|\alpha\rangle$ always *coherent* throughout the quench of $\lambda(t)$, $\xi(t)$. Therefore, we can let the temporal state be $\left|\psi_{1,2}\right\rangle =$

$e^{\mathrm{i}\phi_{1,2}(t)}\left|\alpha_{1,2}(t)\right\rangle$, and the E.O.M.s of α and ϕ read

$$\frac{\mathrm{d}}{\mathrm{d}t}\alpha_{1,2}(t) = -i\alpha_{1,2}(t) - i\lambda_{1,2}(t), \tag{4.23a}$$

$$\frac{\mathrm{d}}{\mathrm{d}t}\phi_{1,2}(t) = \xi(t) + \mathrm{Re}\left[\alpha_{1,2}(t)\lambda^*_{1,2}(t)\right]. \tag{4.23b}$$

The ground state at $t = 0$ is $\alpha_{1,2}(0) = -\lambda_{1,2}(0) = R_p/\sqrt{2}(\mp\pi + \mathrm{i}\omega_s)$ and $\phi_{1,2}(0) = 0$, where $\mathrm{i}\omega_s$ refers to the initial speed in the rotating frame. At final time $t = T$, the solution yields

$$\alpha_{1,2}(T) = e^{-iT}\left[-\lambda_{1,2}(0) - i\int_0^T \lambda_{1,2}(t')e^{it'}\mathrm{d}t'\right], \tag{4.24a}$$

$$\phi_{1,2}(T) = \int_0^T \xi(t')\mathrm{d}t' + \int_0^T \mathrm{Re}\left[\alpha_{1,2}(t')\lambda^*_{1,2}(t')\right]\mathrm{d}t'. \tag{4.24b}$$

The overlap integral is therefore $\int \psi^*(\mathbf{r})\psi(\mathbf{r})\mathrm{d}\mathbf{r} = e^{i(\phi_1(T)-\phi_2(T))}\alpha_2^*(T)\alpha_1(T)$.

4.3.2 Analytical solution to the 2D model

A more rigorous analysis must be proposed if the atom cloud width is not far smaller than the ring path, and the driving speed is fast enough that the centrifugal force becomes important. Therefore, we developed a 2D model to fully answer these issues.
Different from Eq.4.17, we consider the 2D Hamiltonian with symmetric trap $\omega_r = \omega_\tau = \omega \equiv 1$,

$$\mathrm{i}\frac{\partial}{\partial t}\psi_{1,2}(t,\mathbf{r}) = \left[-\frac{1}{2}\nabla^2 + \frac{1}{2}\left|\mathbf{r} - \mathbf{R}_p[\Theta_{1,2}(t)]\right|^2\right]\psi_{1,2}(t,\mathbf{r}), \tag{4.25}$$

where $\mathbf{R}_p[\Theta] = R_p(\cos\Theta, \sin\Theta)$ and $\Theta_{1,2}(t) = \omega_s t \pm \theta_p(t)$.
Similar to the 1D case, we need to transform the reference frame to a rotating frame whose angular speed is ω_s to symmetrise and simplify the Hamiltonian. Therefore, we use the unitary operator $\hat{U}_{1,2}(t) = \exp\left[i\omega_s t\hat{L}_z\right] = \exp\left[\omega_s t\left(x\frac{\partial}{\partial y} - y\frac{\partial}{\partial x}\right)\right]$, and the transformed Hamiltonian is

$$\begin{aligned}\hat{H}'_{1,2} &= \hat{U}_{1,2}\hat{H}_{1,2}\hat{U}^\dagger_{1,2} + \mathrm{i}\hat{U}^\dagger_{1,2}\frac{\partial}{\partial t}\hat{U}_{1,2} \\ &= -\frac{1}{2}\left(\frac{\partial^2}{\partial x^2} + \frac{\partial^2}{\partial y^2}\right) + \frac{1}{2}\left(x^2 + y^2 + R_p^2\right) \\ &\quad - R_p x\cos\theta_p(t) \mp R_p y\sin\theta_p(t) + \mathrm{i}\omega_s\left(x\frac{\partial}{\partial y} - y\frac{\partial}{\partial x}\right).\end{aligned} \tag{4.26}$$

Then we introduce the creation and annihilation operators

$$\hat{a} = \frac{1}{2}\left(x + \mathrm{i}y + \frac{\partial}{\partial x} + \mathrm{i}\frac{\partial}{\partial y}\right),\ \hat{a}^\dagger = \frac{1}{2}\left(x - \mathrm{i}y - \frac{\partial}{\partial x} + \mathrm{i}\frac{\partial}{\partial y}\right),$$

$$\hat{b} = \frac{1}{2}\left(x - \mathrm{i}y + \frac{\partial}{\partial x} - \mathrm{i}\frac{\partial}{\partial y}\right),\ \hat{b}^\dagger = \frac{1}{2}\left(x + \mathrm{i}y - \frac{\partial}{\partial x} - \mathrm{i}\frac{\partial}{\partial y}\right),$$

which simplify Eq. (4.26) to

$$\hat{H}'_{1,2} = (1+\omega_s)\,\hat{a}^\dagger\hat{a} + (1-\omega_s)\,\hat{b}^\dagger\hat{b} + 1 + \frac{R_p^2}{2} - \frac{R_p}{2}\left(\hat{a}e^{\mp\mathrm{i}\theta_p} + \hat{b}e^{\pm\mathrm{i}\theta_p} + \mathrm{H.c.}\right). \quad (4.27)$$

We also found the solution in coherent state basis $e^{\mathrm{i}\phi}\,|\alpha,\beta\rangle$, where α and β correspond to $\hat{a}$ and $\hat{b}$. The E.O.M.s of α, β, and the global phase ϕ read

$$\frac{\mathrm{d}}{\mathrm{d}t}\alpha_{1,2} = -\mathrm{i}\,(1+\omega_s)\,\alpha_{1,2} + i\frac{R_p}{2}e^{\pm i\theta_p}, \quad (4.28a)$$

$$\frac{\mathrm{d}}{\mathrm{d}t}\beta_{1,2} = -\mathrm{i}\,(1-\omega_s)\,\beta_{1,2} + i\frac{R_p}{2}e^{\mp\mathrm{i}\theta_p}, \quad (4.28b)$$

$$\frac{\mathrm{d}}{\mathrm{d}t}\phi_{1,2} = \frac{R_p}{2}\mathrm{Re}\left[\alpha_{1,2}e^{\mp\mathrm{i}\theta_p} + \beta_{1,2}e^{\pm\mathrm{i}\theta_p}\right]. \quad (4.28c)$$

By directly integrating these equations, where initial states are ground states with $\theta_p = 0$, one will get the analytical solution

$$\alpha_{1,2}(T) = \frac{R_p}{2(1+\omega_s)}\left[1 - \mathrm{i}\int_0^T \dot{\theta}_p(t')e^{\mathrm{i}(1+\omega_s)(t'-t)\pm\mathrm{i}\theta_p(t')}\mathrm{d}t'\right], \quad (4.29a)$$

$$\beta_{1,2}(T) = \frac{R_p}{2(1-\omega_s)}\left[1 + \mathrm{i}\int_0^T \dot{\theta}_p(t')e^{\mathrm{i}(1-\omega_s)(t'-t)\mp\mathrm{i}\theta_p(t')}\mathrm{d}t'\right], \quad (4.29b)$$

$$\phi_{1,2}(T) = \frac{R_p}{2}\mathrm{Re}\left[\int_0^T \alpha_{1,2}(t')e^{\mp\mathrm{i}\theta_p(t')} + \beta_{1,2}(t')e^{\pm\mathrm{i}\theta_p(t')}\mathrm{d}t'\right]. \quad (4.29c)$$

Thus the overlap becomes

$$\begin{aligned}\int \psi_1(\mathbf{r})\psi_2^*(\mathbf{r})\mathrm{d}\mathbf{r} &= e^{\mathrm{i}(\phi_1-\phi_2)}\,\langle\alpha_2 \mid \alpha_1\rangle\,\langle\beta_2 \mid \beta_1\rangle \\ &= e^{\mathrm{i}\left[\phi_1-\phi_2+\mathrm{Im}(\alpha_2^*\alpha_1+\beta_2^*\beta_1)\right]}e^{-\frac{1}{2}(|\alpha_1-\alpha_2|^2+|\beta_1-\beta_2|^2)}\end{aligned} \quad (4.30)$$

with all quantities evaluated at $t = T$. The parameters ρ and ϕ are respectively

$$\rho = \exp\left[-\frac{R_p^2}{2}\left(\left|\int_0^T \sin\theta_p(t')e^{\mathrm{i}(1+\omega_s)(t'-T)}\mathrm{d}t'\right|^2 + \left|\int_0^T \sin\theta_p(t')e^{\mathrm{i}(1-\omega_s)(t'-T)}\mathrm{d}t'\right|^2\right)\right], \quad (4.31a)$$

$$\begin{aligned}\phi = {} & R_p^2\int_0^T\left(\frac{\sin(1-\omega_s)t'}{1-\omega_s} - \frac{\sin(1+\omega_s)t'}{1+\omega_s}\right)\sin\theta_p(t')\mathrm{d}t' \\ & + R_p^2\int_0^T\int_0^{t'}\sin\left[\theta_p(t'') - \theta(t')\right]\sin\omega_s(t''-t')\sin(t''-t')\mathrm{d}t''\mathrm{d}t'.\end{aligned} \quad (4.31b)$$

To make a benchmark, we first consider the driving function is linear $\theta_p(t) = (\pi/T)\times t$, and the radius of the ring path is $R_p = 10$. ρ has a dramatic oscillation in small interrogation time $T < 40$ from 0 to 1. The derivative of interference phase ϕ has a descending trend that saturates to $2A_\infty$ for large T, where $A_\infty = \pi R_p^2$. Consequently, the

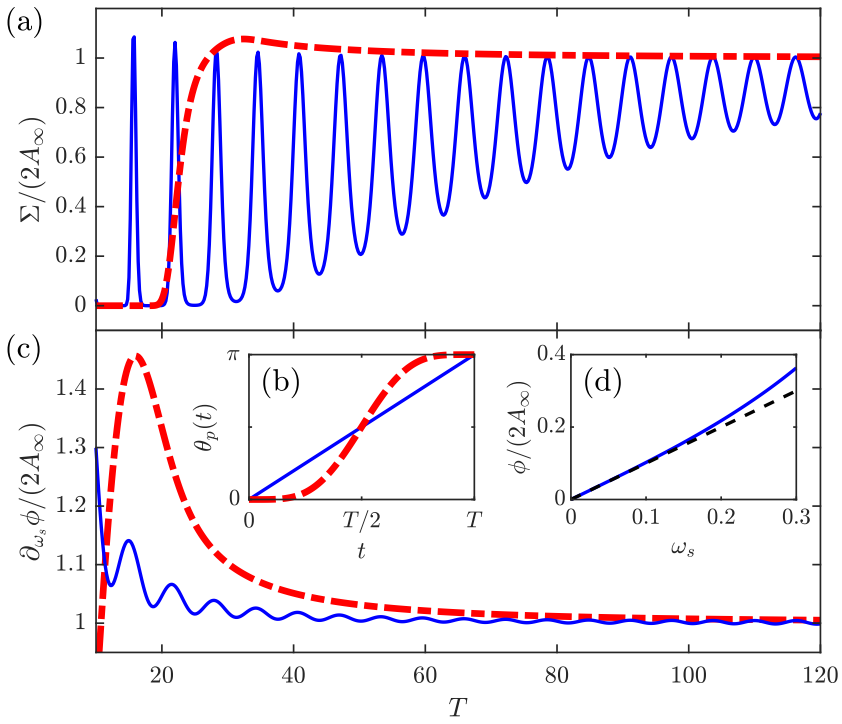


Figure 4.3: (a) The dynamical scale factor for linear (blue solid) and nonlinear (red dashed) driving. (b) The driving function for the linear and nonlinear profile. (c) The interference phase ϕ. (d) Benchmark of the interference phase for a wide range of ω_s under linear driving and $T = 100$. The radius of the ASI path is $R_p = 10$.

dynamical scale factor has a comb profile over interrogation time, and finally reach the classical limit $\Sigma_c = 2A_\infty$ [Fig.4.3a].

Eq. (4.31) is also suitable for arbitrary driving function $\theta_p(t)$. We propose a nonlinear driving function $\theta_p \sim t^4(1-t/T)^4$ as shown in Fig. 4.3(b), and the results are compared with the linear driving as shown in Fig. 4.3(a,b). The dynamical scale factor is clearly smoothed as the overlap ρ reaches 1 nearly at $T \approx 30$. The phase ϕ is also descending, but its peak is larger than the linear driving.

Before we go to the detailed optimisation of $\theta_p(t)$, we verify the linearity of ϕ as a function of ω_s. In Fig. 4.3(d), we show the interference phase ϕ at a large range of ω_s from 0 to 0.3. The phase has accumulated to $\sim 36 \times 2\pi$ for $\omega_s = 0.3$. Nevertheless, if we restrict the working condition $\phi < 2\pi$ to avoid multiple turns of interference, the linear relation between ϕ and ω_s is a good approximation.

In addition, we present some experimental parameters relevant to this study. Using ^{87}Rb as an example, the TAAP traps [99] can confine the atoms in the radial direction at frequency $\omega_r \approx 2\pi \times 127$ Hz and $\omega_z \approx 2\pi \times 206$ Hz in the z-direction. The unit time, length, and energy under such condition are $t_s = 1.26$ ms, $l_s = 1.70$ μm, and $E_s = 8.35 \times 10^{-32}$ J, respectively. The scattering length of ^{87}Rb is $a_s \approx 98$ a_0, a_0 being the Bohr radius, for both $|F = 1\rangle$ and $|F = 2\rangle$ states and their interstate interactions [103].

In the 2D model, the effective interaction strength is $g_{ij} = N\sqrt{m\omega_z/2\pi\hbar}(4\pi\hbar^2/m)a_{ij}$, where N is the number of atoms [102]. Using E_s and l_s as the units, we obtain $g = 4.39\times 10^{-3}\ NE_s l_s^2$. The number of atoms in the BECs can change the relative interaction strength. For example, the dimensionless interaction strength will be $g = 43.9$ for 10^4 atoms.

4.3.3 Optimisation of the driving field

According to Eq. (4.31), the maximal sensitivities can be reached when the driving function $\theta_p(t)$ satisfies $\int_0^T \sin[\theta_p(t)]e^{it}\mathrm{d}t = 0$, such that $\rho = 1$ for $\omega_s = 0$. Here we note that the optimal condition is different for 1D model where $\int_0^T \omega_p(t)e^{it}\mathrm{d}t = 0$. They will result in different maximal interrogation times [105]. As aforementioned, we introduce a trial driving function with a form

$$\theta_p(t) = \frac{\pi}{B(a+1,b+1)}\int_0^t \left(\frac{t'}{T}\right)^a \left(1-\frac{t'}{T}\right)^b \mathrm{d}t', \tag{4.32}$$

where $B(a,b)$ is the Beta function to satisfy the boundary condition $\theta_p(T) = \pi$ and a, b are optimising parameters. This function has been applied to other optimisation problems, e.g., conformal antenna array [106]. With this choice, $\omega_p(t)\dot{\theta}_p(t)$ has a single peak, whose width is characterised by $a+b$, and the central position by $a-b$. This means that the BECs will experience smooth acceleration and deceleration at the beginning and the end of driving. This function is also normalised to π such that the BECs will travel a half of the ring during the interrogation time. In principle, a and b should be chosen carefully for each interrogation time to satisfy the optimal condition. However, we will show that ρ can be achieved very close to 1 for a wide range of interrogation time by a single choice of a and b.

To measure qualities of the optimisation quantitatively, we introduce a cost function

$$\xi = \ln(1-\rho), \tag{4.33}$$

which approximately has $\xi(0) \approx R_p^2\left|\int_0^T \sin\theta_p(t')e^{it'}\mathrm{d}t'\right|^2$ for $\omega_s = 0$ and $\rho \approx 1$. The smaller the value of ξ is, the better the optimisation will be. The cost function is proportional to R_p^2, which means the same driving function will work less good as the radius of path increases. In Fig. 4.4, we show three examples of the cost function with $T = 20, 50, 100$. As shown in Fig. 4.4(a), the optimisation can not improve sensitivities much when T is small, except for a small region around $a = b = 2$. The optimisation works particularly well with larger interrogation time, as shown in the example with $T = 50, 100$ [Fig. 4.4(b,c)]. In these cases, the cost function shows multiple minimal regions. For example, we find five such areas (green dots) in Fig. 4.4(b), and even more and wider area in Fig. 4.4(c). We also show a contour of $\xi = -6.9$ which means

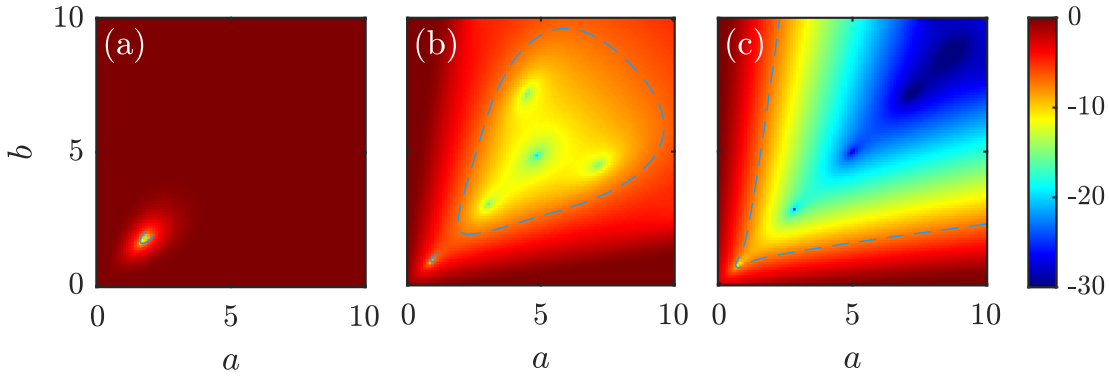


Figure 4.4: The cost function $\xi = \ln(1-\rho)$ for various parameters a and b. The path radius $R_p = 10$, and the interrogate time T is (a) 20, (b) 50, (c) 100. The contour lines enclose the area for $\rho > 99.9\%$.

$\rho > 99.9\%$ in Fig. 4.4, and it can be found that its enclosed area is growing for a longer T.

4.4 Interacting BEC

So far, we have focused on the non-interacting BEC. The effects of atomic interactions are still unclear. In this section, we will numerically solve the nonlinear GPE and make a comparison with the non-interacting cases. We will show the different influence of the inter- and intra-state interactions, as well as the effects of anisotropic trapping potentials.

4.4.1 Numerical solver for GPE

In this work, we solve GPE by time-splitting spectral method (TSSP) [107, 108]. For linear time-independent Schrödinger equation, one can obtain the wave function by $\psi(t) = \exp\left(-i\hat{H}t\right)\psi(0)$. However, as our Hamiltonian is nonlinear and time-dependent, we need to update the Hamiltonian at each time step. We summarise this method as below.

First, we need to split the Hamiltonian by part. According to the simplest Strang splitting approach, the Hamiltonian reads

$$\hat{H} = \frac{1}{2}\hat{V} + \hat{T} + \frac{1}{2}\hat{V}, \tag{4.34}$$

where $\hat{T} = -\frac{\hbar^2}{2m}\nabla^2$ is the kinetic energy, $\hat{V} = V(\mathbf{r}) + g|\psi(\mathbf{r})|^2$ is the external trapping potential plus the nonlinear interaction term. Then we can calculate the evolution of the wave function over one time-step, dt, from $\psi_i(\mathbf{r})$ to $\psi_f(\mathbf{r})$ as

$$\psi_j(\mathbf{r}) = e^{-i\frac{1}{2}\hat{V}dt}\psi_i(\mathbf{r}),$$

$$\begin{aligned}
\tilde{\psi}_j(\mathbf{k}) &= \mathcal{F}\left[\psi_j(\mathbf{r})\right], \\
\tilde{\psi}_j(\mathbf{k}) &= e^{-\mathrm{i}\hat{T}_\mathbf{k}\mathrm{d}t}\,\tilde{\psi}_j(\mathbf{k}), \\
\psi_k(\mathbf{r}) &= \mathcal{F}^{-1}\left[\tilde{\psi}_j(\mathbf{k})\right], \\
\psi_f(\mathbf{r}) &= e^{-\mathrm{i}\frac{1}{2}\hat{V}\mathrm{d}t}\,\psi_k(\mathbf{r}),
\end{aligned}$$

where $\hat{T}_\mathbf{k} = \frac{\hbar^2}{2m}|\mathbf{k}|^2$, $\mathcal{F}$ refers to the Fourier transformation. The advantage appears as follows. Although the matrix exponential of the Hamiltonian is time-consuming, in this method, we only need to calculate the matrix exponential of $\hat{V}(\mathbf{r})$ and $\hat{T}_\mathbf{k}$, which are diagonal in real and momentum space, respectively. Then the matrix exponential is thereby reduced to the element-wise exponential, and speeds up the calculation significantly.

In our work, the matrix of $\hat{T}_\mathbf{k}$ can be pre-stored, the Fourier transformation is powered by *Fast Fourier Transformation* [109], but $\hat{V}$ needs to be updated step-by-step. In order to reduce the cost of memory, our solving domain is only a few times of the size of the wave packet, and moving alongside the motion of the trapping centre.

Furthermore, we also quote that the TSSP method can be improved by involving the adaptive time step [110] and high-order slitting [111, 112], which is similar to Runge-Kutta methods. For the special cases of harmonic oscillators, it is also feasible to apply Hermite spectral instead of Fourier spectral method by replacing $\hat{T} = \frac{1}{2m}p^2$ to $\hat{T} = \frac{1}{2m}p^2 + \frac{1}{2}\hbar^2\omega^2x^2$ [112].

As a demonstration, we show the wave functions of the two BEC components of the ASI at the end of transport $t = T$, with comparison before and after the second $\pi/2$-pulse applied for the conversion of particle numbers. We plotted the column density, I, projected to the tangent direction, $\tilde{\tau}$, in Fig. 4.5. We let $R_p = 10$, $T = 100$, and $\omega_s = 10^{-3}$.

Before the second $\pi/2$-pulse is applied, the wave functions of non-interacting BECs are close to the Gaussian function. If the intra-state interaction (g_{11}, g_{22}) is triggered-on [Fig. 4.5(b,c)], and whatever the inter-state interaction g_{12} is zero or not, the wave functions are more flattened. But if $g_{11} = g_{22} = 0$ and $g_{12} \neq 0$ [Fig. 4.5(d)], the wave functions are sharper than where $g_{11}, g_{22} \neq 0$.

After the second $\pi/2$-pulse, the atom population is converted, in this case, from $|2\rangle$ to $|1\rangle$. As the wave functions of the two components are shifted oppositely from the trap centre, the conversion is incomplete. With the existence of atomic interactions [Fig. 4.5(b,c,d)], we can find that the conversion is suppressed. Comparing the effects of intra- [Fig. 4.5(c)] and inter-state [Fig. 4.5(d)] interactions, we can find the latter has more influence on the dynamics and recombination of the two atom clouds. This will be shown in more details in the next section.

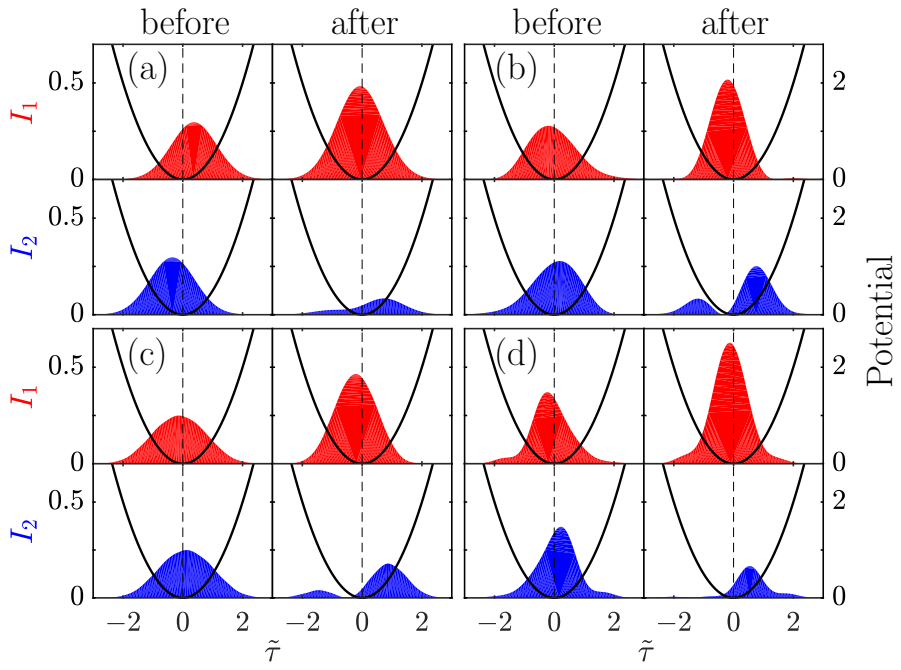


Figure 4.5: Column densities of the BEC components projected on the $\tilde{\tau}$ direction. Density snapshots of the states $|1\rangle$ (upper row) and $|2\rangle$ (lower row) immediately before and after the second (recombination) $\pi/2$ pulse are shown in each panel. Panels correspond to different interaction strengths: (a) $g_{11} = g_{22} = g_{12} = 0$, (b) $g_{11} = g_{22} = g_{12} = 30$, (c) $g_{11} = g_{22} = 30$, $g_{12} = 0$, and (d) $g_{11} = g_{22} = 0$, $g_{12} = 30$. The parameters used in the calculations are $\omega_r = \omega_\tau = 1$, $T = 100$. The trapping potential (solid) and trap center (dashed) along the $\tilde{\tau}$ axis are shown.

4.4.2 Effects of interactions and asymmetric trap

Having discussed the interaction-free cases, we now move our focus to the interacting BECs. In particular, we will show that the optimisation used in Eq.4.32 also works for the latter. We choose the parameters $a = b = 4$. In Fig. 4.6, numerical examples of the dynamical scale factors, Σ, and the gradient of interference phase, $\partial_{\omega_s}\phi$, are presented for different interaction strengths when the trap is symmetric or anisotropic. According to the correction of centrifugal force by Eq. (4.16), we plotted the reference values for $\partial_{\omega_s}\phi = 2A$ as the solid line. It can be seen that they are very close to the results of numerical simulations. For further improvement, we calculated the area swept by the wave packet, where r in Eq. (4.16) should be treated as $r = \langle\hat{r}\rangle$. As plotted with the dashed lines, this is closer to the numerical results. We can also find that the interference phase ϕ has little dependency on the interactions or trapping potentials.

In the isotropic trap and with symmetric interaction ($g_{11} = g_{22} = g_{12} = g$) as shown in Fig. 4.6(a), we find the dynamical scale factor is similar to the non-interacting case when $T < 20$ or $T > 100$. In the former range, ρ rises from 0 to 1, and saturate to 1 in the latter. In the intermediate range $20 < T < 70$, however, the dynamical scale factor oscillates between a maximal and minimal value, which is obviously different from the

non-interacting case. The amplitudes of the oscillation also increase as g increases. This suggests that the collective motions are excited during the transport, which inhibits the two-component BECs fully overlap for interference.

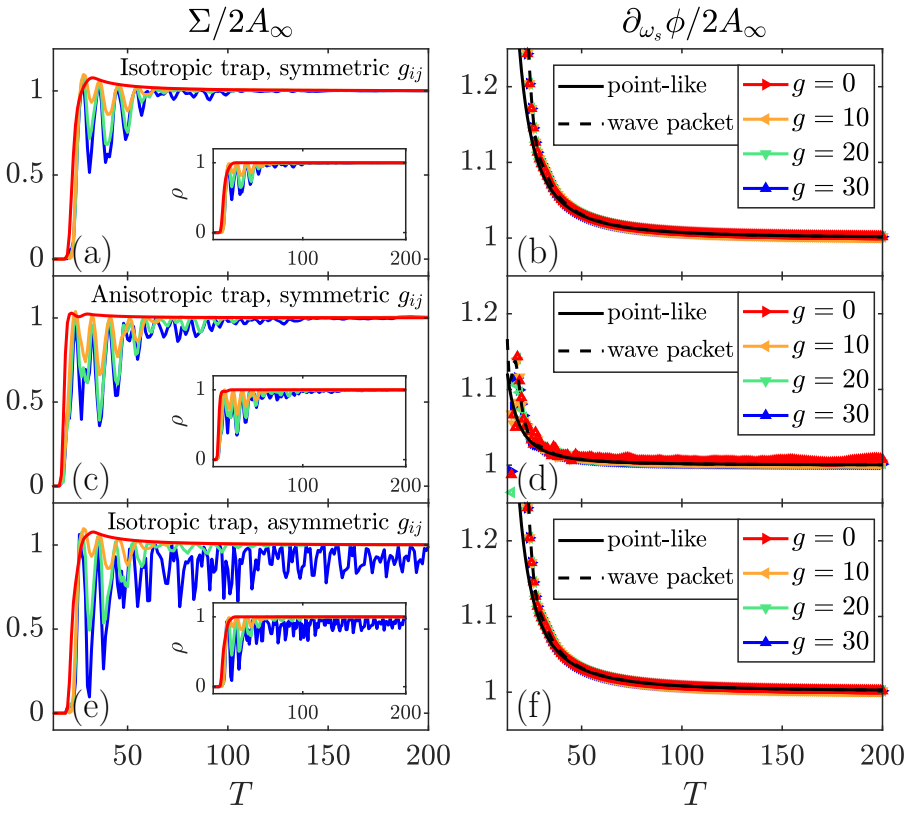


Figure 4.6: Role of trap anisotropy and interactions. Dynamical scale factors, normalised to the static value (left column) and phase gradient (right column), as a function of interrogation time T for the driving function parameters $a = b = 4$. We consider three cases: (a), (b) symmetric interactions $g_{11} = g_{22} = g_{12} = g$ and isotropic traps $\omega_r = \omega_\tau = 1$; (c), (d) symmetric interactions $g_{11} = g_{22} = g_{12} = g$ and anisotropic traps $\omega_r = 1$, $\omega_\tau = 0.5$; (e), (f) asymmetric interactions $g_{11} = g_{22} = 10$, $g_{12} = g$ and isotropic traps $\omega_r = \omega_\tau = 1$. Insets in the left panels show the overlap ρ. The phase gradients are displayed together with numerical calculations of the path-enclosed area for a classical pointlike particle (black solid lines) and an average over the BEC wave packets (dashed lines).

Then we show two different situations. First, we break the trapping symmetry. In particular, we focus on a shallower trap along the tangent direction, such that $\omega_\tau = \frac{1}{2}\omega_r = \frac{1}{2}\omega$. The corresponding dynamical scale factors, Σ, are shown in Fig. 4.6(c). Compared to the isotropic trap, the deduction of the Σ with finite atomic interaction is more significant, and the minimum interrogate time T for saturated ρ is slightly bigger. Second, we also examined the changes when the interactions are not symmetric, and we fix $g_{11} = g_{22} = 10$, vary g_{12} from 0 to 30. Such situations can be realised, for example, through Feshbach resonance [16]. As shown in Fig. 4.6(e), the dynamical scale factor behaves similar to the symmetric interaction configuration for $g_{12} \leqslant 20$, but

the oscillation of Σ is drastic for $g_{12} = 30$. Here we recall the observation in Fig. 4.3, where the dominating g_{12} can significantly change the dynamics of BECs, and the full spatial overlap is inhibited, even at very large interrogate time $T \approx 100$.
Therefore, we conclude that the inter-state interaction is the main reason for the drop in the dynamical scale factor of ASI. Increasing the intra-state interaction over the inter-state interaction can sufficiently suppress the effects caused by the latter. To maintain the isotropy of the trap is also crucial for the robustness of the interference.

Chapter 5

Project: Quench Dynamics of Extended Bose-Hubbard Model

With optical lattices, it is possible to simulate quantum many-body physics that are encountered in condensed matter systems. Due to the high controllability, it is even more interesting that some exotic physical states can be observed and engineered beyond ordinary solid-state systems [113–115]. For example, the well-known superfluid-Mott insulator (SF-MI) transition was observed in optical lattice [116, 117]. Recently, the use of long-range interactions (LRI) made it possible to study the Supersolid (SS) and density wave (DW) phases, which are hard to be found directly in solid-state systems [118–127]. There are many studies on the dynamics of atoms in optical lattices, including Landau-Zener transitions [128–130], Kibble-Zurek mechanism (KZM) [131–137], transport [138–140], excitations of Higgs and Goldstone modes [141, 142].
In this chapter, we will explore the dynamics of bosonic atoms in a 2D square optical lattice under the quench of the lattice depth, such that the system evolves from MI to SF through KZM. The long-range interactions are triggered using Rydberg-dressing (Chapter 3). The SS and DW phases may then appear during the dynamics.

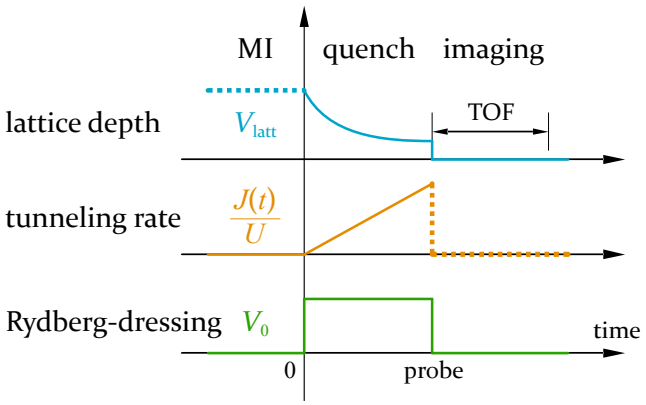


Figure 5.1: Quench Scheme. (1) prepare an ideal Mott-insulator phase with unit filling in a deep lattice (2) reduce the lattice depth to ramp up the tunnelling rate as $J(t)/U = a_Q t$, meanwhile turn on the LRI (3) remove all the external fields for time-of-flight interference and imaging.

As introduced in Chapter 2, we describe atoms on optical lattices with the extended Bose-Hubbard Model (eBHM). The Hamiltonian reads

$$H = -J(t)\sum_{\langle i,j\rangle}\hat{b}_i^\dagger\hat{b}_j + \sum_i\left[\frac{U}{2}\hat{n}_i(\hat{n}_i-1)-\mu\hat{n}_i\right] + \sum_{i<j}V_{ij}\hat{n}_i\hat{n}_j, \tag{5.1}$$

where $\langle i,j\rangle$ restricts the hopping between sites i and j to the nearest-neighbouring only. The LRI term V_{ij} depicts the tail of Rydberg-dressing which reads

$$V_{ij} = V_0\frac{2}{(r_{ij}/r_c)^6+1}. \tag{5.2}$$

Here the factor 2 in the numerator is manually introduced, such that it is more comparable to the box-type potential approximation:

$$V_{ij} = V_0\Theta(r_c - r_{ij}), \tag{5.3}$$

where Θ is the Heaviside function [$\Theta(0)=1$]. When r_c is equal to the lattice constant, the box-type potential is the same as the nearest-neighbour interaction, and its phase transitions and dynamics have been discussed in many papers, for example [40, 122, 135, 136].

As shown in Fig. 5.1, the depth of the optical lattice can be subtly reduced, and the hopping parameter J is ramped up from (near) zero linearly to a sufficiently large value, where the final state is expected in SF phase. The Rydberg-dressing strength is turned on and keep constant during the quench.

In Section 5.1, we will introduce the Gutzwiller ansatz, which enables us to simulate the dynamics numerically. In Section 5.2, we show the phase diagrams of eBHM. In Section 5.3, we introduce the Kibble-Zurek mechanism (KZM). Finally, in Section 5.4, we show our main results of the dynamics. We will focus on the evolution of superfluid density and the particle density modulation. We also take advantage of the time-of-flight (TOF) interference, which leads to the possible experimental observables for these quantities.

5.1 Gutzwiller ansatz

Gutzwiller ansatz (or Gutzwiller approximation, GA) refers to a variational approach to solving molecular and many-body systems, typically the Hubbard model [143, 144], Haldane-Shastry model [145, 146] and Landau's Fermi-liquid theory [147]. The idea of introducing Gutzwiller wave function (GWF) is to interpolate the ground state from non-interacting limit to highly interacting limit. Formally, let Ψ_0 be the ground state of

free particle, the GWF is created by finding a projector such that $\Psi_G = \hat{P}_G \Psi_0$, and

$$\hat{P}_G = \prod_i \sum_{\Gamma_i} \lambda_{\Gamma_i} |\Gamma_i\rangle\langle\Gamma_i| , \tag{5.4}$$

where $\{|\Gamma_i\rangle\}$ is a set of local states on the i-th lattice point, and λ_{Γ_i} is the variational coefficient. It is expected that the highly interacting states, such as doubly or multiply occupation, are less weighted to minimise the total energy.

As for BHM, $|\Gamma_i\rangle$ can be chosen to be the Fock state, and we can replace λ_{Γ_i} by f_m^i, which results in the GWF being [36, 148]

$$|\Psi\rangle_G \simeq \prod_i \sum_m f_m^i |i,m\rangle . \tag{5.5}$$

The coefficients f_m^i must follow the local normalisation condition $\sum_m \left|f_m^i\right|^2 = 1$. The E.O.M. of f_m^i can be derived from the Schrödinger equation [Appendix. B.1]:

$$\mathrm{i}\dot{f}_m^i = -J\Phi_i\sqrt{m} f_{m-1}^i - J\Phi_i^*\sqrt{m+1} f_{m+1}^i + \left[\frac{U}{2}m(m-1) + m\left(\sum_j V_{ij} n_j - \mu\right)\right] f_m^i . \tag{5.6}$$

where $\Phi_i = \sum_{\langle j\rangle_i} \phi_j$ is the sum of the superfluid (SF) orders of the nearest sites around i. The SF order is defined by $\phi_j = \langle\psi_j|\hat{b}_j|\psi_j\rangle$, and $n_j = \langle\psi_j|\hat{n}_j|\psi_j\rangle$ is the occupation number. From then on, we will let $U \equiv 1$ for convenience.

For real-time simulation of the quench process, our initial state is unit-filled Mott insulator, i.e., $f_1^i = 1$ and $f_m^i = 0$ for $m \neq 0$. To take the random phase into consideration, we let $f_1^i = e^{\mathrm{i}\theta_0^i}$, where $\theta_0^i \in [0, 2\pi)$ is random for each site. We also applied a small fluctuation to other terms with $m \neq 1$ to trigger the initial evolution. Finally, multiple (~ 40 in this work) trajectories were launched and the physical variables were obtained by averaging all trajectories.

Besides, Eq. (5.6) can also be derived from the mean-field theory by decoupling the operators, such as $\hat{b}_i^\dagger \hat{b}_j \approx \phi_i^* \hat{b}_j + \phi_j \hat{b}_i^\dagger - \phi_i^* \phi_j$ [149]. Therefore, GA is also known as Gutzwiller mean-field theory.

The ground state can be achieved by the imaginary time evolution method. Replacing $\mathrm{i} = \sqrt{-1}$ on the LHS of Eq. (5.6) to -1, and renormalising the wave function for each imaginary time step, such as $|\psi_i(t+\Delta t)\rangle = |\psi_i(t+\Delta t)\rangle / \langle\psi_i(t+\Delta t)|\psi_i(t+\Delta t)\rangle$, one can eventually reach the ground state of the system. For canonical ensemble, the total occupation is fixed to be a constant and the chemical potential μ is undetermined. One needs to modify μ for searching the desired filling factor. This can be realised by the bisection method or, more generally, the Nelder-Mead algorithm.

Furthermore, we note that the particle number during the real-time evolution is automatically conserved in the complete Fock state basis, analytically. In numerical simulation,

the particle number conservation is also valid when the upper bound of occupation is large enough.

5.2 Phase diagram of the extended Bose-Hubbard model

In Sec. 2.3, we have presented the MI-SF phase transition in the BHM. In the language of spontaneous symmetry breaking, SF appears when the $U(1)$ symmetry is broken and the SF order $\phi \neq 0$. In the eBHM, it is crucial to consider the breaking of the spatial translational symmetry (STS). Generally, the STS breaking leads to the density modulation, and the density-modulated insulating phase is called the density wave (DW) phase. As for the coexistence of non-zero SF order and density modulation, the state of matter is called the supersolid (SS) phase.

Following Chapter 2, we use the superfluid fraction $\rho_s = (1/M)\sum_{\langle i,j\rangle} \phi_i^* \phi_j$ (Eq. (2.27)) to characterise the superfluidity. The density wave is generally depicted by the structure factor

$$S(\mathbf{k}) = \frac{1}{M}\sum_i e^{\mathrm{i}\mathbf{k}\cdot\mathbf{r}_i} n_i, \tag{5.7}$$

which is essentially the Fourier transform of the density from real space to momentum space. Usually, there are only a few discrete points in the momentum space where $S(\mathbf{k})$ is non-zero. For example, when the interaction is applied to the nearest sites only, the structure factor only peaks at $\mathbf{k} = \pi/d(\pm 1, \pm 1)$, which creates the checkerboard pattern in real space. The peak at the original point $\mathbf{k} = \mathbf{0}$ is trivial in all cases. However, if the interaction length grows, the positions of the peaks will change, and generally hard to predict. Before we discuss this in the next section from the roton instability perspective, we first introduce the mean density variance

$$\sigma = \sqrt{\langle \hat{n}^2 \rangle - \langle \hat{n} \rangle^2}, \tag{5.8}$$

where $\langle \cdot \rangle$ is the quantum expectation value of each site then averaged for the whole real space. This allows us to include any kind of density wave and signifies the boundaries between MI and SF, or DW and SS.

We examined the ground-state phase diagrams for the box interaction by a similar method to Ref. [40]. It was shown that the ground state exhibits MI, DW, SS and SF phases by varying hopping, on-site and LRI. We calculate the phase diagram with average particle number in each site $n_i = 1$. One example of the box-type interaction with $r_c = d$ is shown in Fig. 5.2(a). d is the lattice constant. When the tunnelling and V_0 are weak, the ground state is a MI. Starting from the MI, the system undergoes an MI-SF phase transition when J increases. With larger V_0, the ground state enters DW phases when the hopping is small. We find a DW-SS and then SS-SF transition by

increasing hopping J [150]. More cases and discussions of the phase diagram can be found in [40]. In the case of soft-core interactions, the phase diagram has a similar profile. In Fig. 5.2(b), we give one example for $r_c = 2.5d$. In this case, the SS phase region becomes larger in the parameter space due to the longer-range interaction.

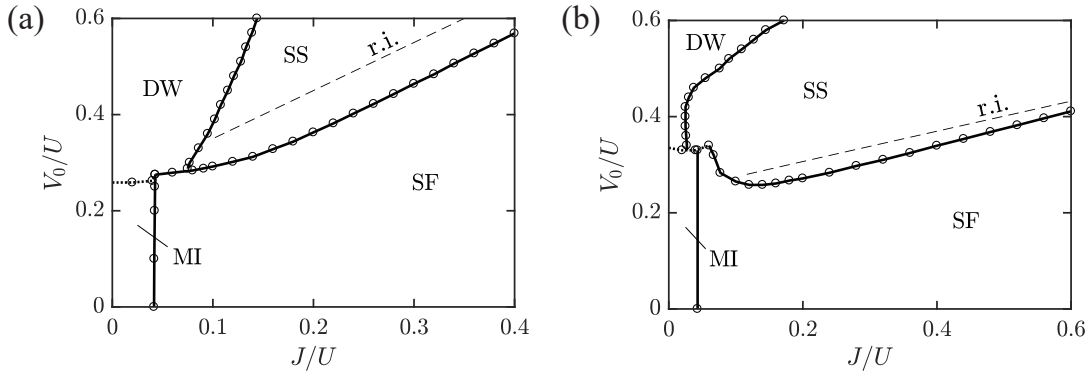


Figure 5.2: Phase diagrams of the extended BHM: (a) for box-type interaction with $r_c = d$, (b) for soft-core interaction with $r_c = 2.5d$. The filling factor is 1.

5.2.1 Roton instability

The emergence of the SS phase can be further analyzed using the Bogoliubov theory. In the SF region, the ground state is a homogeneous condensate, while SS leads to spatial modulations in the condensate. When this happens, the Bogoliubov spectrum of the homogeneous SF phase [151, 152],

$$E(\mathbf{k}) = \sqrt{\varepsilon(\mathbf{k})^2 + \rho_0 \varepsilon(\mathbf{k}) \left(U + \tilde{V}(\mathbf{k})\right)}, \tag{5.9}$$

becomes unstable. Here $\varepsilon(\mathbf{k}) = 2J\left[2 - \cos(k_x d) - \cos(k_y d)\right]$ is the kinetic energy term, ρ_0 is the condensate density and $\tilde{V}(\mathbf{k}) = \frac{1}{M}\sum_{i\neq j} V_{ij} \exp(i\mathbf{k}\cdot\mathbf{r}_{ij})$, is the Fourier transform of the LRI. In free space, $\tilde{V}(\mathbf{k})$ is calculated analytically, which yields $\tilde{V}(\mathbf{k}) = V_0 \frac{2\pi r_c}{|\mathbf{k}|} J_1(|\mathbf{k}|r_c)$ for the box interaction and $\tilde{V}(\mathbf{k}) = V_0 \frac{4\pi r_c^2}{3} \sum_{m=0,\pm 1} e^{i2m\pi/3} K_0(e^{im\pi/3}|\mathbf{k}|r_c)$ for the soft-core interaction, where $J_n(x)$ is the first kind of Bessel function and $K_n(x)$ is the second kind of modified Bessel function [153].

When the LRI is strong, the negative components of $\tilde{V}(\mathbf{k})$ cause a roton instability. Here the Bogoliubov spectra $E(\mathbf{k})$ becomes imaginary. The critical hopping (i.e. the lower bound) to observe the roton instability is $J_l = -\min[\Sigma(\mathbf{k})]$, where

$$\Sigma(\mathbf{k}) = \rho_0 \frac{U + \tilde{V}(\mathbf{k})}{2 - \cos(k_x d) - \cos(k_y d)}. \tag{5.10}$$

A typical $\Sigma(\mathbf{k})$ for the soft-core interaction with $r_c = d$ and $V_0 = 0.6U$ is shown in

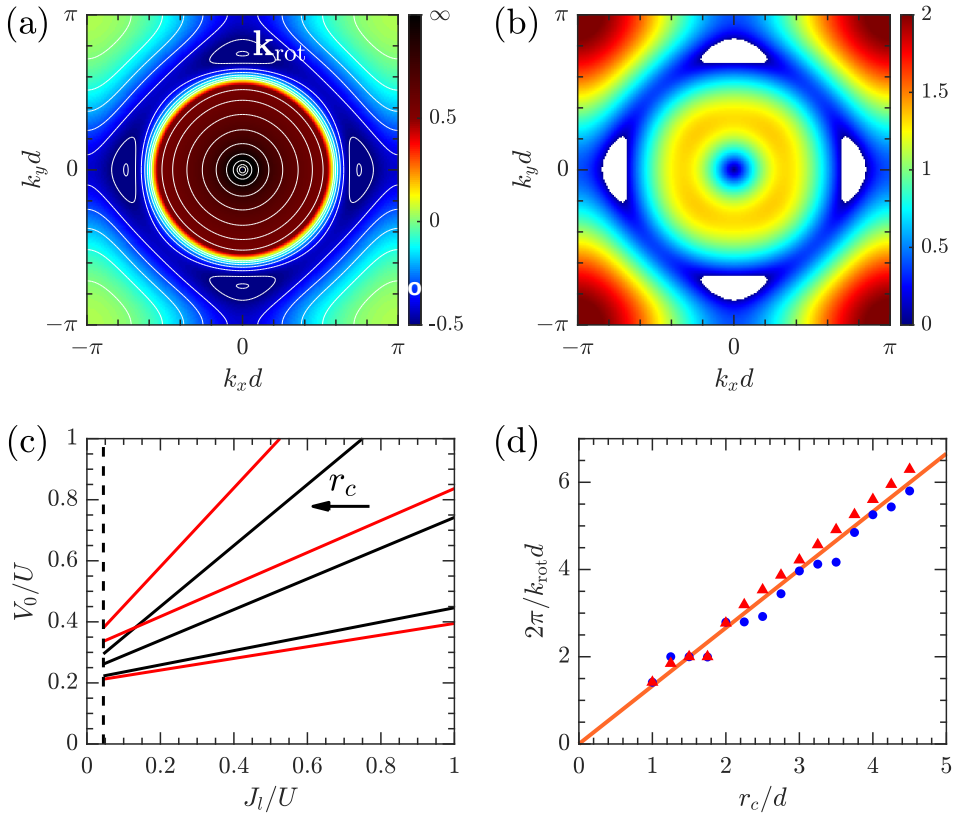


Figure 5.3: (a) The function $\Sigma(\mathbf{k})$ as defined in Eq. (5.10). The valleys signify the momentums where roton instability appears. (b) Bogoliubov spectrum for elementary excitations. The white areas are roton instability. The interaction for (a,b) are set to be soft-core shaped with $r_c = d$ and $V_0 = 0.6U$. (c) The critical value of V_0 for observing roton instability $J_l = -\min[\Sigma(\mathbf{k})]$. Black lines represent for the box-type and red lines for the soft-core interactions, whose interaction lengths are 1, 2, 3, increasing following the arrow. (d) The position of the roton instability versus the interaction lengths. Blue squares are for the box-type red triangles for soft-core interactions. The orange line is a linear fitting $k_{\rm rot} = 3\pi/(2r_c)$.

Fig. 5.3(a). When $J = 0.5U$, the roton instabilities are triggered and shown in the white area in the Bogoliubov spectrum [Fig. 5.3(b)].

Through numerically fitting J_l versus V_0, its slope for the soft-core interaction becomes larger than that of the box interaction when increasing r_c [Fig. 5.3(c)]. On the other hand, momentum $\mathbf{k}_{\rm rot}$ corresponding to the onset of roton instabilities varies with r_c. From the numerical data, we found that $|\mathbf{k}_{\rm rot}| \approx 3\pi/2r_c$ when $r_c \gg d$ [Fig. 5.3(d)].

5.3 Kibble-Zurek mechanism

In 1976, Tom Kibble discovered that phase transition leads to disparate choices of broken local symmetry and as a result, topological defects are generated, also known as cosmic strings [154]. Later, Wojciech Zurek applied this theory to condensed mat-

ter physics and achieved success in describing the emergence of vortices in superfluid phase transition in liquid helium [155].

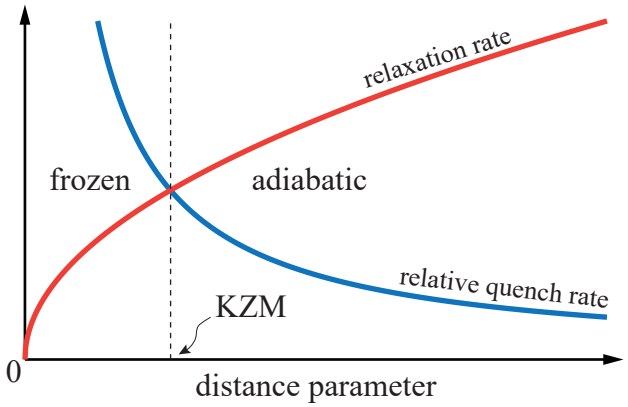


Figure 5.4: Kibble-Zurek Mechanism. The competition between the instantaneous relaxation rate and the relative quench rate determines the Kibble-Zurek time and separates the quench process to frozen and adiabatic stages.

The basic idea of KZM is illustrated in Fig. 5.4. For second-order thermal phase transition, one can quench the temperature T through the critical temperature T_c, and for quantum phase transition, one can instead change one parameter λ in the Hamiltonian through the critical value λ_c. In this work, for example, we choose $\lambda = J$. For convenience, we introduce a *distance* parameter $\varepsilon = 1 - \lambda/\lambda_c$, which tells the distance between λ to the phase transition point. On the one hand, Landau's mean-field theory unveils that the relaxation of the system in the vicinity of λ_c is infinitely slow, and the relaxation rate increases from 0 at $\varepsilon = 0$. On the other hand, we can find the relative quench rate, defined as $|\dot{\varepsilon}/\varepsilon|$, diverges at $\varepsilon = 0$, so there must be a cross point, $\hat{\varepsilon}$, between the two rates, and corresponds to the Kibble-Zurek time $\hat{t}$. Within the cross point, $|\varepsilon| < \hat{\varepsilon}$, the relaxation rate is lower than the quench, and the system is expected to be *frozen*. Beyond the cross point, $|\varepsilon| > \hat{\varepsilon}$, the relaxation is fast enough that the system should evolve *adiabatically* according to the manipulation of the parameter λ.

5.3.1 Novel power-law scalings

KZM not only separates the dynamics into two stages, and also provides several important scaling laws [133]. According to Landau's mean-field theory [20], there are two scaling laws for correlation length ξ and relaxation time τ for equilibrium states

$$\xi(\varepsilon) = \xi_0 |\varepsilon|^{-\nu}, \tag{5.11a}$$

$$\tau(\varepsilon) = \tau_0 |\varepsilon|^{-z\nu}, \tag{5.11b}$$

where ν and z are universal exponents only depend on the class of systems. KZM can be understood via a linear quench dynamics where ε is tuned from -1 to $+1$

$$\varepsilon(t) = \begin{cases} -1 & (t < -\tau_Q) \\ t/\tau_Q & (-\tau_Q \leqslant t \leqslant \tau_Q) \\ 1 & (t > \tau_Q) \end{cases}. \tag{5.12}$$

Meanwhile, $\lambda(t)$ changes from $2\lambda_c$ to 0, and order parameter changes from non-zero to zero. The system will pass the critic point at $t = 0$, and τ_Q^{-1} determines the quench rate, which can vary from adiabatic to impulse limit.

To estimate the KZM time $\hat{t}$ as shown in Fig. 5.4, we find the instantaneous relaxation time is $\tau(t) = \tau_0 |t/\tau_Q|^{-z\nu}$, and the relative quench rate is $|\dot{\varepsilon}/\varepsilon| = |t|^{-1}$. Without breaking generality, we consider $t > 0$ only. Then we shall expect that $\tau^{-1}(\hat{t}) = \hat{t}^{-1}$, and

$$\hat{t} = \left(\tau_0 \tau_Q^{z\nu}\right)^{\frac{1}{1+z\nu}} \propto \tau_Q^{1-\frac{1}{1+z\nu}}. \tag{5.13}$$

One can also check the evolution of an arbitrary physical variable $\alpha(t)$, whose instantaneous relaxation rate it $\tau^{-1}(t)$, such that

$$\begin{aligned} &\frac{\mathrm{d}\alpha(t)}{\mathrm{d}t} = -\frac{\alpha(t)}{\tau(t)} \\ \Rightarrow \quad &\alpha(t) = \alpha_0 \exp\left[-\frac{\tau_Q}{(1+z\nu)\tau_0}\left(\frac{t}{\tau_Q}\right)^{1+z\nu}\right] \end{aligned} \tag{5.14}$$

If we write $\alpha(t)$ in the form of $\sim \exp\left[-(t/\hat{t})^{1+z\nu}\right]$, we can also find that $\hat{t} \propto \tau_Q^{1-\frac{1}{1+z\nu}}$. Similarly, the correlation length at time $\hat{t}$ is

$$\hat{\xi} = \xi(\hat{t}) = \xi_0 \left(\frac{\tau_Q}{\tau_0}\right)^{\frac{\nu}{1+z\nu}} \propto \tau_Q^{\frac{\nu}{1+z\nu}}. \tag{5.15}$$

Another important scaling is applied to the vortex nucleation, or topological defects. The density of vortices, n_v, can be phenomenologically estimated by $\hat{\xi}^{\mathsf{def}-\mathsf{dim}}$, such that

$$n_v = \hat{\xi}^{\mathsf{def}-\mathsf{dim}} \propto \tau_Q^{(\mathsf{def}-\mathsf{dim})\frac{\nu}{1-z\nu}}, \tag{5.16}$$

where def is the dimension of the topological defects, e.g., $\mathsf{def} = 0$ for vortices in 2D space. dim is the dimension of the system.

This method can also be extended to the phase transition beyond mean-field theory. For example, we consider Kosterliz-Thouless phase transition class [156], where the correlation length and instantaneous relaxation time follow the power-law relations

$$\xi(\varepsilon) = \xi_0 \exp\left[a/\sqrt{\varepsilon}\right], \tag{5.17a}$$

$$\tau(\varepsilon) = \tau_0 \exp\left[za/\sqrt{\varepsilon}\right]. \tag{5.17b}$$

The solution of KZM time $\hat{t}$ is given by $\tau(\hat{\varepsilon}) = \hat{t}$ and yields [133]

$$\hat{t} = \tau_Q \left(\frac{za/2}{W\left[za/2\sqrt{\tau_Q/\tau_0}\right]} \right)^2, \tag{5.18}$$

where $W[x]$ is Lambert W function. The asymptotic behaviour is

$$\hat{t} \approx \begin{cases} \tau_0 & , \quad \tau_Q \ll \tau_0 \\ \left(\frac{za}{2}\right)^2 \frac{\tau_Q}{\ln \tau_Q/\tau_0 - \ln\ln \tau_Q/\tau_0} & , \quad \tau_Q \gg \tau_0 \end{cases} \tag{5.19}$$

5.3.2 Dynamics of superfluid fraction and density variance

The studies of quenched BHM have already shown the KZM in the MI-SF transition [134]. With Rydberg-dressing, the first question we need to answer is whether the dynamics are different from the BHM. Therefore, we show the evolution of the SF fraction ρ_s and density variance σ_n as plotted in Fig. 5.5. We let the quench rate $a_Q = 10^{-2}U$, the interaction is box-type with $r_c = d,\ 2d,\ 3d$. The interaction strength is $V_0 = 0.1U$ for Fig. 5.5(a,b) and $V_0 = 0.5U$ for Fig. 5.5(c,d).

As shown in Fig. 5.5(a,b), when the interaction strength is weak, the dynamics is very similar to that of BHM. The LRI behaves as a weak perturbation. The lower panels of Fig. 5.5(a,b) show the difference between $V_0 \neq 0$ and $V_0 = 0$, where the change of both ρ_s and σ_n is one order smaller than the upper panel. Both ρ_s and σ_n increase from 0 as $J(t)$ ramps up. The tunnelling is negligible until $J(t)$ increases to $\sim 0.17U$. This forms the early stage of evolution. After $J(t) > 0.17U$, ρ_s and σ_n increase rapidly.

Dynamics change drastically with strong LRI, as illustrated in Fig. 5.5(c,d). At the early stage, $\rho_s(t)$ is the same as BHM and universal for different LRI lengths. However, ρ_s decrease with increasing r_c at later times. σ_n is more sensitive to r_c. Different curves depart from each other when $J(t) > 0.17U$. From a mean-field level, we can understand these curves by noting that the density-density interaction at a given site becomes stronger due to the LRI (i.e., with multiple sites). Eventually, the local SF order parameter is reduced with larger soft-core radius [Fig. 5.5(c)]. At the same time, the density variance is enhanced [Fig. 5.5(d)], as density waves are excited during the quench.

KZM time is a turning point where the system leaves the frozen regime, so we use the time where $\mathrm{d}^2\rho_s/\mathrm{d}t^2$ is maximised, pointed out with black arrows as shown in Fig. 5.5 for $J \approx 0.17U$. At this stage, the LRI has little influence on the emergence of SF order and ρ_s, so we conclude the KZM is universal in our system for various LRI based on our initial state.

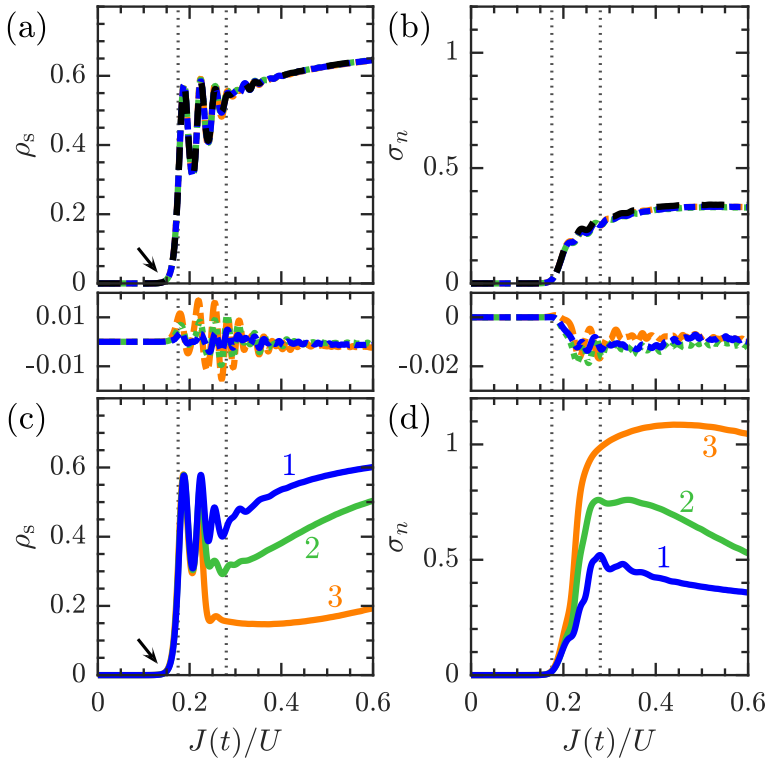


Figure 5.5: Dynamics of the superfluid fraction ρ_s and density variance σ_n. (a,b), Weak interacting case with $V_0 = 0$ (dashed black) and $V_0 = 0.1U$ (colored). The lower panel shows the difference between ρ_s and σ_n between interacting and non-interacting cases. (c,d) In strong interacting cases with $V_0 = 0.5U$, the evolution depends on the strength and length of the LRI. In the simulation, $a_Q = 10^{-2}U$ and $r_c = d(blue), 2d(green), 3d(orange)$. Arrows indicate the Kibble-Zurek time. Dotted lines indicate probe times for time-of-flight (TOF) interference. The first line $J(t) = 0.175U$ is for Fig. 5.9 and the second $J(t) = 0.28U$ is for Fig. 5.10.

5.3.3 Vortex nucleation and Kibble-Zurek scaling

We now turn to the dynamics of the vortex nucleation. When $J(t)$ is increasing, topological defects (vortices) can be created in the many-body system. Using the GWF, in a 2D square lattice, n_v is evaluated according to

$$n_v = \frac{1}{2\pi M}\sum_i \left|\arg(\phi^*_{i+\hat{x}}\phi_i) + \arg(\phi^*_{i+\hat{x}+\hat{y}}\phi_{i+\hat{x}}) + \arg(\phi^*_{i+\hat{y}}\phi_{i+\hat{x}+\hat{y}}) + \arg(\phi^*_i\phi_{i+\hat{y}})\right|, \tag{5.20}$$

The development of the topological defects in the vicinity of the phase transition point is related to various quantities, such as the healing length and the density variance, which has been studies in BHM [132] and eBHM with dipolar interactions [120, 157].

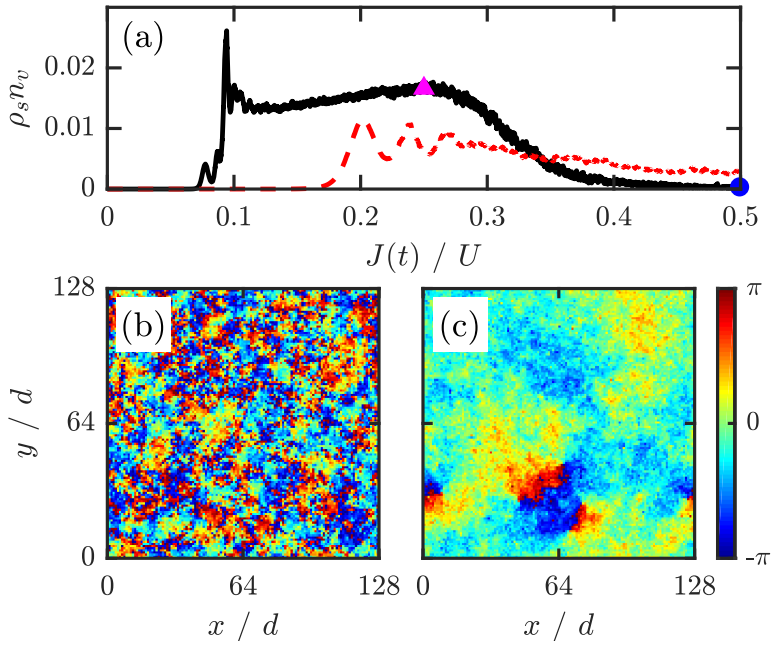


Figure 5.6: Demonstration of the vortex nucleation. The LRI is set to be box-type with $V_0 = 0.5U$, $r_c = d$. (a) Evolution of superfluid vortex density with quench rate a_Q/U is 10^{-3} (black), 10^{-2} (red). (b,c) The snapshots of local phase of SF order parameter at the points labelled as magenta triangle and blue circle in (a), and specifically (b) $J(t)/U = 0.25$, (c) $J(t)/U = 0.5$

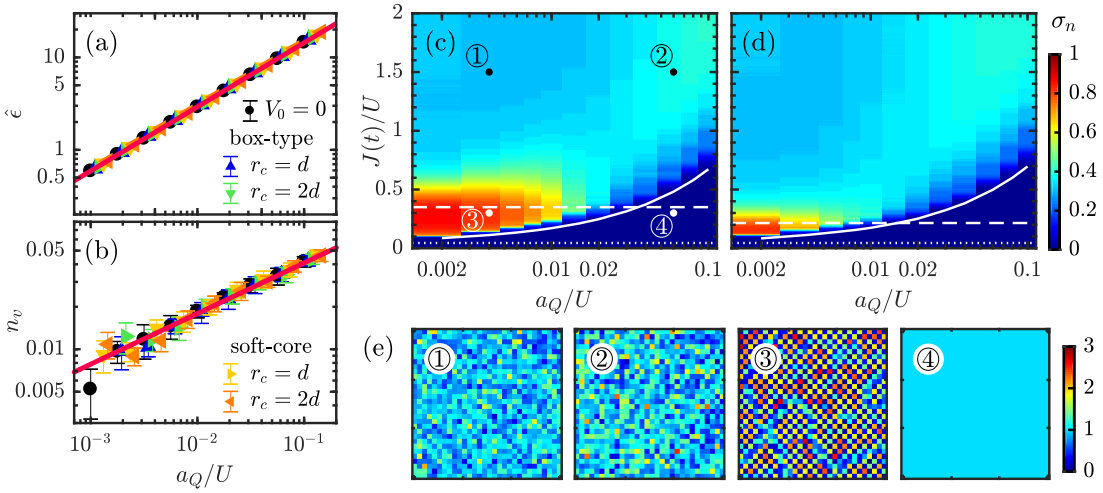


Figure 5.7: (a) Distance parameter and (b) density of vortices at KZ time. The density variance evolution under different quench rate for (c) box-type and (d) soft-core interaction with $r_c = d$, $V_0 = 0.6U$. (e) Snapshots of density distribution as labelled in (c).

In our system, we demonstrate the evolution of vortex density in Fig. 5.6(a). We let the LRI to be box-type and $V_0 = 0.5U$, $r_c = d$. Since the local phase of SF order parameters, ϕ, have random values, we plotted the multiplication of SF density and the vortex density, $\rho_s n_v$. The quench rate a_Q is set to be $10^{-2}U$ and $10^{-3}U$ for comparison. For intermediate quench rate $a_Q = 10^{-2}U$, $\rho_s n_v$ increases rapidly around $J(t) = 0.17U$.

In this case, there will be some vortices remained even when $J(t)$ is deeply in the SF phase region. When the quench rate is low, $a_Q = 10^{-3}U$, $\rho_s n_v$ increases quickly when $J(t) > 0.071U$. This comes from the fact that low-energy modes are excited during the slow quench, which creates many vortices. Subsequently, the SF vortex density decreases with increasing $J(t)$. When $J(t)$ is large, vortex-antivortex pairs recombine at a higher rate, which speeds up the relaxation of the system to a homogeneous SF with nearly homogeneous phases [Fig. 5.6(c)].

To find the universal behaviours in ρ_s, we change the quench rate from 10^{-3} to 10^{-1}, and find the KZM time for non-interacting, box and soft-core interactions with $V_0 = 0.6U$, $r_c = d$, and $2d$, respectively. The corresponding frozen parameter $\hat{\varepsilon}$ is shown in Fig. 5.7(a). Apparently, $\hat{t}$ and $\hat{\varepsilon}$ are independent to the interaction types. $\hat{\varepsilon}$ is fitted by

$$\hat{\varepsilon} = \left(\frac{a_Q \tau_0}{J_s/U}\right)^{\frac{1}{1+z\nu}}. \tag{5.21}$$

The fitting parameters yield $J_s = 0.0449U$, $z\nu = 0.442$ and $U\tau_0 = 21.0$. The resulting J_s is close to the ground-state phase transition point for MI-SF. According to the decoupling approach, $J_s = 0.0429U$ [158] and our calculation $J_s = 0.0415U$ (Fig. 5.2). The vortex density $n_v \propto \xi^{\mathsf{def}}/\xi^{\mathsf{dim}} \propto a_Q^{(\mathsf{dim}-\mathsf{def})\nu/(1+z\nu)}$, where ξ is the correlation length, and $\mathsf{dim} = 2$ is the dimension of the lattice, def is that of topological defects. Here we argue that $\mathsf{def} = 1$ because the vortices are always created in pairs (e.g., Fig. 5.6c). Using the same interaction configuration as aforementioned, the scaling exponent $(\mathsf{dim}-\mathsf{def})\nu/(1+z\nu) = 0.359$, as shown in Fig. 5.7(b). Compared to the fitting results of $\hat{\varepsilon}$, we obtain $\nu = 0.518$, $z = 0.854$, Here we make a comparison with the mean-field results where $\nu = 0.5$, $z = 2$, and 3D XY model, which is frequently compared with 2D BHM, where $\nu = 2/3$ and $z = 1$ [37, 159, 160]. In Ref. [134], it was found that the vortex density has anomalous behaviours in the slow quench regime ($a_Q < 10^{-2}U$). In our simulations, n_v shows larger fluctuation as a_Q decreases due to the finite size effect, but the average values still fit well with the universal scaling.

The dynamics of σ_n for box-type [Fig.5.7(c)] and soft-core [Fig.5.7(d)] are qualitatively the same. We compared the values of MI-SF transition point of BHM J_s, the critical point for roton instability J_l, and the hopping parameter at KZM time $J(\hat{t})$. Only the last one is related to a_Q. The breakdown of the universal dynamics is more outstanding for the slow quenches, where $J(\hat{t}) < J_l$. For fast quenches when $J(\hat{t}) > J_l$, however, the system will not fully respond to the roton mode, where dynamics is still universal. σ_n develops a maximal value around $J(t) \sim J_l$ when the quench rate is low. In this region, the system suffers significantly from the roton instability, exhibiting apparent density patterns [Fig. 5.7(e3)]. When $J(\hat{t}) > J_l$, the density variance σ_n increases slowly with time.

5.4 Correlations in the quench process

The correlation functions characterise various features of many-body systems. Here, I present a summary of the relations between the correlation functions and the time-of-flight interference (TOF). The former can be derived from theoretical models and signifies the novel quantum many-body phases. The latter is one of the essential experimental techniques in cold atom systems.

TOF is an analogue to light interference for the matter waves of atoms. The realisation of interference is based on the atoms being prepared in a degenerate state, or specifically, a condensed phase. For BEC on an optical lattice, the TOF can also be analogised with the grating diffraction. Furthermore, similar to optics, the fringes of the interference pattern are associated with the first-order correlation, and unveils the density of atoms in their momentum space. The second-order correlation has more in-depth insight, which can be implemented as the Hanbury Brown and Twiss (HBT) effect. As of TOF, it reflects the density modulations, or density wave, embedded in the optical lattice. The combination of the two correlation functions makes it possible to probe the instantaneous phase of the system dynamically during the quench.

5.4.1 Correlation measurement and time-of-flight interference

Generally, the l-th order correlation function $G^{(l)}$ is defined as the expectation of the field operators in their normal order

$$G^{(l)}(\mathbf{x}_1,\mathbf{x}_2,\cdots,\mathbf{x}_l)=\langle\hat{a}^\dagger(\mathbf{x}_1)\hat{a}^\dagger(\mathbf{x}_2)\cdots\hat{a}^\dagger(\mathbf{x}_l)\hat{a}(\mathbf{x}_l)\cdots\hat{a}(\mathbf{x}_2)\hat{a}(\mathbf{x}_1)\rangle_e, \tag{5.22}$$

where $\langle..\rangle_e=\sum_i P_i\langle i|..|i\rangle$ is the ensemble average. For pure state, it is equal to the quantum expectation value. Another widely used definition is by its normalisation

$$g^{(l)}(\mathbf{x}_1,\mathbf{x}_2,\cdots,\mathbf{x}_l)=\frac{G^{(l)}(\mathbf{x}_1,\mathbf{x}_2,\cdots,\mathbf{x}_l)}{\langle\hat{n}(\mathbf{x}_1)\rangle_e\langle\hat{n}(\mathbf{x}_2)\rangle_e\cdots\langle\hat{n}(\mathbf{x}_l)\rangle_e}. \tag{5.23}$$

Furthermore, it is also important to consider the covariance $C(\mathbf{x}_1,\mathbf{x}_2)$, which is based on the number operators $\hat{n}=\hat{a}^\dagger\hat{a}$, and reads

$$C(\mathbf{x}_1,\mathbf{x}_2)=\langle\hat{n}(\mathbf{x}_1)\hat{n}(\mathbf{x}_2)\rangle_e-\langle\hat{n}(\mathbf{x}_1)\rangle_e\langle\hat{n}(\mathbf{x}_2)\rangle_e. \tag{5.24}$$

In experiment, $C(\mathbf{x}_1,\mathbf{x}_2)$ can be measured by coincidence counting and plays a similar role to the second-order correlation $G^{(2)}(\mathbf{x}_1,\mathbf{x}_2)$ [161].

In this work, under Gutzwiller ansatz, the original field operators are decoupled, and the wave function is factorisable, such as $\langle\hat{b}_1^\dagger\hat{b}_2\rangle=\langle\hat{b}_1^\dagger\rangle\langle\hat{b}_2\rangle=\phi_1^*\phi_2$, where $\hat{b}_i^\dagger$ is the operator creating particles in the i-th lattice point. This results in the covariance always being zero and the correlation functions being trivial. TOF, however, can lead to

another set of field operators $\hat{a}(\mathbf{x})$ as a superposition of $\hat{b}_i$, whose covariance or high-order correlations can be calculated theoretically. Following this idea, we will show the construction of $\hat{a}(\mathbf{x})$ by a linear combination of $\hat{b}_i$ in the ballistic expansion approximation, and successively the first and second-order correlation functions and covariance are derived.

Ballistic Expansion

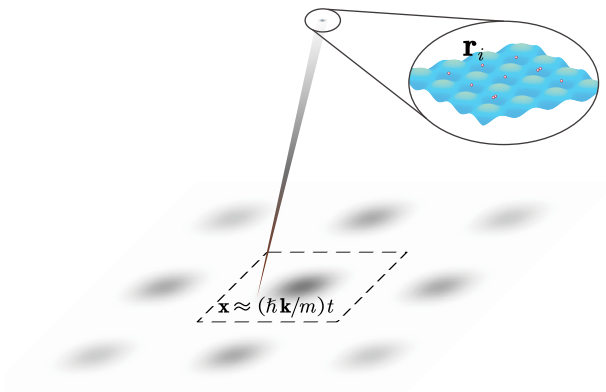


Figure 5.8: Schematic diagram of the time-of-flight expansion. The atoms are released from the lattice and interfere. The image of real space (labelled by $\mathbf{x}$) reflects the distribution in the reciprocal space of the lattice. The dashed box illustrates the first Brillouin zone.

Presuming the optical lattice is described by Wannier operators $\hat{b}_i$ at time $t = 0$, the field operator reads $\hat{\psi}(\mathbf{r}) = \sum_i w(\mathbf{r} - \mathbf{r}_i)\hat{b}_i$. When the external fields, including trapping and cooling, are removed, the atoms will be released and *fly*, and the corresponding operator evolves according to

$$\hat{a}(\mathbf{x}) = \int \mathrm{d}^3\mathbf{r} \exp\left[\mathrm{i}\frac{m}{\hbar}\frac{\mathbf{x}-\mathbf{r}}{t}\cdot(\mathbf{x}-\mathbf{r})\right]\hat{\psi}(\mathbf{r}) = \int \mathrm{d}^3\mathbf{r} \exp\left[\mathrm{i}\frac{m|\mathbf{x}-\mathbf{r}|^2}{\hbar t}\right]\sum_i w(\mathbf{r}-\mathbf{r}_i)\hat{a}_i. \tag{5.25}$$

Here the phase factor is applied by Wentzel–Kramers–Brillouin (WKB) approximation. We have to bear in mind that the beginning of the expansion is nonlinear to time, and the *ballistic* momentum $m\mathbf{x}/t$ is an approximation. Then we apply the Fourier transformation to the Wannier function, which results in

$$\int \mathrm{d}^3\mathbf{r} \exp\left[\mathrm{i}\frac{m|\mathbf{x}-\mathbf{r}|^2}{\hbar t}\right] w(\mathbf{r}-\mathbf{r}_i) = \int \mathrm{d}^3\mathbf{r} \exp\left[\mathrm{i}\frac{m|\mathbf{x}-\mathbf{r}|^2}{\hbar t}\right] \int \frac{\mathrm{d}^3\mathbf{k}}{(2\pi)^3} e^{\mathrm{i}\mathbf{k}\cdot(\mathbf{r}-\mathbf{r}_i)}\tilde{w}(\mathbf{k})$$
$$\sim e^{-\mathrm{i}\mathbf{k}\cdot\mathbf{r}_i}\tilde{w}(\mathbf{k}), \tag{5.26}$$

where

$$\mathbf{k} = \frac{m\mathbf{x}}{\hbar t}, \tag{5.27}$$

and one can absorb the constant produced by Gaussian integral into $\tilde{w}(\mathbf{k})$. Finally, we have

$$\hat{a}(\mathbf{x}) = \tilde{w}(\mathbf{k}) \sum_i e^{-i\mathbf{k}\cdot\mathbf{r}_i} \hat{b}_i, \tag{5.28}$$

and

$$\hat{n}(\mathbf{x}) = |\tilde{w}(\mathbf{k})|^2 \sum_{i,j} e^{i\mathbf{k}\cdot(\mathbf{r}_i - \mathbf{r}_j)} \hat{b}_i^\dagger \hat{b}_j. \tag{5.29}$$

As discussed in Sec. 2.3, the Wannier function is localised in real space as the lattice is deep. Thereby, its Fourier transform is delocalised and has a flat profile in the momentum space. One can crudely approximate $\tilde{w}(\mathbf{k}) \approx$ const. and simplify the following calculation. In experiment, the Wannier envelope can be seen as large as 2 to 3 Brillouin zones [162, 163].

5.4.2 First-order correlation

The snapshot of TOF is equivalent to measure the quantum expectation values of the density operator, such that

$$W^{(1)}(\mathbf{x}) = \langle \hat{n}(\mathbf{x}) \rangle. \tag{5.30}$$

This is the first-order correlation, which can be obtained by substituting Eq. (5.29). Then

$$\langle \hat{n}(\mathbf{x}) \rangle = |\tilde{w}(\mathbf{k})|^2 \sum_{i,j} e^{i\mathbf{k}\cdot(\mathbf{r}_i - \mathbf{r}_j)} \langle \hat{b}_i^\dagger \hat{b}_j \rangle. \tag{5.31}$$

The field operators can be decoupled, which ends up with

$$\langle \hat{b}_i^\dagger \hat{b}_j \rangle = \phi_i^* \phi_j (1 - \delta_{ij}) + n_i \delta_{ij}, \tag{5.32}$$

and finally

$$n(\mathbf{x}) = M |\tilde{w}(\mathbf{k})|^2 \left[|S(\phi;\mathbf{k})|^2 + \frac{1}{M} \sum_i \left(n_i - |\phi_i|^2 \right) \right], \tag{5.33}$$

where $S(\phi;\mathbf{k}) \overset{!}{=} 1/\sqrt{M} \sum_i e^{i\mathbf{k}\cdot\mathbf{r}_i} \phi_i$ is the Fourier transformation of ϕ, M is the total number of sites. The relationship between $\mathbf{x}$ and $\mathbf{k}$ is based on the ballistic approximation, $\mathbf{x} = (\hbar t/m)\mathbf{k}$. We notice that the profile of $n(\mathbf{k})$ is the same as $|S(\phi;\mathbf{k})|^2$, except for a constant term which guarantees the conservation of the number of particles. If ϕ_i is homogeneous and non-zero, one can expect $n(\mathbf{k})$ become a δ-function with a peak at $\mathbf{k} = 0$, which indicates that the initial state is a superfluid. If there is a modulation of ϕ_i in the lattice space, one can also expect some other peaks in $n(\mathbf{k})$. As will be shown later, the second-order correlation better describes these features.

Regarding that our initial state is Mott-insulator, one needs to do multiple trajectories to show the effects of the initial random phase and get rid of the symmetry breaking caused by the formation of domain walls. However, as the size of the lattice grows,

the randomness can also be retrieved in the sense of thermal limit. This results in a trade-off between the size of the lattice and the number of trajectories. In this work, we use $\gtrsim 100 \times 100$ lattice points and ~ 10 trajectories for simulation.

5.4.3 Second-order correlation

Inheriting from the first-order correlation, we can extend the same procedure to the second-order correlation. This can be implemented by two-point coincidence measurement of TOF imaging. Let the separation of the two points be $\mathbf{u}$, corresponding to the momentum difference $\mathbf{q}$, and we have the scattering amplitude $\sim \langle \hat{a}(\mathbf{x}+\mathbf{u})\hat{a}(\mathbf{x})\rangle$, resulting in the two-point joint intensity

$$W^{(2)}(\mathbf{x},\mathbf{x}+\mathbf{u}) = \langle \hat{a}^\dagger(\mathbf{x})\hat{a}^\dagger(\mathbf{x}+\mathbf{d})\hat{a}(\mathbf{x}+\mathbf{d})\hat{a}(\mathbf{x})\rangle, \tag{5.34}$$

It is straightforward to work out the covariance:

$$\begin{aligned}
C(\mathbf{k},\mathbf{k}+\mathbf{q}) &= \langle \hat{a}^\dagger(\mathbf{x})\hat{a}(\mathbf{x})\hat{a}^\dagger(\mathbf{x}+\mathbf{u})\hat{a}(\mathbf{x}+\mathbf{u})\rangle - \langle \hat{a}^\dagger(\mathbf{x})\hat{a}(\mathbf{x})\rangle\langle \hat{a}^\dagger(\mathbf{x}+\mathbf{u})\hat{a}(\mathbf{x}+\mathbf{u})\rangle \\
&= |\tilde{w}(\mathbf{k})|^2\,|\tilde{w}(\mathbf{k}+\mathbf{q})|^2 \left[\sum_{i,j,m,n} e^{\mathrm{i}\mathbf{k}\cdot(\mathbf{r}_i-\mathbf{r}_j)+\mathrm{i}(\mathbf{k}+\mathbf{q})\cdot(\mathbf{r}_m-\mathbf{r}_n)} \langle \hat{b}_i^\dagger \hat{b}_j \hat{b}_m^\dagger \hat{b}_n\rangle \right. \\
&\qquad \left. - \left(\sum_{i,j} e^{\mathrm{i}\mathbf{k}\cdot(\mathbf{r}_i-\mathbf{r}_j)} \langle \hat{b}_i^\dagger \hat{b}_j\rangle \right) \left(\sum_{i,j} e^{\mathrm{i}(\mathbf{k}+\mathbf{q})\cdot(\mathbf{r}_i-\mathbf{r}_j)} \langle \hat{b}_i^\dagger \hat{b}_j\rangle \right) \right] \\
&= |\tilde{w}(\mathbf{k})|^2\,|\tilde{w}(\mathbf{k}+\mathbf{q})|^2 \Big\{ \left|S(n-|\phi|^2;\mathbf{q})\right|^2 + \left|S(\eta^*-\phi^{*2};\mathbf{Q})\right|^2 + C_0 \\
&\quad + \Delta(\mathbf{q})S(n-|\phi|^2;\mathbf{q}) - 4\mathscr{X}(\phi^*;(n-|\phi|^2)\phi) + 2\mathscr{X}(\phi^*;\gamma-\eta\phi^*) \\
&\quad + \sqrt{M}\Delta(\mathbf{q})S(\phi^*;\mathbf{k})\tilde{S}(\phi;\mathbf{k}') + 2\sqrt{M}\big[\mathscr{Y}(\phi,\phi,\eta^*-\phi^{*2};\mathbf{k},\mathbf{k}') \\
&\quad + \mathscr{Y}(n-|\phi|^2,\phi,\phi^*;\mathbf{q},\mathbf{k})\big]\Big\},
\end{aligned} \tag{5.35}$$

where

$$\eta_i = \langle \hat{b}_i\hat{b}_i\rangle, \quad \gamma_i = \langle \hat{b}_i^\dagger \hat{b}_i\hat{b}_i\rangle, \quad \lambda_i = \langle \hat{b}_i^\dagger \hat{b}_i^\dagger \hat{b}_i\hat{b}_i\rangle,$$

$$\Delta(\mathbf{q}) = \frac{1}{\sqrt{M}}\sum_i e^{\mathrm{i}\mathbf{q}\cdot\mathbf{r}_i}, \quad \mathscr{X}(f,g) = \mathrm{Re}\left[S(f;\mathbf{k})\tilde{S}(g;\mathbf{k}) + S(f;\mathbf{k}')\tilde{S}(g;\mathbf{k}')\right],$$

$$\mathscr{Y}(f,g,h;\mathbf{k}_1,\mathbf{k}_2) = \mathrm{Re}\left[S(f;\mathbf{k}_1)S(g;\mathbf{k}_2)\tilde{S}(h;\mathbf{k}_1+\mathbf{k}_2)\right],$$

$$C_0 = \frac{1}{M}\sum_i \left(8n_i|\phi_i|^2 - 2n_i^2 - |\eta_i|^2 + \lambda_i - 6|\phi_i|^4 - 4\mathrm{Re}\left[\gamma_i^*\phi_i - \eta_i^*\phi_i^2\right]\right),$$

and $\mathbf{Q} = 2\mathbf{k}+\mathbf{q}$. We notice that the Wannier envelope of the two points, $\mathbf{k}$ and $\mathbf{k}+\mathbf{q}$, can be picked out. As of deep lattice, we assume $\tilde{w}(\mathbf{k}) = \text{const.}$ as mentioned before. One can also define a covariance as a function of a single argument, $\mathbf{q}$, by integrating $\mathbf{k}$, such that $C(\mathbf{q}) = \int C(\mathbf{k},\mathbf{k}+\mathbf{q})\mathrm{d}^2\mathbf{k}$.

In Mott insulator regime, $\phi = \eta = \gamma = 0$. The covariance is reduced to

$$C_{\text{ins.}}(\mathbf{q}) \approx N|S(n;\mathbf{q})|^2 + N\Delta(\mathbf{q})S(n;\mathbf{q}) + \sum_i \left(\langle \hat{n}_i \hat{n}_i \rangle - n_i - 2n_i^2\right). \tag{5.36}$$

The first term indicates that the profile of $C(\mathbf{k},\mathbf{k}+\mathbf{q})$ mainly depends on the Fourier transform of the density in lattice space. The second term is a sharp peak at the centre of Brillouin zone $\mathbf{q} = 0$. The last term is a constant shift. Therefore, the density modulation, also known as the structure factor shown in Eq. (5.7), $S(n,\mathbf{q})$, is well depicted by the covariance.

5.4.4 Emergence of the density wave and supersolidity

Based on TOF interference, we make a comparison between the early and late stages of dynamical evolution. As shown in Fig. 5.5, we took the snapshots at $Ut = 17.5$ and 28 with $a_Q = 10^{-2}U$, which are plotted in Fig. 5.9 and Fig. 5.10, respectively. The former is within the universal regime where the system just leaves MI into SF, and the latter represents for the state where the system leaves the oscillatory regime and begins to relax. In Fig. 5.9, we plotted the cases without LRI and with box-type interaction $V_0 = 0.66U$, $r_c = d$. Since the early stage is insensitive to the LRI, the difference between those two cases is not obvious. In Fig. 5.10, we show the cases without LRI and box-type interaction with various interaction length $r_c = d, 2d, 3d, 4d$. The interaction strengths are $V_0 = 0.66U, 0.50U, 0.36U, 0.24U$, respectively.

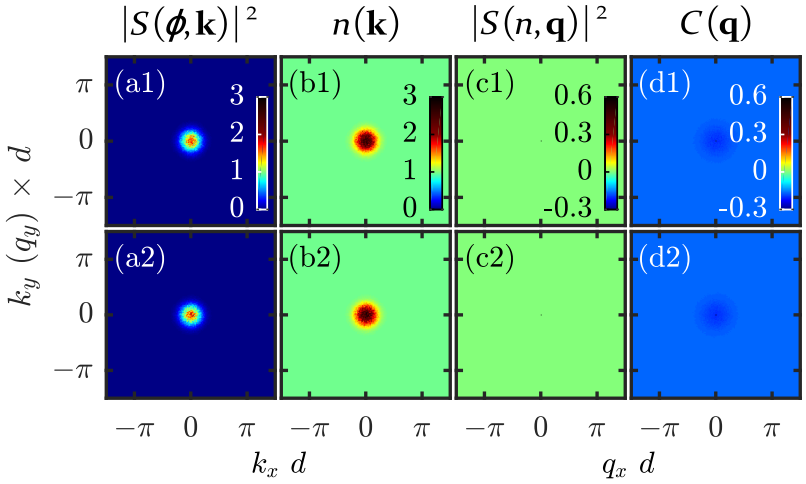


Figure 5.9: TOF snapshots at time $Ut = 17.5$, $a_Q = 10^{-2}U$, for TOF density $n(\mathbf{k})$ and covariance $C(\mathbf{q})$, as well as the Fourier transform of order parameter $|S(\phi,\mathbf{k})|^2$ and density $|S(n,\mathbf{q})|^2$. (a1-d1) The results without LRI, (a2-d2) for box-type LRI with interaction length $r_c = d$, strength $V_0 = 0.66U$.

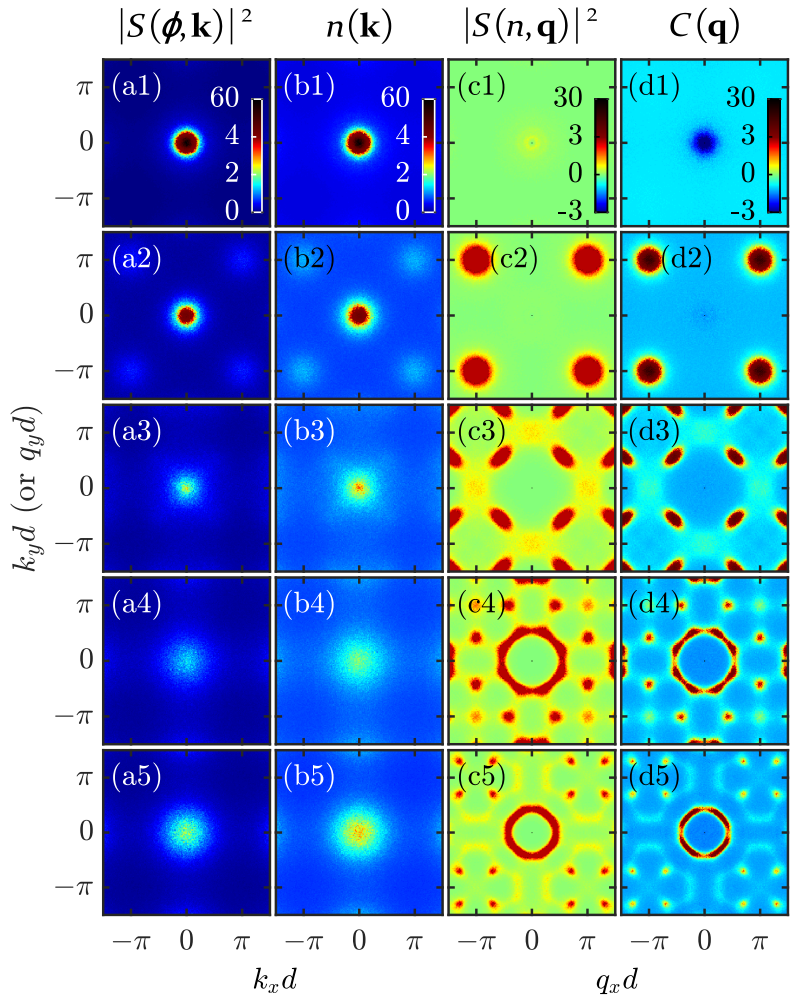


Figure 5.10: TOF snapshots at time $Ut = 28$, $a_Q = 10^{-2}U$, for TOF density $n(\mathbf{k})$ and covariance $C(\mathbf{q})$, as well as the Fourier transform of order parameter $|S(\phi,\mathbf{k})|^2$ and density $|S(n,\mathbf{q})|^2$. (a1-d1) The results without LRI, (a2-d5) for box-type LRI with interaction lengths being $r_c = d, 2d, 3d, 4d$, strengths $V_0 = 0.66U, 0.50U, 0.36U, 0.24U$, respectively.

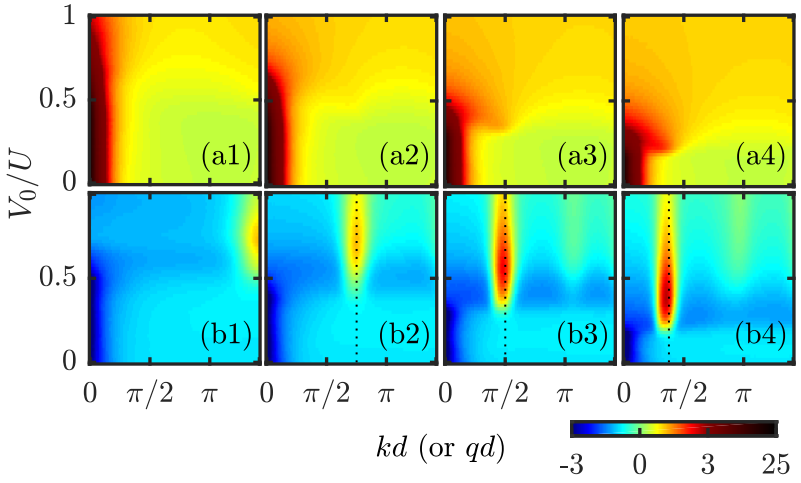


Figure 5.11: Ring integrals of (a1-a4) $n(k)$ and (b1-b4) $C(q)$ at $Ut = 28$ and $a_Q = 10^{-2}U$. The LRI is box-type and $r_c =$ (a1,b1) d, (a2,b2) $2d$, (a3,b3) $3d$, (a4,b4) $4d$.

At the early stage, $Ut = 17.5$, $|S(\phi,\mathbf{k})|^2$ and $n(\mathbf{k})$ are almost uniform except for a small peak area centred at $\mathbf{k} = 0$. Such a feature is hardly visible in the distribution of $|S(n,\mathbf{q})|^2$ and $C(\mathbf{q})$. Note that all these distributions are flat in the initial state. At a later time, $Ut = 28$, $n(\mathbf{k})$ has a higher peak around $\mathbf{k} = 0$, about 20 times larger than that at $Ut = 17.5$, signifying the appearance of the SF fraction. Comparing different LRI, we find that the SF fraction decreases as r_c grows. The most important feature happens to the covariance $C(\mathbf{q})$, which has multiple peaks as LRI exists. The profile of $S(n,\mathbf{q})$ and $C(\mathbf{q})$ are very similar, except for a constant bias. We can also find some weak peaks in $n(\mathbf{k})$ and $S(\phi,\mathbf{k})$ which are at the same position. For the sake of high contrast in the experiments, $C(\mathbf{q})$ is a better choice than $n(\mathbf{k})$. The structure factor appears to have peaks at $\pi/d(\pm1,\pm1)$ for box-type interaction with $r_c = d$ [Fig. 5.10(c2-d2)], which refers to a chequerboard density distribution, and is consistent with the ground state of eBHM with nearest-neighbour interactions [40]. When $r_c > d$, however, the featuring peaks become more complicated. The smallest momentum $|\mathbf{q}|$ of the peaks also decreases as r_c increases. This suggests that the periodicity in real lattice space is growing with r_c. We have also noticed the second-order peaks for $r_c = 3d$ and $4d$ [Fig. 5.10(c4-d4, c5-d5)]. They correspond to the multiple periodic density modulations appear in SS phase, and the density in real space goes far beyond the chequerboard assumption.

To further present the effects of LRI to the TOF results, we calculate the *ring* integrals of $n(\mathbf{k})$ and $C(\mathbf{q})$, which, for $n(\mathbf{k})$ as an example, are defined as $n(k) \stackrel{!}{=} \int n(\mathbf{k}')\delta\left(k - |\mathbf{k}'|\right)\mathrm{d}\mathbf{k}'$. We show $n(k)$ and $C(q)$ at $Ut = 28$ for box-type LRI with $r_c = d$, $2d$, $3d$, $4d$ and V_0 varying from 0 to 1 in Fig. 5.11.

We find that when the V_0 is small, both $n(k)$ and $C(q)$ change slightly. When V_0 increases to a certain value, which is smaller as r_c increases, the distribution of $n(k)$ is broadened, and $C(q)$ also begins to have peaks at $q \neq 0$. This corresponds to the transition to SS phase. As for $r_c = d$ [Fig. 5.11(a1,b1)], the peak of $C(q)$ appears at $k = \sqrt{2}\pi/r_c$, and its position for $r_c > d$ is consistent with the position of roton minima as predicted in Fig. 5.3(d), $k_{\mathrm{rot}} \approx 3\pi/(2r_c)$. When V_0 keeps growing, the peak values of $n(k)$ at $k = 0$ decrease. We can expect that the strong LRI will suppress the SF order parameter and even lead to the insulating phase.

Chapter 6

Project: Trapping Atoms with 3D Printing Technology

In this chapter, I will give a summary of our earlier work on the 3D atom chip project [3]. A major topic in the community of cold atom physics is to transfer the experiments from the laboratory to industrial use and create commercial values. The cold atom system have excellent properties, such as high sensitivity and controllability, which unveil great potential for next-generation devices superior to conventional ones, e.g., semiconductor materials. However, a compact and reliable facility to acquire the cold atom resource remains a challenge and requires a systematic redesign.

From the perspective of physics, trapping and controlling atoms always require electromagnetic fields including lasers, radio frequency (rf) waves, static fields. For static magnetic fields, as an example, its strengths decay quickly in vacuum and usually results in the demand for huge coils and high energy consumptions in experiment. As for laboratory demonstrations, massive coils are acceptable for convenient installation. A practicable device, however, expects those heavy parts to be more integrated and delicate. Therefore, the concept of *atom chip* has been put forward and gained great success [164].

Conventional atom chips are designed on printed circuit board (PCB) where current-carrying wires generate magnetic fields. There are two major disadvantages. First, the geometry of the wires is restricted to a 2D surface, which wastes a lot of space in the vacuum chamber and reduces the efficiency of the utility of electricity. Second, the material and manufacture of PCB restrict the maximal current density, which limits the lifespan of the device. To overcome these drawbacks, we tried to extrude the designs of the wires from a 2D surface to a 3D space. This can be realised by the new rising technology of additive manufacture by 3D printing.

In the chapter, we will first introduce the physical background of the magneto-optical trap (MOT) in Sec. 6.1, which is a basic technique to trapping neutral atoms. Next, we will show three different designs of 3D printed MOT in Sec. 6.2. The generated magnetic fields and electrical currents are simulated by COMSOL Multiphysics. Afterwards,

we will show the time response performance of the 3D MOTs in Sec. 6.3. Lastly, we will quote some experimental results carried out by our collaborators in Sec. 6.4 [4].

6.1 Magneto-optical trap

MOT is one of the most conventional approaches to getting a large number ($10^7 \sim 10^{10}$) of cold ($\sim \mu$K) atoms. The trapping and cooling processes are featured by the restoration of atoms towards the trapping centre via the state-selective forces between light and atoms. The precise control of the restoring force can be significantly promoted by applying an appropriate magnetic field and monochromatic laser with very narrow linewidth at a certain frequency. The most popular set-ups, e.g., the anti-Helmholtz coils and the Ioffe-Pritchard trap are presented in Fig. 6.1(a), and the trapping mechanism is illustrated in Fig. 6.1(b).

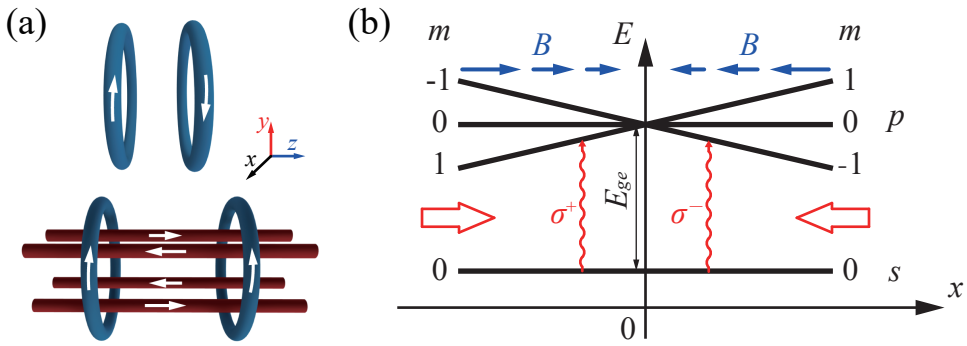


Figure 6.1: **Magneto-optical trap.** (a) The conventional anti-Helmholtz coil and Ioffe-Pritchard trap. The white arrows show the directions of the electric current. (b) Schematic diagram showing the operation of a MOT for atomic motion along the x-axis (a similar picture holds along the y and z directions): The strength of the magnetic field is proportional to x, and its direction is shown by the blue arrows. The Zeeman effect splits the energy of atoms by an amount proportional to m. An s-state atom moving leftwards from $x = 0$ will interact with the right-going circularly polarised light whose energy is slightly below ΔE, and triggers the σ^+ transition by exciting the atom to the $m = 1$ state. In order to maintain the momentum conservation, the atoms are slowed by the photon absorption. The de-excitation process emits photons randomly in all directions so that, on average, the atom slows. A similar deceleration occurs for right-moving atoms that absorb left-moving photons which excites the σ^- transition.

For simplicity, we can show this kind of restoring light force by considering the two-level atoms projected to a ground s-state and an excited p-state. This is also generally true for alkali atoms neglecting their fine structures. A static magnetic field can split p-state into three substates via the Zeeman effect [Fig. 6.1(b)]. The splitting energy is $\Delta E = -mg\mu_B B$, where m is the magnetic quantum number, and $m = 0$ for s-state, $m = 0, \pm 1$ for p-state. g is the Landé g-factor, and μ_B is the Bohr magneton. In MOTs, the strength of the magnetic field is approximately proportional to the distance from the

trapping centre, such that $\mathbf{B} = (\alpha_x x, \alpha_y y, \alpha_z z)$. The excited-state energy consequently splits as the atoms move away from the trap centre, and the energy diagram (along x-axis as an example) is shown in Fig. 6.1(b). The flux conservation of the magnetic field requires that $\alpha_x + \alpha_y + \alpha_z = 0$. For anti-Helmholtz coils, the azimuthal symmetry with respect to z-axis results in $\alpha_x : \alpha_y : \alpha_z = 1 : 1 : -2$.

The laser beams are usually cast towards the centre from six orthogonal directions. Their frequencies are red detuned, i.e., slightly lower than the transition frequency from the ground state to the excited state, E_{ge}. For atoms, the absorption efficiency of photons that excite electrons reaches the peak when the frequency matches, i.e., $h\nu = E_{ge} + \Delta E$, where $h\nu$ is the energy of one photon. Therefore, it preferentially occurs that the atoms moving away from the trap centre can resonantly absorb more photons than those precisely at the centre. This process confines the atoms.

As has been illustrated in Fig. 6.1(b), we let the trapping lasers be circularly polarised, such that the right-going laser can trigger the σ^+ transition, and the left-going laser σ^- transition. This configuration makes the atoms moving to $x < 0$ regime be excited to $m = 1$ state, and $x > 0$ regime to $m = -1$ state. After that, in nanoseconds, the atoms will quickly decay and emit photons isotropically. This process will contribute to a momentum change in all directions with equal probability. For the whole atom ensemble, the net total momentum change is zero, but its variation is non-zero. This is thereby against the cooling mechanism, and will result in a finite temperature at equilibrium.

The width of the laser beams for MOT can be as large as centimetres, which enables a large number of atoms to be trapped and pre-cooled. Usually, MOT is the first step to get the cold atom resources, and other cooling techniques, such as Doppler cooling, Sisyphus cooling and evaporative cooling [22, 23] can be applied for further reduction of temperature and get degenerate gas. The low temperature and large atom number are more or less a pair of contradiction, especially for evaporation. Therefore, it is crucial to get a sufficient number of atoms from the beginning to ensure the successive experiments. The demand for high efficient MOT is thereby of great importance.

The conventional anti-Helmholtz coils in laboratories consist of multiple turns (usually > 100) of copper wires held outside of the ultra-high-vacuum (UHV) chamber. This makes it require huge currents (~ 100 A) in the wires because they are far from the atom cloud. To utilise the space between the coils, and thus achieve more power-efficient trapping, the inside-UHV apparatus are necessary. For example, Ioffe and Pritchard independently designed a magnetic trap to generate the field whose x, y components are quadrupole as shown in Fig.6.1(a,lower) [165, 166]. The four parallel wires generate the quadrupole magnetic field along with the x and y directions, and an additional pair of coils provide the magnetic field for z-directional trapping. The straight electrodes can be integrated inside the chamber and reduce the demand for electric current.

Our primitive design consists of bent metallic bars, which construct the backbone of the new structures by illustrating the main flow of the field-generating electric current. Their topology is inspired by both the Ioffe-Pritchard trap and anti-Helmholtz coils. To further reduce the heat dissipation resulting from the currents, we have investigated compact conductor geometries based on the primitive design. They wrap closely around the atomic cloud, and are suitable for manufacturing by using 3D printing technology. Our designs comprise either 2 or 4 separate conducting parts and 4 current terminals. The streams of the electric current in the bulky metals are similar to that in the twisted bars, but the broader cross-sections allow lower resistance and reduce the power consumption.

6.2 New designs for 3D printing manufacture

First of all, it is important to emphasis on the key relations between the magnetic fields and the geometry of conducting parts under the restriction of the heat dissipation. The fundamental physical laws lead the directions of new designs and ensure their performance.

The static magnetic field provided by the steady electric current is governed by the Biot-Savart law:

$$\mathbf{B}(\mathbf{r}) = \frac{\mu_0}{4\pi} \iiint_{\Omega} \frac{\mathbf{J}(\mathbf{r}') \times (\mathbf{r} - \mathbf{r}')}{|\mathbf{r} - \mathbf{r}'|^3} \mathrm{d}^3\mathbf{r}', \tag{6.1}$$

where Ω is the domain of the current-carrying conductor and $\mathrm{d}^3\mathbf{r}'$ is its differential element.

The working temperature is another fact to be considered. The accumulated electrical heat gives the rise of temperature and, in the long-term, can distort the material and worsen the performance. The electrical heat follows the Joule's law,

$$Q_W = \frac{1}{2}\sigma \iiint_{\Omega} |\mathbf{J}(\mathbf{r})|^2 \, \mathrm{d}^3\mathbf{r}, \tag{6.2}$$

where σ is the conductivity, and is assumed to be homogeneous in the entire device. In the vacuum chamber, the conducting parts only have two ways to release the heat. One is to radiate to the vacuum, which is negligible in comparison to Q_W at ~ 300 K. Another is to transfer the heat along the electrodes following Newton's cooling law,

$$Q_C = \kappa A(T - T_0), \tag{6.3}$$

where κ is the empirical cooling coefficient, A is the area of the cross-section of the electrode and T_0 is the temperature of the environment. The balance of $Q_W = Q_C$ provides the temperature T in equilibrium.

Then we will show a dimensional analysis which reveals the importance of shrinking

the size of the trap for the sake of high performance. We define l to be the linear scale as we resize the whole geometry along with all directions pro-rata. The conductor volume is proportional to the cubic of l, $V_\Omega \propto l^3$, and the cross-section area A depends on the square of l, $A \propto l^2$. The current density under the fixed terminal current is $|J| \propto I/A \propto Il^{-2}$. According to Eq. 6.2, the Joule's heat $Q_W \propto I^2 l^{-1}$. From Eq. 6.3, the leaking heat $Q_C \propto A \times (T - T_0) \propto l^2$. To achieve $Q_W = Q_C$, one can find $I \propto l^{3/2}$. According to the Biot-Savart law (Eq. 6.1), the magnetic field $B \propto I/l \propto l^{1/2}$, and the gradient $\nabla B \propto l^{-1/2}$. Therefore, under the constraint of heat dissipation, it is efficient to pursue a smaller size of MOT for the desired gradient magnetic field.
The magnitude of the magnetic field decays according to $\sim R^{-2}$, where R is the distance from the atom cloud to the current source. The use of multiple parts can enhance the field by constructively adding up their contributions. Therefore, we found that a high-performance MOT should follow several key design criteria:

- Conductors should wrap the optical molasses region tightly and fill as much space as possible around it;
- The trap conductors should be as compact as possible;
- Each bar/conducting volume should always wind in the same direction either clockwise or anticlockwise to maximise its contribution to the magnetic field.

The primitive twisted bar design in Fig.6.2(a) does not need to satisfy all of those criteria. It only reflects the idea of new traps but not make full use of the space to be efficient. The improved designs with more bulky structures should agree with those criteria and guarantee the ratio of the field gradient being 1:1:-2 at the same time.
We achieve the other two improved designs by thickening the conductors to fulfil more space. However, the thickness cannot be arbitrarily large, due to the current far from the trap centre generating a lower magnetic field, and the distribution of the current density is always concentrated in the inner side of a bulky material which make the outer side of the material wasted. Another critical issue is to maintain the ratio of the field gradient, which involves some subtle adjustments to the size of the trap. The dimensions mentioned in this work should be treated as part of the design, as any modification may cause the generated magnetic field out of expectation.

6.2.1 Twisted metal bars design

A primitive design of curvilinear current paths was first demonstrated to illustrate how MOT can be produced without neither straight nor circular structures. Our start point is to modify the Ioffe-Pritchard trap by twisting the four metal bars consistently, which ends up with a cage profile as shown in Fig.6.2(a). The trap is built-up using 3D CAD software Solidworks. The cross-section of the bars is circular with a diameter equal

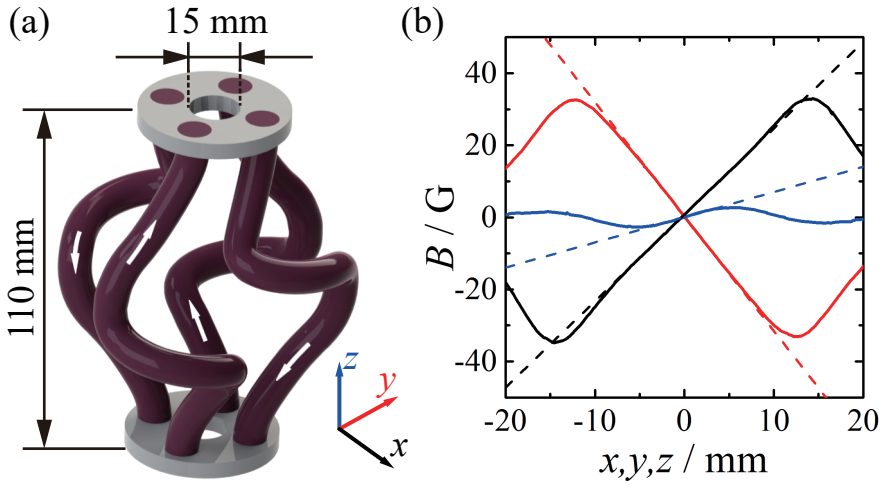


Figure 6.2: **Twisted Metal Bars Design.** (a) A MOT design using twisted metal bars to achieve 3D trapping. The grey discs are dielectric mounts, and the purple parts are the conductive bars. The white arrows show the current flow in each bar. (b) Calculation of the magnetic field magnitude, B, versus position along the x, y and z directions (black, blue and red curves respectively). The gradients near the trap centre along the x, y and z directions are 15.1, 6.5 and -22.1 G/cm (black, blue and red dashed lines).

to 10 mm. The shape of the bars is guided by the parametric equations in spherical coordinates $\{r, \theta, \phi\}$:

$$r(\theta) = \begin{cases} \frac{h}{4}\left(2 - \sqrt{1 - \left(\frac{4\theta}{\pi} - 1\right)^2}\right) & 0 < \theta \leqslant \pi/4 \\ \frac{l}{4} & \pi/4 < \theta \leqslant 3\pi/4 \\ \frac{h}{4}\left(2 - \sqrt{1 - \left(\frac{4\theta}{\pi} - 3\right)^2}\right) & 3\pi/4 < \theta \leqslant \pi \end{cases} \tag{6.4a}$$

$$\phi(\theta) = \begin{cases} \frac{\pi}{3}\left(1 + e^{-10(\theta - \frac{\pi}{3})}\right)^{-1} & 0 < \theta \leqslant \pi/4 \text{ and } 3\pi/4 < \theta \leqslant \pi \\ \frac{\pi}{3}\left(1 + e^{-10(\theta - \frac{2\pi}{3})}\right)^{-1} & \pi/4 < \theta \leqslant 3\pi/4 \end{cases} \tag{6.4b}$$

where $h = 110$ mm is the height of the whole structure. $\mathbf{r} = 0$ is the trapping centre. The outer width is designed to be 55 mm in order to generate the desired magnetic field. These parameters allow the access to 15 mm diameter orthogonal laser beams from the holes in the bottom and top insulating mounts (grey), and the gap between the twisted wires.

We can decompose the shape of the bars to several segments for better understanding of how to generate the magnetic fields. The current in adjacent bars flows in the opposite directions (white arrows). According to the Biot-Savart law, the vertical current component contributes to the horizontal magnetic field, whilst the horizontally twisted current generates the vertical field. The twisted parts intuitively create the vertical component of the magnetic field which is absent in the Ioffe-Pritchard trap, and make up the MOT field in all direction. Due to the anti-symmetric current flow configuration in the

four bars, the strength of the magnetic field vanishes at the centre and increase linearly around it. This scheme can provide the magnetic field required for a MOT.
The physical fields are simulated by COMSOL Multiphysics. We first simulate the electric current in the metal bars with the boundary conditions of fixed electric potential on the ends of the wires. Then we calculate the magnetic field in a box at least 3 times larger than the whole structure using the stationary Maxwell's equations. The boundary condition of the shell of the box is perfect magnetic conductor, which is however insensitive as we simulate the stationary field. As mentioned before, the linearity of Maxwell's equations allows us to scale the solutions of the strength of the magnetic field and current density proportionally with the voltage in the boundary conditions, such that the desired field gradient can be achieved.
In Fig.6.2(b), we plot the field along three axes through the trap centre where the field gradients have approximately constant values of 15.1, 6.5 and -22.1 G/cm along the x, y and z-axes respectively. To generate such a magnetic field, we found the current needed to make the trap is 100 A, and the total electric power dissipation via Joule heating is 14.9 W for copper.
It is still distant from our goal. Although this design illustratively works, there is still much unfilled space between the conductors and the trap centre, making the trap power consumption unnecessarily high. The gradient slope and linear region along z-axis are also less satisfying than those of x, y-axes.

6.2.2 Compact conductor design

Our first improvement, as shown in Fig.6.3, inherits the same topology of the current paths as shown in Fig.6.2. In this case, the total height of the trap is only 45 mm, and its outer width is 24 mm. The holes for the laser beams access are still 15 mm in diameter. We left a gap between the four conductors to be $\sim$ 0.5 mm, which can be filled with dielectric materials for installation and is adjustable to fit the stability in a UHV environment. The design also requires four pairs of voltage contacts to run the trap and control the current in each conducting part. Fig. 6.3(b) shows the exploded image of the design and illustrates the directions of electric current.
Compared to the twisted bar design in Fig.6.2, this structure better satisfies the three aforementioned design criteria. It is 60% smaller and makes better use of space around the atom cloud. The current in the *twisted* parts is more effective to generate the desired field than the previous design. The current in the conductors can be divided approximately into vertical and horizontal components, with the former creating the magnetic field in the xz-plane and the latter generating the field along the z-axis. The currents in adjacent conductors are anti-parallel at the contacts and, at the trap centre, provide a linear magnetic gradient along the x, y and z-axes.

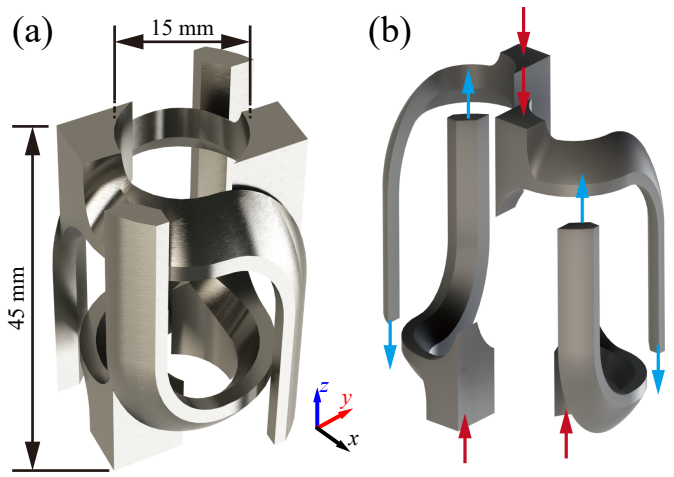


Figure 6.3: **Compact Conductor Design.** (a) Design for a 3D-printed version of the current topology shown in Fig.6.2(b). The four conducting parts are electrically isolated, and the gaps between them can be filled with dielectric materials (not shown). (b) An exploded view of the trap. Red and blue arrows indicate the current input and outflow.

To change the gradient ratio in the three directions, one may easily adjust the length of the conducting prongs. To produce the field gradients close to the 1:1:-2 ratio typically used for MOTs, we choose the height of the device to be larger than its width. To further reduce the resistance and power consumption, one may further increase the thickness of the volumetric conductors.

In Fig.6.4(a), we show a colour map of the current density on the surface of the conductors. In Fig.6.4(b), we show the corresponding magnetic field components B_x, B_y, B_z along the x, y and z-axes and linear fits at the trap centre. The field variations across the xz, xy and zy-planes through the trap centre are shown in Fig.6.4(c-e), where the colour scale shows the field magnitude.

In general, the current flow does not always follow the deigned paths, but goes through the shortest-cut. Its density is the highest at sharp bends in the conductors and less concentrated on the outer side. To avoid current hot spots, we thereby fill the bend regions with curving surfaces, which is possible to realise by 3D printing. The current on the inner conductor surfaces is higher than that at the outer ones, which is suitable for producing the magnetic field in the trap. The decaying profile of the electric current density from the inner surface to the outer also unveils that it is not always necessary to increase its thickness, as long as the total resistance is acceptable. In Fig.6.4(b), the linear fitted slopes near the centre along the x, y and z-axes are 11.5, 11.9 and -22.5 G/cm respectively. The linear fit regime is about 10 mm in diameter, slightly smaller than the size of the holes. The linearity is visually very promising in this regime. The total Joule's heat in the trap is 0.4 W for copper conductors.

The significant improvements compared to the twisted-bars design are based on the

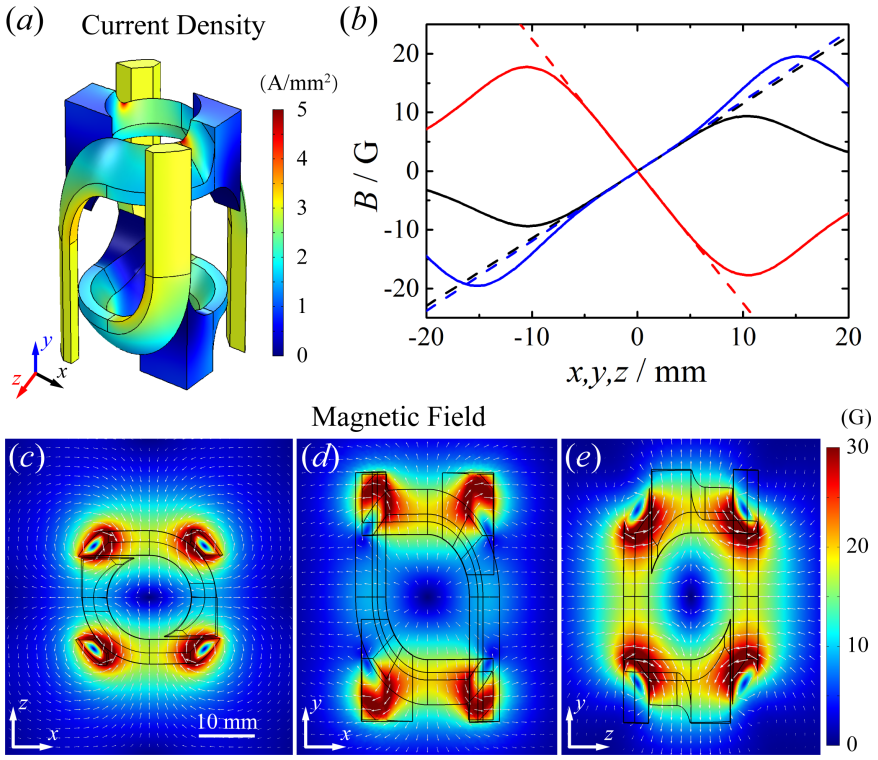


Figure 6.4: (a) Current density distribution calculated for the MOT shown in Fig.6.3, with each conductor carrying 40 A. (b) Calculation of the magnetic field magnitude versus position along the x, y and z-axes (black, blue and red solid lines). The gradients along the x, y and z-axes at the trap centre are 11.5, 11.9 and -22.5 G/cm respectively (black, blue and red dashed lines). (c-e) The magnetic field magnitude in the xz, xy and zy-planes through the centre of the MOT. In each plane, there is a minimum at the centre. The gaps between the four conductors are just large enough for a 1.5 cm diameter laser beam to pass through.

compactness. The twisted parts in this design are almost horizontal, which ensures the generated field being vertical, and the gradient along the z-axis can be strengthened. The vertical parts are also nearly parallel to the z-axis, which makes the generation of the quadrupole field in the xy-plane more efficient than the previous design. Therefore, the compact design not only reduces the space and consumption, but can also improve the performance of the yielding fields.

A shortcoming of this design is that we need to print four parts (Fig.6.3) and either fix them separately, or print dielectric material between each part to maintain the integrity of the structure. Such an arrangement is possible, but still a challenge for current Additive Manufacturing techniques. Another problem is the need of 8 terminals to drive the trap, which is also complicated for in-chamber experiments. In the next section, we consider further simplification of the design to remove this issue by reducing the number of separate conductors.

6.2.3 Two-piece conductor design

In this section, we will propose a further improvement with only two pieces of conductor parts and four terminals for current supply.
The idea is still to create the desired field with the combination of quadrupole bars and rings. Here, we start from a cylinder and cut it into two pieces. First, we produce three orthogonal laser-access holes with circular cross-sections, then separate that conductor into two parts as shown in Fig. 6.5(a). The gaps can also be filled with dielectric materials for installation, and we keep it to be 0.5 mm the same as the previous design. The electric current will flow in and out of the straight arms through a roughly circular path in between [Fig. 6.5(b)]. The parallel straight arms will provide a quadrupole field in the trap centre in the *xy*-plane, and the approximately circular current will create the field pointing towards the trap centre along the *y*-axis.
This geometry takes advantage of filling almost the whole volume surrounding the laser beams with the conductor, thereby reducing the resistance of the current paths. The size of the trap is also manually modified for the best performance mainly regarding the ratio of the field gradient. The diameters of the holes are fixed to be 15 mm as for the laser access. We did the independent simulations for various parameters and finally found out that when the height is 38 mm, outer diameter is 26 mm, and the thickness of the arm is 3.1 mm, the ratio of the magnetic field gradient can be 1.0:1.0:-1.9 as we expected.

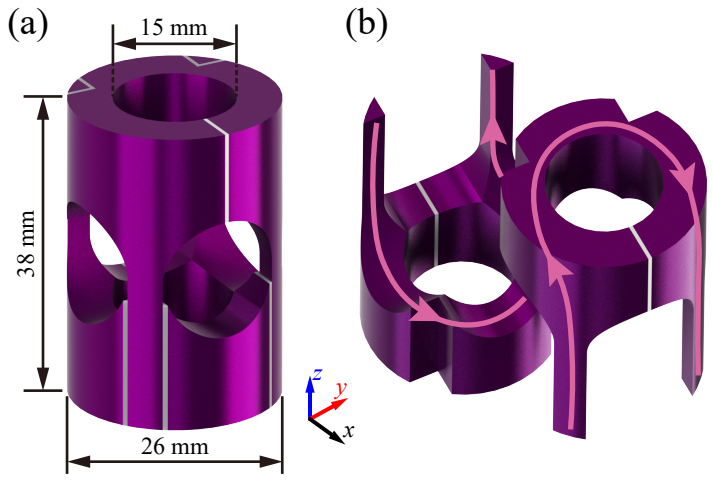


Figure 6.5: (a)A 3D-printed MOT design with conductors that have a cylindrical outer curved surface. The shape is inspired by the Ioffe-Pritchard trap. (b) An exploded view of this model showing the two conductors. The pink lines and arrows show the directions of the current. Gaps between the conductors appear white.

From the current density plot, we found that the current is significantly concentrated in the straight arms. This is due to the geometry that the cross-sections in the straight arms are smaller and become more expansive in the ring parts. Despite the difference in the

current density, the total currents are still the same, which contribute the straight parts being equivalent to that in the rings. This design does not have reflection symmetry with respect to the zx-plane, but the resulting magnetic field still shows superior performance.

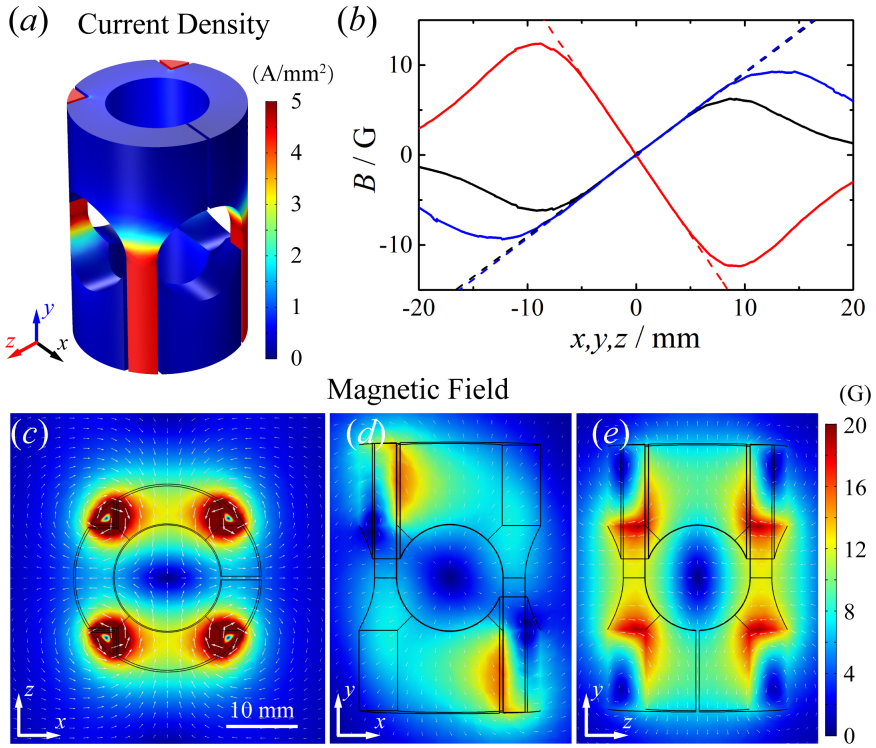


Figure 6.6: (a) Current density distribution calculated for the MOT shown in Fig.6.5, with each conductor carrying 25 A in total. (b) Calculation of the magnetic field magnitude versus position along the x, y and z-axes (black, blue and red solid lines). The gradients along the x, y and z-axes at the trap centre are 8.98, 9.20 and -17.6 G/cm respectively (black, blue and red dashed lines). (c-e) The magnetic field magnitude in the xz,xy and zy-planes through the centre of the MOT. In each plane, there is a minimum at the centre. The circular holes in the trap are just large enough for a 1.5 cm diameter laser beam to pass through.

We set the current to be 25 A in each conductor, and simulated the electromagnetic field in the same way as mentioned in other designs. The current density and magnetic field are plotted in Fig. 6.6. The current density in each arm is $\sim$5 A/mm^2. In the ring-like regions, by contrast, the current density is significantly smaller, below 1 A/mm^2. By design, there is no hot spot in the current density so the trap will be heated uniformly. The total Joule heat in the trap is $\sim$ 0.2 W for copper.

Fig.6.6(b) shows the magnetic field components B_x, B_y, B_z along the x, y and z-axes and linear fits (dashed lines) near the trap centre. The ratio of their gradients is close to $1:1:-2$ along x, y and z-axes, specifically, 9.0, 9.2 and -17.6 G/cm respectively with an uncertainty of $\sim$ 0.03 G/cm in each case under our simulation conditions.

Here we should bear in mind that the material in simulation is set to be copper, whose conductivity is 5.96×10^7 S/m. The most common materials for 3D printing, however,

are usually titanium and nickel alloys, which have $\sim$ 10 times larger resistance than copper. Thus, to provide the same magnetic field using these materials will require about 2 W in power dissipation in the conductors. Nevertheless, this is not a fixed value, and the real results depend on the printing technologies, which is still rapidly growing. For example, we will show that a quenching process applied to the material can significantly increase its conductivity. The details are shown in the last section.
As the only way for heat dissipation is that through the ends of the arms, we estimate the transfer coefficient for the device. Considering the total power dissipation is ~ 0.2 W for copper, and the transfer area is $\sim 4 \times 10^{-5}\mathrm{m}^2$ in total, in order to maintain the temperature increase below an experimentally-tolerable limit of 200 K, the heat transfer coefficient should be around 25 $\mathrm{W/m^2K}$. This is practical for experimental set-ups and, if additional external cooling can be applied to the trap, the operating temperature can be made lower than 470 K.

6.3 Time response

A significant concern in MOT-based quantum devices is the switching time of the atom trap. In order to minimise the current flow and power dissipation, coils with multiple turns are preferred, which leads to high inductance. Since the relaxation time, or LR constant, of an inductor is $\tau = L/R$, a high inductance will slow the switching process which may limit experiments. One solution may be to increase the resistance, R, which will reduce the relaxation time, but increase the power consumption and the local temperature of conductors. Therefore, balancing the inductance and the resistance becomes a crucial problem for structural design.
To make a comparison with anti-Helmholtz coils, we found coil parameters that generate the same magnetic field gradient as the 3D printed structure shown in Fig.6.6 with the same electric current. The inner diameter of the coils, and their separation, is 15 mm. The outer radius and height of the coil are respectively 3.8 mm and 4.5 mm. We also extrude the electrode arms in our design 20 cm longer to touch the boundary of the simulation box, such that AC field can be applied for inductance analysis.
Here we propose two methods to estimate the time response of the coils. First, we consider the DC regime. Here we can use the energy of stationary magnetic field stored in the coil using the relation for lumped inductor $E_H = \frac{1}{2}LI^2$, where E_H can be acquired by integration according to $E_H = \int d^3\mathbf{r} \frac{1}{2\mu_0}|\mathbf{B}|^2$. This idea holds on that the magnitude of the magnetic field decays quickly towards the solution domain and nearly vanishes on its boundary. The resistance can be calculated by Joule's heat W according to $W = I^2R$ as expected in the DC field. For the anti-Helmoholz coil, the results yield $L = 83.6$ nH, $R = 0.206$ mΩ, and $\tau = 405$ μs. In comparison, the designed one shows $L = 122$ nH, $R = 0.630$ mΩ, and $\tau = 193$ μs. Although the inductance and the resistance of

the 3D printed structure are both higher than the traditional anti-Helmholtz coil, their ratio is lower which makes the switching time almost twice as fast. However, we note that the inductance depends on the whole electric circuit, especially the connecting leads, which are not considered here, and the distributed capacitance will also slow the response. And the gap between conductors is assumed to be large enough such that there is no free charge accumulation.

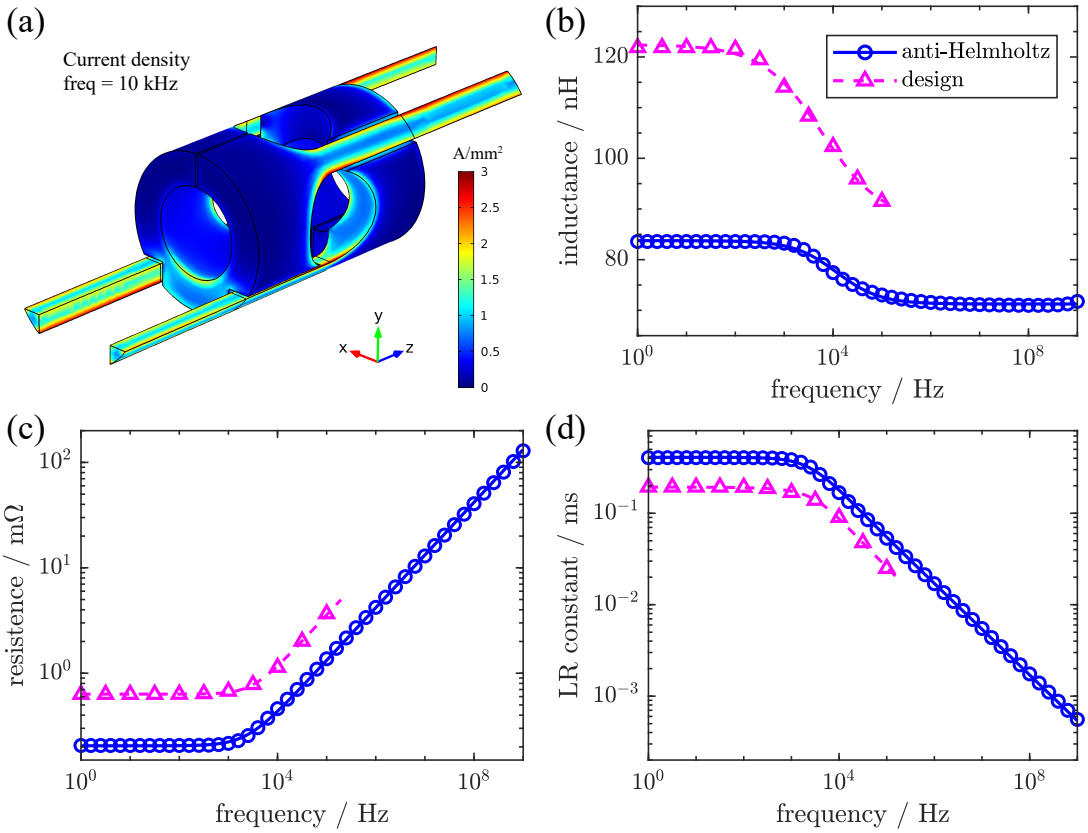


Figure 6.7: Inductance, resistance, and LR constant for anti-Helmholz coil (blue) and our designed 3D coil (pink). The markers are simulation results and lines are fitting curves.

Second, we applied AC current to the coils and evaluated the LR constants by the built-in coil analyser in COMSOL [167, 168]. The frequency-domain analysis helps us to understand the temporal performance of AC-MOT. Because of the large skin effects in high-frequency regime above MHz, we swept the frequency f from 1 Hz to 100 kHz in the 3D model. For $f = 10^4$ Hz (Fig.6.7a), the current density shows noticeable skin effects, and the skin depth is already in the same order of our mesh finesse. However, for anti-Helmohz coil, we simplified the geometry to a 2D model using the rotational symmetry, such that finer mesh can be utilised to push up the frequency to 100 MHz. We present the simulation results in Fig.6.7b (inductance), c (resistance), d (LR constant). Both the anti-Helmholz coil and design 3D coil have a similar dependency to frequency. The inductance has different asymptotic values in both low-frequency and

high-frequency regime, and there is a transition zone between 1∼100 kHz. The resistance is almost constant when $f < 1$ kHz, but increases dramatically after that. In contrast, LR constant changes slowly when $f < 1$ kHz but decreases dramatically afterwards. The inductance and resistance can be fitted by empirical equations as studied in transmission lines [169, 170]

$$L = \left(L_0 + L_\infty \left(\frac{f}{f_L}\right)^{\beta_L}\right) \Big/ \left(1 + \left(\frac{f}{f_L}\right)^{\beta_L}\right), \tag{6.5}$$

$$R = R_0 \left(1 + \left(\frac{f}{f_R}\right)^{\frac{\beta_R}{2}}\right)^{\frac{1}{\beta_R}}. \tag{6.6}$$

In the low-frequency limit, $L \to L_0$ and $R \to R_0$. We found that for anti-Helholz coil, $L_0 = 83.8$ nH, $R_0 = 0.205$ mΩ, and $\tau = 409$ μs. For designed 3D coil, $L_0 = 122$ nH, $R_0 = 0.633$ mΩ, and $\tau = 193$ μs. They agree with the stationary calculation results with little difference. In the high-frequency limit, we show that the inductance relaxes to asymptotic value L_∞ which is still in the same order of L_0, the decrease is only 15% to 30%. The resistance, however, will increase with frequency according to $R \sim \sqrt{f}$. This scaling originates from the skin depth $\delta = 1/\sqrt{\pi f \mu_0 \sigma}$, and $1/\delta$ signifies the conducting cross area at high-frequency. Therefore, the LR constant will decrease as $\tau \sim 1/\sqrt{f}$ solely due to the resistance. We note that although the decrease of LR constant may lead to faster response, the increasing impedance caused by R will inhibit the realisation of high-frequency AC-MOT due to Joule's heat.

Finally, we make a comparison between the anti-Helmholz coil and our design. Noticing the logarithm scale in Fig.6.7, the LR constant is always 50% smaller for our design at any frequency. This is the primary advantage of our design. However, considering the total impedance $Z = R + j2\pi f L$, and L, R are both larger in our design, the dissipation loss is greater, which should be taken into consideration for high-frequency use.

6.4 Experimental test

The experimental test of the two-piece conductor design has been carried out by our collaborator P. Krüger and R. Wildman's group (details can be found in [4]).

The design has been modified with four arms for connecting terminals to fit in the vacuum chamber. The sample was printed by selective laser melting (SLM) machine with Al-Si10-Mg alloy. The resistance has been measured to be (800 ± 20) $\mu\Omega$. It can be reduced by a baking and quenching process, and finally results in (640 ± 4) $\mu\Omega$ [Fig. 6.8(a)]. This is merely 1% from our simulation, and suggests that the Al-Si10-Mg alloy can be as conductive as copper after the baking and quench process.

The magnetic field in the MOT has been measured under 14 A current supply as shown

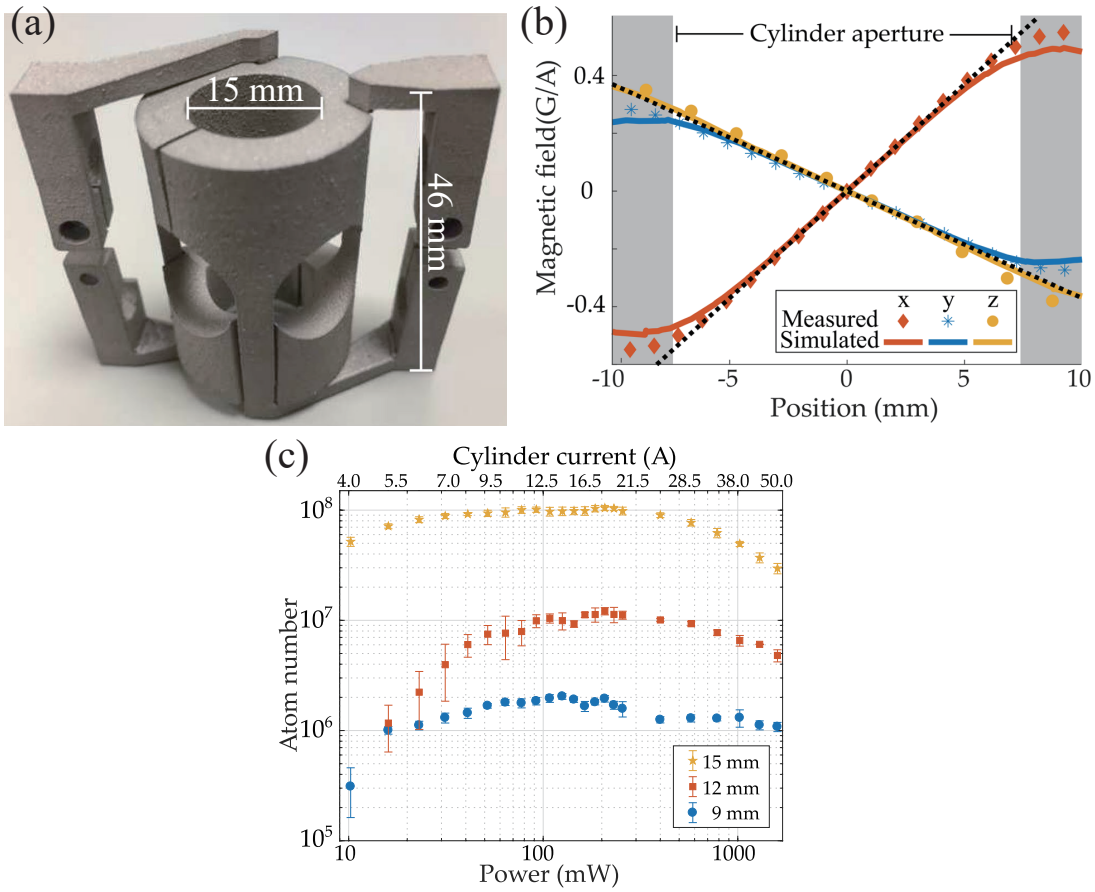


Figure 6.8: **Experiment outcome of the 3D printed MOT.** (a) 3D-printed atom chip structure. (b) Measured magnetic field magnitude along each axial direction with markers. The ideal linear field with $1:1:-2$ ratio is plotted as the dashed lines. The linearity maintains throughout the cylinder aperture. (c) The maximum number of trapped atoms as a function of the electrical power consumption (or electric current) for beam diameters of 9,12 and 15 mm.

in Fig. 6.8(b). The resulting gradient reached 10 G/cm (weak direction) under the operation current being 14 A, and the total energy dissipation was about 100 mW. When the current was increased to 50 A, the gradient increased to 37 G/cm. The numerical simulation and measurement results were also highly consistent.

The inductance of the printed device has been measured and yields $(0.49 \pm 0.05)\ \mu$H, about 4 times larger than the L_0 in theory. This is measured by connecting the device with a capacitor for a series LC circuit. The resonance frequency is given by $f_{\text{res}} = 1/(2\pi\sqrt{LC})$. Then we change the value of the external capacitor for different resonance frequency. The inductance can be extracted from the fitting results. However, as the operating frequency has been seen above ~ 100 MHz, the resulting inductance is valid for high-frequency limit. Besides, the experiment showed that the decay time of the magnetic field in MOT was $13.0 \pm 2.3\ \mu$s, one order faster than simulation. This can be a result of the surface defects. The roughness of the surface can enormously increase the resistance in high-frequency limit due to skin effect, and thereby reduce the LR constant

significantly. The faster response requires higher energy consumption, which is also a trade-off for practice. So far, the heat dissipation is acceptable in our experiments.
To test the trapping performance, we trapped ^{87}Rb atoms via the D2 line. We used three types of laser beams with different diameters, and its peak intensity is 4 mW/cm^2. The power of the MOT was modified by varying the current from 4 to 50 A, and the power consumption ranged from 10 mW to 1.6 W. The detuning of the cooling light was always optimised for the maximal trapping. As shown in Fig. 6.8(c), the increasing diameter of the beams from 9 to 15 mm helps to trap more atoms, with the maximum value close to 10^8 for the power between 100 and 200 mW, referring to the current ranging from 12 to 17 A as expected. Apparently, larger beam width will trap more atoms, and making full use of the holes in our device is important.

6.5 Conclusion and discussions

We have made a prototype of the new design of MOT with 3D printing technology. From theory to experiment, our design paves the way to miniaturisation and portability of the next-generation of atom-based quantum devices. The scaling of the dimensions of new designs has been manifested by physical laws, which guarantees the production of cold atom resource under the restricted energy dissipation and time response.
The ongoing problems remain on the flexibility of the specific structures to be adapted to further quantum operations, e.g., the access to the probe beams, the RF fields for vapour cooling, and the pathways for atom interference. One can also expect the 3D printing technique help to replicate small apparatus to the extended system, such that numerous experiments can be carried out simultaneously as well as the realisation of the entanglement of multiple quantum systems.

Chapter 7

Project: Fermi Surface Deformation of Rydberg-Dressed Atoms

Recent experiments and theories have shown that Rydberg-dressing offers a promising approach to engineering the long-range interactions in cold atom systems for the studies of many-body physics. Apart from traditional Fermi liquid and superconductor theories in solid-state materials, a large variety of quantum states such as the nematic phase [171], FFLO phase [172], charge density wave and supersolid [173]., have been explored or demonstrated in ultracold atom systems. The interaction has played an essential role in these aspects. In this chapter, we will present the possibility to achieve the anisotropic quantum states with Rydberg-dressing, which broadens the utility of ultracold atoms as quantum simulators.

The anisotropic interactions in ultracold Fermi gas have been realised with dipole-dipole interactions, which result in the deformation of Fermi surface and anisotropic zeroth sound [174, 175]. A weak elliptical deformed Fermi surface has been observed in the experiment reported in Ref. [176]. Here, we focus on the Rydberg-dressing, which provides a wider range of the controllability of the interaction strength, anisotropy, etc. We explored the interaction profiles of different Rydberg states for ^{6}Li and ^{40}K atoms, and picked up the most anisotropic ones. We calculated the Fermi surface deformation numerically, and found several scaling relations about the interaction strength.

In Section 7.1, we introduce the Hartree-Fock-Bogoliubov approximation for the ground state of interacting fermions. In Section 7.2, we show the different interaction parameters in ^{6}Li and ^{40}K atoms. In Section 7.3, we show the Fermi surface deformation of ^{6}Li with numerical methods.

7.1 Hartree-Fock-Bogoliubov approximation

To begin with, we consider a system of atoms trapped in the electromagnetic fields with their occupation fully polarised to one single hyperfine state, such that the spin degree of freedom is neglected. We start with the Hamiltonian of spinless fermions with two-

body interaction at zero temperature, which reads

$$H = \int \mathrm{d}^3\mathbf{r}\ \hat{\psi}^\dagger(\mathbf{r}) \left[-\frac{\hbar^2}{2m}\nabla^2 + V_{\mathrm{ext}}(\mathbf{r}) - \mu \right] \hat{\psi}(\mathbf{r}) + \iint \mathrm{d}^3\mathbf{r}\mathrm{d}^3\mathbf{r}'\ \hat{\psi}^\dagger(\mathbf{r})\hat{\psi}^\dagger(\mathbf{r}')V(\mathbf{r},\mathbf{r}')\hat{\psi}(\mathbf{r}')\hat{\psi}(\mathbf{r}). \tag{7.1}$$

The first part consists of the kinetic energy, external trapping potential V_{ext} and the chemical potential μ, which determines the number of atoms. The second part is the two-body atom interaction. $V(\mathbf{r},\mathbf{r}')$ is dominated by Rydberg-dressing as introduced in Section 3.3.

We assume the density in real space is homogeneous, which can be achieved by applying a shallow trapping potential or even put the atoms in a box potential, and V_{ext} is dropped out. However, despite the presence of V_{ext}, the translational symmetry in real space is still breakable under strong interactions. This may lead to density waves and is beyond the scope of this work [177]. However, if we restrict ourselves in weak interaction regime, it is known that the fermions are in the so-called Fermi liquid phase for repulsive interaction, and BCS phase for attractive interaction [178]. Both cases can be well described in momentum space.

The Hamiltonian in momentum space, or reciprocal space, is attained by Fourier transformation of field operator $\hat{\psi}(\mathbf{r})$ to $\hat{a}_{\mathbf{k}} = \sum_{\mathbf{r}} e^{i\mathbf{k}\cdot\mathbf{r}}\hat{\psi}(\mathbf{r})$. Under the Hartree-Fock-Bogoliubov (HFB) approximation, the Hamiltonian reads (Appendix C, [179])

$$H = \sum_{\mathbf{k}} \left[\frac{|\mathbf{k}|^2}{2m} + U_H + U_F(\mathbf{k}) \right] \left(\hat{a}^\dagger_{\mathbf{k}}\hat{a}_{\mathbf{k}} + \hat{a}^\dagger_{-\mathbf{k}}\hat{a}_{-\mathbf{k}} \right) + \Delta(\mathbf{k})\hat{a}^\dagger_{\mathbf{k}}\hat{a}^\dagger_{-\mathbf{k}} + \Delta^*(\mathbf{k})\hat{a}_{-\mathbf{k}}\hat{a}_{\mathbf{k}}, \tag{7.2}$$

with

$$\text{Hartree direct energy} \qquad U_H = \rho\tilde{V}(0), \tag{7.3a}$$

$$\text{Fock exchange energy} \qquad U_F(\mathbf{k}) = -{\sum_{\mathbf{k}'}}'\tilde{V}(\mathbf{k}-\mathbf{k}')\langle\hat{a}^\dagger_{\mathbf{k}'}\hat{a}_{\mathbf{k}'}\rangle, \tag{7.3b}$$

$$\text{Bogoliubov order parameter} \qquad \Delta(\mathbf{k}) = {\sum_{\mathbf{k}'}}'\tilde{V}(\mathbf{k}-\mathbf{k}')\langle\hat{a}_{-\mathbf{k}'}\hat{a}_{\mathbf{k}'}\rangle, \tag{7.3c}$$

and ρ is the density of particles $\rho = \langle\hat{a}^\dagger_{\mathbf{k}}\hat{a}_{\mathbf{k}}\rangle$. $\sum'$ refers to the summation of a half of the momentum space in order to get rid of the duplication of $\mathbf{k}$ and $-\mathbf{k}$.

For homogeneous gas, the Hartree term can be absorbed into the chemical potential as a constant energy shift. The Fermi surface deformation is dominated by the Fock term and Bogoliubov term, but by two different implications. The Fock exchange energy will change the shape of the Fermi surface. For example, the ground state of non-interacting fermions is described by a Fermi sphere in the momentum space, but becomes an ellipsoid with anisotropic interactions. The Bogoliubov term does not change the shape of the Fermi sphere, but will smooth out the density distribution in the vicinity of the

Fermi level due to the formation of the Cooper pairs. The pair density can be evaluated by $\rho_p \equiv N_p/\mathcal{V} = \sum_{\mathbf{k}} |u_{\mathbf{k}}|^2 |v_{\mathbf{k}}|^2 = \sum_{\mathbf{k}} n_{\mathbf{k}}(1-n_{\mathbf{k}})$, where $u_{\mathbf{k}}$, $v_{\mathbf{k}}$ are the parameters in BCS wave function $|\mathrm{BCS}\rangle = \prod_{\mathbf{k}} \left(u_{\mathbf{k}} + v_{\mathbf{k}} \hat{a}^\dagger_{\mathbf{k}} \hat{a}^\dagger_{-\mathbf{k}}\right) |0\rangle$. Furthermore, if $\Delta(\mathbf{k})$ is 0, the HFB approximation will be reduced to the HF approximation.

7.2 Anisotropic Rydberg-dressed interaction

As we have discussed in Chapter 3, atoms dressed to Rydberg $|n, l > 0\rangle$ states will lead to anisotropic interactions. There are two questions: First, what is the shape of the dispersion coefficient C_6 with respect to (θ, ϕ)? Second, does anisotropy depends on the principal quantum number n?

Here, we evaluated the C_6 coefficients for ^{6}Li and ^{40}K atoms for their nS, nP and nD states, respectively. In the absence of a transverse field, the atomic interactions have azimuthal symmetry, such that ϕ is irrelevant in our case. We show the results in Fig: 7.1 for $n = 60$.

Here we notice several features. First, the nS states are indeed isotropically repulsive. Second, the anisotropy of nP, nD states are well captured by the ratio of $C_6(0)/C_6(\pi/2)$, as $C_6(\theta)$ is monotonic from $\theta = 0$ to $\theta = \pi/2$. Third, not all states are suitable for Rydberg-dressing. As we have shown in Chapter 3, the sign of C_6 is better to be maintained the same for all directions, which is not true for ^{40}K at nD states with $m_j > 1/2$. Comparing all the states in Fig. 7.1, we found that ^{6}Li achieves the maximal anisotropy at $nD_{5/2}$ $(m_j = 5/2)$ state, and ^{40}K prefers to $nP_{3/2}$ $(m_j = 3/2)$. To further confirm these observations with n taken into consideration, we plot $C_6(0)/C_6(\pi/2)$ in Fig. 7.2. For ^{6}Li, the ratio $C_6(0)/C_6(\pi/2)$ is insensitive to n, which means the maximum anisotropic interaction can be realised at any n. The most anisotropic state is indeed $nD_{5/2}$ $(m_j = 5/2)$ state. For ^{40}K, the ratio $C_6(0)/C_6(\pi/2)$ has resonant behaviour for $nP_{1/2}$ $(m_j = 1/2)$, $nP_{3/2}$ $(m_j = 3/2)$ and $nD_{3/2}$ $(m_j = 1/2)$ states. To be more specific, we plot the ratio $C_6(\theta)/C_6(0)$ in Fig. 7.2(d) for ^{40}K at $nP_{3/2}$ $(m_j = 3/2)$ state. We can find that there is a lobe for $n < 44$ where the ratio is negative, which means the sign of the interaction is different at $\theta = 0$ and $\theta = \pi/2$. However, if one expects to have an interaction with C_6 having the same sign at all directions, it is a better choice to use $44P_{3/2}$ $(m_j = 3/2)$ state for maximum anisotropy. As a comparison, ^{6}Li does not have this problem, as the ratio $C_6(\theta)/C_6(\pi/2)$ plotted in Fig. 7.2(c) is independent to n for $nD_{5/2}$ $(m_j = 5/2)$.

7.3 Ground state of ultracold ^{6}Li gas

In the previous section, we have found two optimal states with the maximum anisotropy for ultracold atom experiments. For ^{6}Li, $nD_{5/2}$ $(m_j = 5/2)$ state offers highly

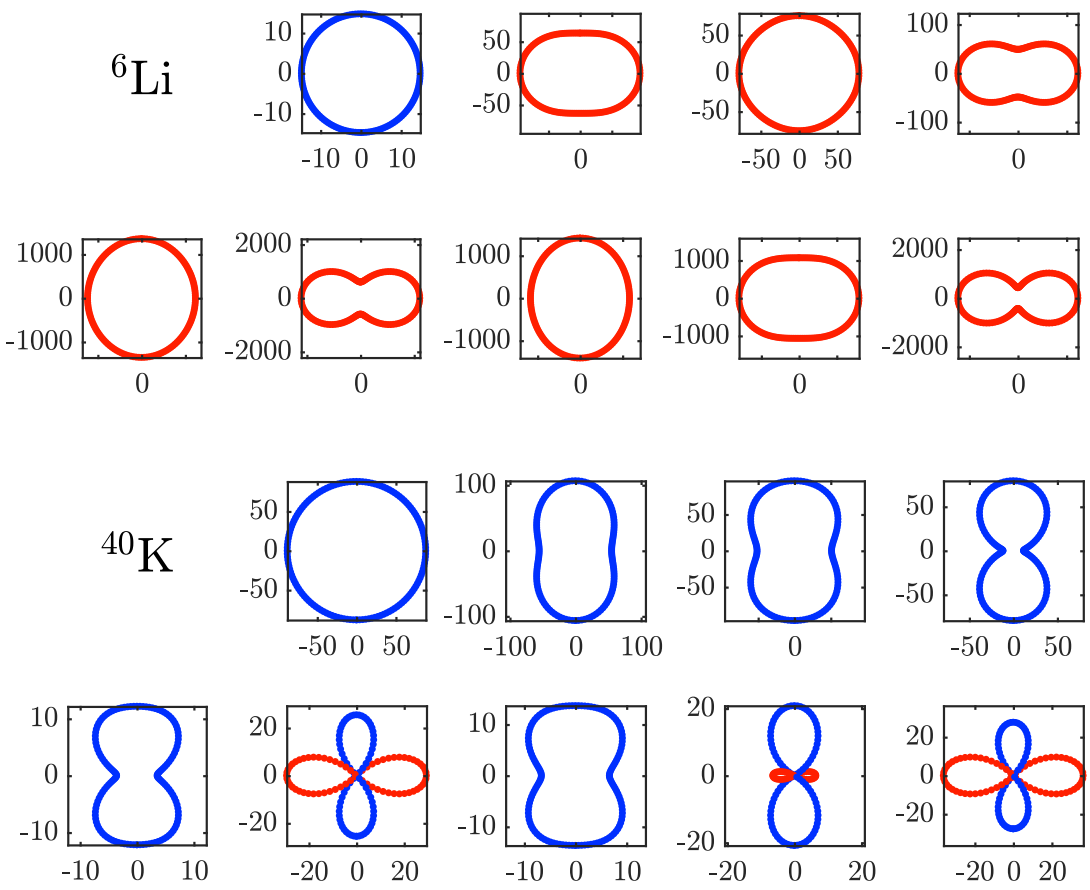


Figure 7.1: $C_6(\theta)$ parameters for ^{40}K and ^{6}Li with in (z,x) for $n = 60$. The orbital and spin configuration for the first row: $S_{1/2}$ $(m_j = 1/2)$, $P_{1/2}$ $(m_j = 1/2)$, $P_{3/2}$ $(m_j = 1/2)$, $P_{3/2}$ $(m_j = 1/2)$, the second row: $D_{3/2}$ $(m_j = 1/2)$, $D_{3/2}$ $(m_j = 3/2)$, $D_{5/2}$ $(m_j = 1/2)$, $D_{5/2}$ $(m_j = 3/2)$, $D_{5/2}$ $(m_j = 5/2)$. Blue is negative value for repulsive force, and red is positive for attractive force. Unit: GHz μm^6.

anisotropic attractive interaction, and for ^{40}K, $nP_{3/2}$ $(m_j = 3/2)$ $(n \geqslant 44)$ offers repulsive interaction. Here we will only focus on the ^{6}Li, because both Fock term and Bogoliubov term are present, and we can see both the Fermi surface deformation and the formation of Cooper pairs.

7.3.1 Self-consistent approach

The ground state of Eq. (7.2) can be solved by self-iteration. We derive the particle distribution in the momentum space with the order parameter. The Bogoliubov theory shows that

$$\langle \hat{a}^\dagger_{\mathbf{k}} \hat{a}_{\mathbf{k}} \rangle = \frac{1}{2}\left(1 - \frac{\xi_{\mathbf{k}}}{\sqrt{\xi^2_{\mathbf{k}} + |\Delta(\mathbf{k})|^2}}\right), \tag{7.4a}$$

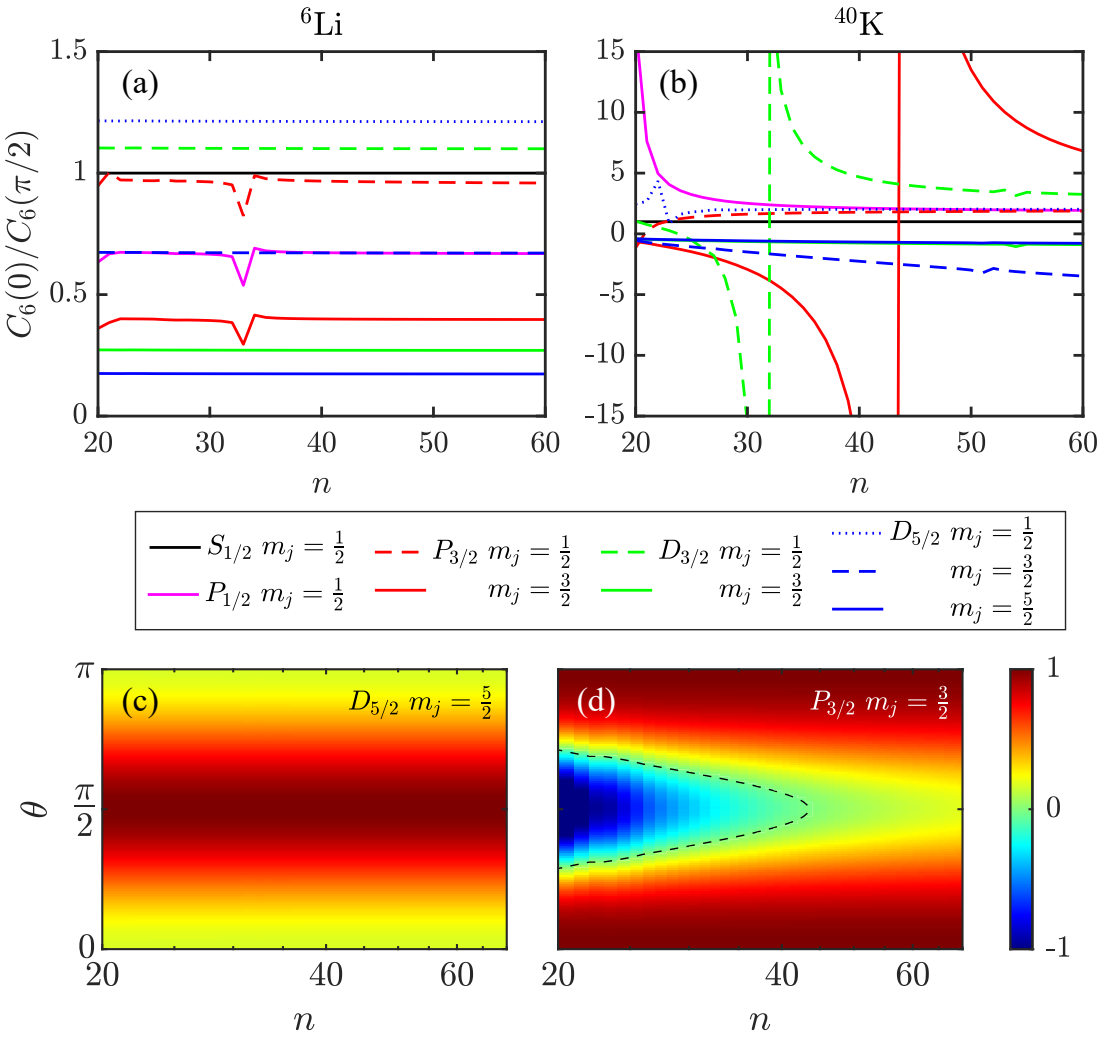


Figure 7.2: Ratio of the C_6 parameters at $\theta = 0$ and $\pi/2$ for S, P, D states and (a) for ^{6}Li, (b) for ^{40}K. (c) $C_6(\theta)/C_6(\pi/2)$ for ^{6}Li at $D_{5/2}$ ($m_j = 5/2$). (d) $C_6(\theta)/C_6(0)$ for ^{40}K at $P_{3/2}$ ($m_j = 3/2$).

$$\langle \hat{a}_{\mathbf{k}} \hat{a}_{-\mathbf{k}} \rangle = \frac{\xi_{\mathbf{k}}}{2\sqrt{\xi_{\mathbf{k}}^2 + |\Delta(\mathbf{k})|^2}}, \tag{7.4b}$$

$$\xi_{\mathbf{k}} = \frac{\hbar^2}{2m} |\mathbf{k}|^2 - \mu + U_F(\mathbf{k}). \tag{7.4c}$$

But here is an unfixed chemical potential μ, which should guarantee the conservation of the total number of particles. Therefore, we adopt the Nelder-Mead algorithm to find μ of each step. The pseudo-code of the whole self-consistent method is listed below:
As a demonstration, we calculated the deformation of the Fermi surface for ^{6}Li at $nD_{5/2}$ ($m_j = 5/2$) with $n = 35$ and 45, respectively, in Fig. 7.3. We let the Rabi frequency of the dressing laser be $\Omega = 2\pi \times 10$ MHz, detuning $\delta = -2\pi \times 50$ MHz, the original Fermi vector $k_F = 2\ \mu\text{m}^{-2}$, and the density $\rho = 1.35 \times 10^{11}\ \text{cm}^{-3}$. We have shown the distribution in the momentum space $n(\mathbf{k})$, the difference compared to the

Algorithm 1 Hartree-Fock-Bogoliubov Self-consistent Method

Initial conditions: ▷ Start from free Fermi gas
chemical potential: $\mu = E_{F0}$ $(\mu_1 = \mu)$
occupation: $v_{\mathbf{k}}^2 = \Theta(k_{F0} - |\mathbf{k}|)$
gap: $\Delta(\mathbf{k}) =$ rand. ▷ To avoid postulated symmetry
total number of particles $N_0 = \dfrac{1}{6\pi^2 k_{F0}^3}$ $(N_1 = N_0)$ ▷ To be fixed
repeat
    Update $U_F(\mathbf{k})$
    Find another μ_2, calculate total number of particles N_2
    repeat ▷ Use Nelder-Mead algorithm
        Reorder (μ_1, N_1) and (μ_2, N_2), such that $|N_1 - N_0| < |N_2 - N_0|$
        if $(N_1 - N_0)(N_2 - N_0) > 0$ **then**
            $\mu_2 = \mu_1 + \alpha(\mu_1 - \mu_2)$ ▷ Reflect and expand μ_2, $\alpha > 1$
        else
            $\mu_2 = \mu_2 + \beta(\mu_1 - \mu_2)$ ▷ Shrink μ_2, $\beta < 1$
        end if
        Update N_2
    until N converges, **return** μ, N, $n_{\mathbf{k}}$
    Calculate $\xi_{\mathbf{k}}$, $\Delta(\mathbf{k})$, $n_{\mathbf{k}}$, etc.
until μ converges

non-interacting Fermi gas $n(\mathbf{k}) - n_0(\mathbf{k})$, where $n_0(\mathbf{k}) = \Theta(k_F - |\mathbf{k}|)$, and the order parameter $\Delta(\mathbf{k})$.

The ground state has shown great anisotropic behaviour for Rydberg-dressed atoms. In term of the deformation of the Fermi sphere due to the exchange energy, one can use the aspect ratio

$$\alpha = k_F'(0)/k_F'(\pi/2) \tag{7.5}$$

to measure the deformation [176]. Generally, for the smoothed $n(\mathbf{k})$, $k_F'(\theta_{\mathbf{k}})$ can be evaluated by the half-height of $n(\mathbf{k})$, such that $n[k_F'(\theta_{\mathbf{k}})] := \frac{1}{2}\max[n(\mathbf{k})]$. In the cases shown in Fig. 7.3, the value of $|\alpha - 1|$ is in the order of $1\% \sim 0.1\%$. However, the smoothness of $n(\mathbf{k})$ in the vicinity of the Fermi surface due to the pairing is more significant. We introduce the variance to signify the change of $n(\mathbf{k})$ which reads

$$\sigma^2 = \frac{1}{\rho}\int \frac{\mathrm{d}^3\mathbf{k}}{(2\pi)^3}\left[n(\mathbf{k}) - n_0(\mathbf{k})\right]^2, \tag{7.6}$$

where $n_0(\mathbf{k}) = \Theta(k_F - |\mathbf{k}|)$. Both $n_0(\mathbf{k})$ and $n(\mathbf{k})$ satisfy the normalisation condition that their integrals are equal to ρ, and they can be measured by the standard time-of-flight imaging. The link between BCS theory under HFB model and FL theory under HF model can be established by defining the aspect ratio. Though the Fermi surface is blurred in BCS due to the Cooper pairs, we can find out the half-height contour of $n(\mathbf{k})$, i.e., $n[k_F'(\theta_{\mathbf{k}})] \stackrel{!}{=} \frac{1}{2}\max[n(\mathbf{k})]$, to substitute the Fermi surface as well-defined in HF

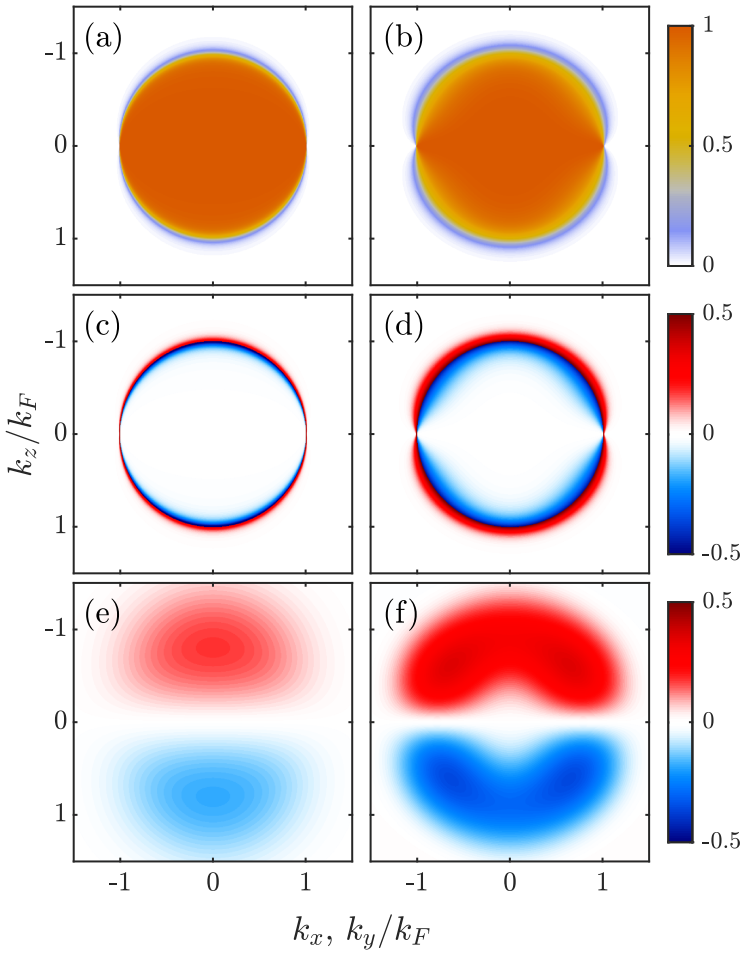


Figure 7.3: Ground state of Rydberg-dressed ^{6}Li atom gas in the momentum space. The target Rydberg state is $nD_{5/2}$ $(m_j = 5/2)$ and (a,c,d) $n = 35$, (c,d,f) $n = 45$. (a,b) Show the density distribution $n(\mathbf{k})$. (c,d) Show the difference between the dressed ground state and that of non-interacting Fermi gas $n(\mathbf{k}) - n_0(\mathbf{k})$. (e,f) Show the order parameter.

model. This allows us to use $\alpha = k'_F(0)/k'_F(\pi/2)$ as the aspect ratio which is compared with the variance.

Dressing to $n = 35$ and $n = 45$ states does not change the maximal interaction strength, as it is determined by Ω and δ. The anisotropic shapes of the interaction potentials are also similar, which can be found in Fig. 7.2(c). The difference mainly lies on the interaction length. We define R_m as the largest blockade radius in all directions, such that $R_m := \max\left[\sqrt[6]{-C_6(\theta)/(2\delta)}\right]$. Then $R_m = 1.47\ \mu$m for $n = 35$, and $R_m = 2.34\ \mu$m for $n = 45$.

When R_m is small, the deformation appears to be elliptical, and the most deformed points apply to $\theta_{\mathbf{k}} = 0$ or π. By increasing the interaction length, R_m, however, the most deformed point moves to $\theta_{\mathbf{k}} = \pm\pi/4$, which generates non-elliptical deformation. We also find that the smoothness of $n(\mathbf{k})$ is consistent with the order parameter $\Delta(\mathbf{k})$, which suggests that the observation of the Fermi surface also leads to the superconducting order.

7.3.2 Scaling relations of the Fermi surface deformation

In this part, we show the relations of anisotropy and various variables. We evaluated the aspect ratio α and the variance σ under different dressing laser with Rabi frequency Ω and detuning δ, as well as the atom density ρ and the quantum number n of the Rydberg states. The parameters are based on $\Omega = 2\pi \times 10$ MHz, $\delta = -2\pi \times 50$ MHz, $\rho = 1.35 \times 10^{11}$ cm^{-3} ($k_F = 2\ \mu$m^{-2}), $n = 32$, and we sweep each of them with the other three fixed. The results are plotted in Fig.7.4.

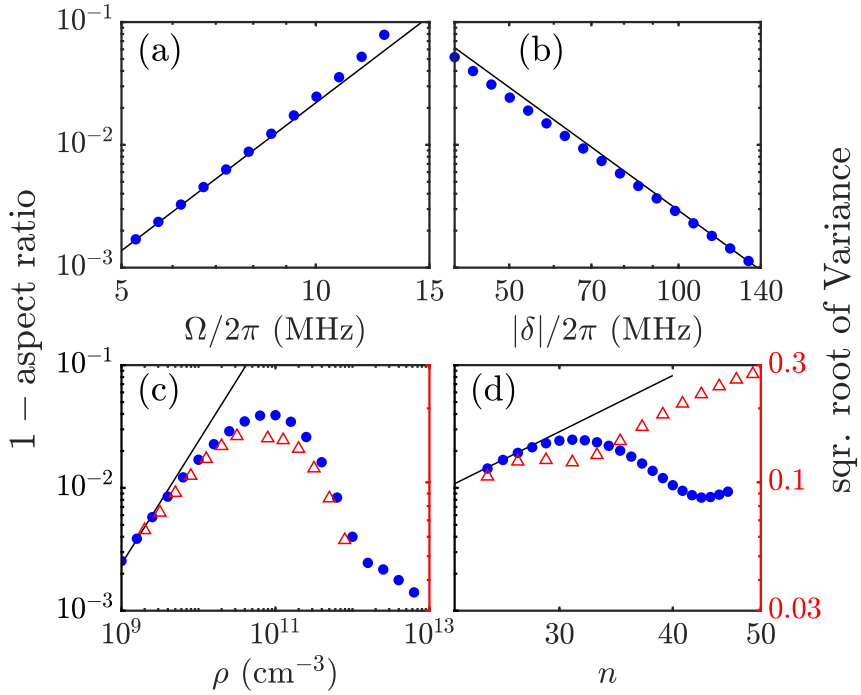


Figure 7.4: Blue dots for aspect ratio $(1-\alpha)$, red triangles for the variance σ. (a) $k_F = 2\ \mu$m^{-1}, $|\delta| = 2\pi \times 50$ MHz, $n = 32$. The black line is fitted with $\sim \Omega^4$. (b) $\Omega = 2\pi \times 10$ MHz, $k_F = 2\ \mu$m^{-1}, $n = 32$, $\delta < 0$. The black line is fitted with $\sim |\delta|^{-10/3}$ (c) $|\delta| = 2\pi \times 50$ MHz, $\Omega = 2\pi \times 10$ MHz, $n = 32$. The black line is fitted with $\sim \rho$. (d) $|\delta| = 2\pi \times 50$ MHz, $\Omega = 2\pi \times 10$ MHz, $k_F = 2\ \mu$m^{-1}. The black line is fitted with $\sim n^{11/3}$.

We found that $1-\alpha$ and σ show power-law scalings in the weak coupling condition ($\Omega \ll |\delta|$), dilute limit ($k_F R_m \ll 1$), and relatively short-range regime determined by small n. According to our calculation, we fit $1-\alpha$ with other parameters such that $1-\alpha \sim \Omega^4 \sim |\delta|^{-10/3} \sim \rho \sim n^{11/3}$. The exponents can be partly understood from the perturbation scope [179]. The relative change of the Fermi vector is approximately

$$\frac{\Delta k_F}{k_F} = \frac{1}{2E_F} \int \frac{\mathrm{d}^3\mathbf{k}'}{(2\pi)^3} \tilde{V}(\mathbf{k}_F - \mathbf{k}') n_0(\mathbf{k}'), \tag{7.7}$$

where $\tilde{V}(\mathbf{k})$ is the Fourier transform of RDI. Since the strength of RDI is proportional to Ω_4/δ^3, we expect $1-\alpha \sim \Omega^4$. However, the other three exponents are not very obvious, and requires the expansion of the convolution in Eq. (7.7).

The standard variance σ has similar behaviour to $1-\alpha$ when the power-law relations are satisfied. This suggests that the pairing of the fermions is closely related to the Fermi surface deformation. However, as the interaction length is considerable, by dressing to high n Rydberg states [Fig. 7.4(d)], σ deviates $1-\alpha$ dramatically. This is consistent with the data in Fig.7.3, where a quadrupole deformation occurs. Under quadrupole deformation, the change of k_F at $\theta_{\mathbf{k}}=0$ and $\pi/2$ are in the same direction, but the deformation still exists. Thereby, on needs to generalise the definition of α to capture the arbitrary shapes of the deformation.

7.4 Discussions and outlook

In this work, we have applied the conventional HFB approximation to solve the ground state of Rydberg-dressed fermions, and studied the anisotropic density distribution caused by the anisotropic interactions.

The perturbation method to compute the Fermi surface deformation is still ongoing. We would expect to find some scaling functions for generalising the scaling relations to high-order deformations.

Chapter 8

Summary

In this thesis, we discussed four topics about the dynamics and interactions of ultracold atoms. First, the interference of guided BECs leads to the atomic Sagnac interferometer. Second, the non-equilibrium dynamics was studied in an optical lattice with Rydberg-dressing interactions. Third, we show the new prototype of magneto-optical traps for 3D printing technology. Fourth, we explored the ground state of Rydberg-dressed fermions from the perspective of Fermi surface deformation.

In Chapter 4, we studied the dynamics of atomic Sagnac interferometer under mean-field approximation. The performance of the interferometer has been evaluated using the dynamical scale factor. Based on the analytical solutions to the non-interacting and isotropic trapping case, we employed Bernstein polynomial function for the driving field to achieve the maximal sensitivities at moderate interrogation times. With the numerical simulations of interacting cases using the Gross-Pitaevskii equation, we verified the optimisation is robust for various configurations. We also changed the isotropy of intra- and inter-state interactions strength, and found that the inter-state interaction is the principal cause of the reduction of the sensitivity. Furthermore, the symmetric trap behaves better than the asymmetric trap.

Our study has so far, focused on the ideal case. The number of the atoms are equal for both hyperfine states, the confinement of the two components is the same, and no thermal fluctuation is considered. The future theoretical study may be in demand with further consideration of the particle number and phase fluctuation. As for experiments, the engineering of stable traps based on atom chips is also of great importance.

In Chapter 5, we explored the non-equilibrium dynamics of quenched extended Bose-Hubbard model with Rydberg-dressing. The phase diagrams have been presented including superfluid, supersolid, Mott-insulator and density waves. The emergence of the supersolid and density waves has been implemented with the roton instability. We found that, by quenching the hopping parameter, the evolution from a Mott-insulator state experiences a universal regime at the early stage following the Kibble-Zurek mechanism. The long-term evolution is affected by the long-range interaction, and the density struc-

ture is characterised by the interaction length. The correlation of the system can be measured by time-of-flight interference, which manifests the quantum state and can be realised in experiment.

In this work, we have quenched the hopping parameter by reducing the lattice depth. Another interesting topic is to explore the adiabatic or abrupt quench of long-range interactions. This can be realised experimentally by tuning the Rydberg-dressing laser. Moreover, the initial states chosen to be superfluid or half-filled Mott-insulator (density wave) may lead to different dynamics which is so far unexplored. Apart from the correlation, the entanglement and entropy have been studied in many other systems, but their connection to Rydberg-dressed interactions needs further study.

In Chapter 6, we presented three designs of magneto-optical traps. They can be realised by 3D printing technology, and one of them has already been printed and tested. In theory, we simulated the electromagnetic field generated by the devices. They all satisfy the demand for atom trapping and cooling. The AC simulation also predicts that the new designs may have better performance for fast time-response and high-frequency experiments.

However, the compact apparatus of ultracold atoms is a systematic project, where our designs only consist part of that. The further optimisation for a particular use is needed if the device is adapted to, e.g., atomic clock or interferometers. The complete roadmap of the 3D printed quantum device also involves the vacuum chamber, antenna and electronics. It is critical, and yet challenging, to synthesise different parts as a whole for the next-generation quantum sensors.

In Chapter 7, we have explored the anisotropic Fermi surface deformation of Rydberg-dressed fermions. The shape deformation and pairing have been worked out and result in the power-law scaling relations with the parameters of the laser field, density of atoms and principal quantum number of Rydberg states.

It will be shown in our following work to explain the scaling relations using perturbation theory. However, it is also important to understand the elementary excitations in the Rydberg-dressed systems. Our current study has been focused on the homogeneous atom gas, but density modulation is expected to occur with strongly repulsive interactions. Our future work may extend to the optical lattice, and find out more phases associated with anisotropy.

Appendix A

Atomic Sagnac Interferometer

In this section, we will show three things. First, the rotation transformation of the Hamiltonian, which results in Eq. 4.22 for 1D and Eq. 4.27 for 2D case. Second, the derivation of the equations of motion in the coherent state basis. For 1D case, we achieve Eq. 4.23 and, in 2D case, we have Eq. 4.28. Third, the solutions to the E.O.M.s by integral.

To begin with, we need to introduce two results in linear algebra. First, we consider two matrices A, B, and

$$e^{A}Be^{-A} = B + [A,B] + \frac{1}{2!}[A,[A,B]] + \frac{1}{3!}[A,[A,[A,B]]] + \cdots . \tag{A.1}$$

The second, also known as the Baker-Campbell-Hausdorff formula, shows

$$e^{A}e^{B} = \exp\left(A + B + \frac{1}{2}[A,B] + \frac{1}{12}[A,[A,B]] - \frac{1}{12}[B,[A,B]] + \cdots\right). \tag{A.2}$$

If $[A,[A,B]] = [B,[A,B]] = 0$, we can truncate the right hand side at $[A,B]$.

A.1 1D case

For 1D case, the Hamiltonian in the laboratory frame is

$$\hat{H}_{1,2} = -\frac{1}{2R_p^2}\frac{\partial^2}{\partial\theta^2} + \frac{R_p^2}{2}\left[\theta - \Theta_{1,2}(t)\right]^2 . \tag{A.3}$$

To transform into rotating frame, we choose $\hat{U}_{1,2}(t) = \exp\left[\omega_s t\frac{\partial}{\partial\theta}\right]$, and the rotated Hamiltonian is

$$\hat{H}'_{1,2}(t) = \hat{U}_{1,2}(t)\hat{H}_{1,2}(t)\hat{U}^{\dagger}_{1,2}(t) + \mathrm{i}\left(\frac{\partial}{\partial t}\hat{U}_{1,2}(t)\right)\hat{U}^{\dagger}_{1,2}(t). \tag{A.4}$$

Using Eq. A.1, we find the first two terms are

$$\left[\omega_s t\frac{\partial}{\partial\theta},\hat{H}_{1,2}\right]=\frac{R_p^2}{2}\omega_s t\left[\frac{\partial}{\partial\theta},(\theta-\Theta_{1,2})^2\right]=R_p^2\omega_s t\,(\theta-\Theta_{1,2}),$$
$$\left[\omega_s t\frac{\partial}{\partial\theta},\left[\omega_s t\frac{\partial}{\partial\theta},\hat{H}_{1,2}\right]\right]=\left[\omega_s t\frac{\partial}{\partial\theta},R_p^2\omega_s t\,(\theta-\Theta_{1,2})\right]=R_p^2\omega_s^2 t^2.$$

The higher orders are equal to zero. We also find that $\mathrm{i}\left(\frac{\partial}{\partial t}\hat{U}_{1,2}(t)\right)\hat{U}_{1,2}^{\dagger}(t)=\mathrm{i}\omega_s\frac{\partial}{\partial\theta}$. Finally, the rotated Hamiltonian yields

$$\hat{H}'_{1,2}=-\frac{1}{2R_p^2}\frac{\partial^2}{\partial\theta^2}+\frac{R_p^2}{2}\theta^2\mp R_p^2\left[\theta_p(t)-\pi\right]\theta+\frac{1}{2}\left[\theta_p(t)-\pi\right]^2+\mathrm{i}\omega_s\frac{\partial}{\partial\theta}. \tag{A.5}$$

Using the creation and annihilation operators, we finally get Eq. 4.22,

$$\hat{H}'_{1,2}=\hat{a}^{\dagger}\hat{a}+\lambda_{1,2}(t)\hat{a}^{\dagger}+\lambda_{1,2}^{*}(t)\hat{a}+\xi(t), \tag{A.6}$$

where

$$\lambda(t)=\frac{R_p}{\sqrt{2}}\left[\mp(\theta_p(t)-\pi)-i\omega_s\right],$$
$$\xi(t)=\frac{1}{2}R_p^2\left[\theta_p(t)-\pi\right]^2+\frac{1}{2}.$$

The Hamiltonian only consists of the linear term $\hat{a}$, $\hat{a}^{\dagger}$, and the number term $\hat{a}^{\dagger}\hat{a}$, so the evolution of a coherent state will stay coherent. We consider a small time evolution during $\mathrm{d}t$, such that

$$\begin{aligned}
e^{-\mathrm{i}\mathrm{d}t\hat{H}'_{1,2}(t)}&=e^{-\mathrm{i}\mathrm{d}t\hat{a}^{\dagger}\hat{a}+\left[-\mathrm{i}\lambda_{1,2}(t)\mathrm{d}t\hat{a}^{\dagger}-\mathrm{H.c.}\right]-\mathrm{i}\mathrm{d}t\xi(t)}\\
&=e^{-\mathrm{i}\mathrm{d}t\hat{a}^{\dagger}\hat{a}}e^{\left[-\mathrm{i}\lambda_{1,2}(t)\mathrm{d}t\hat{a}^{\dagger}-\mathrm{H.c.}\right]}e^{-\mathrm{i}\mathrm{d}t^2\left(\left[\hat{a}^{\dagger}\hat{a},\lambda_{1,2}(t)\hat{a}^{\dagger}-\mathrm{H.c.}\right]\right)}e^{-\mathrm{i}\mathrm{d}t\xi(t)}\\
&=\hat{R}\left(-\mathrm{i}\mathrm{d}t\right)\hat{D}\left(-\mathrm{i}\lambda_{1,2}(t)\mathrm{d}t\right)e^{\mathcal{O}(\mathrm{d}t^2)}e^{-\mathrm{i}\mathrm{d}t\xi(t)}\\
&\approx\hat{R}\left(-\mathrm{i}\mathrm{d}t\right)\hat{D}\left(-\mathrm{i}\lambda_{1,2}(t)\mathrm{d}t\right)e^{-\mathrm{i}\mathrm{d}t\xi(t)}.
\end{aligned} \tag{A.7}$$

Here $\hat{R}$ is the rotation operator, $\hat{D}$ is the displacement operator. They both act on the coherent state $|\alpha\rangle$ as

$$\hat{R}(\beta)|\alpha\rangle=\left|\alpha e^{\beta}\right\rangle, \tag{A.8}$$
$$\hat{D}(\beta)|\alpha\rangle=e^{\frac{1}{2}(\alpha\beta^*-\alpha^*\beta)}|\alpha+\beta\rangle. \tag{A.9}$$

Therefore,as aforementioned, a coherent state or vacuum state will always stay coherent. The quantum state in the coherent phase space will rotate around the origin at the frequency $\omega_r\equiv 1$, and displaced by $\lambda(t)$. $\xi(t)$ offers a shift of the global phase. Presuming that at time t, the wavefunction is $\psi'_{1,2}(t)=e^{\mathrm{i}\phi_{1,2}(t)}\left|\alpha_{1,2}(t)\right\rangle$, the wavefunction

of next time step $t+\mathrm{d}t$ will be

$$\begin{aligned}
&\psi'_{1,2}(t+\mathrm{d}t) = \hat{R}(-\mathrm{i}\mathrm{d}t)\hat{D}(-\mathrm{i}\lambda_{1,2}(t)\mathrm{d}t)\, e^{-\mathrm{i}\xi(t)\mathrm{d}t} e^{\mathrm{i}\phi_{1,2}(t)} \left|\alpha_{1,2}(t)\right\rangle \\
&= e^{\mathrm{i}\phi_{1,2}(t)-\mathrm{i}\xi(t)\mathrm{d}t}\hat{R}(-\mathrm{i}\mathrm{d}t)\, e^{\mathrm{i}\mathrm{Im}\left[\mathrm{i}\alpha_{1,2}(t)\lambda^*_{1,2}(t)\mathrm{d}t\right]} \left|\alpha_{1,2}(t)-\mathrm{i}\lambda_{1,2}(t)\mathrm{d}t\right\rangle \\
&= e^{\mathrm{i}\phi_{1,2}(t)-\mathrm{i}\xi(t)\mathrm{d}t+\mathrm{i}\mathrm{Re}\left[\alpha_{1,2}(t)\lambda^*_{1,2}(t)\mathrm{d}t\right]} \left|(\alpha_{1,2}(t)-\mathrm{i}\lambda_{1,2}(t)\mathrm{d}t)\, e^{-\mathrm{i}\mathrm{d}t}\right\rangle \\
&= e^{\mathrm{i}\phi_{1,2}(t)-\mathrm{i}\xi(t)\mathrm{d}t+\mathrm{i}\mathrm{Re}\left[\alpha_{1,2}(t)\lambda^*_{1,2}(t)\mathrm{d}t\right]} \left|\alpha_{1,2}(t)-\mathrm{i}\alpha_{1,2}(t)\mathrm{d}t-\mathrm{i}\lambda_{1,2}(t)\mathrm{d}t+\mathcal{O}(\mathrm{d}t^2)\right\rangle .
\end{aligned}$$

Then we can find the E.O.M.s of $\alpha_{1,2}(t)$ and $\phi_{1,2}(t)$ which result in Eq. 4.23,

$$\frac{\mathrm{d}}{\mathrm{d}t}\alpha_{1,2}(t) = -\mathrm{i}\alpha_{1,2}(t)-\mathrm{i}\lambda_{1,2}(t), \tag{A.10}$$

$$\frac{\mathrm{d}}{\mathrm{d}t}\phi_{1,2}(t) = \xi(t)+\mathrm{Re}\left[\alpha_{1,2}(t)\lambda^*_{1,2}(t)\right]. \tag{A.11}$$

The initial states are

$$\alpha_{1,2}(0) = -\lambda_{1,2}(0) = \frac{R_p}{\sqrt{2}}(\mp\pi+\mathrm{i}\omega_s). \tag{A.12}$$

The phase $\phi_{1,2}(0)$ is arbitrary and can be set to be zero. The real parts of $\alpha_{1,2}(0)$ denote the initial positions $\sim\pm\pi$, and the imaginary parts denote the initial speed $\sim\mathrm{i}\omega_s$. At $t=T$, the two wave packets are expected to meet about the origin. $\alpha_{1,2}(t)$ and $\phi_{1,2}(t)$ can be evaluated by integration

$$\begin{aligned}
\alpha_{1,2}(t) &= e^{-\mathrm{i}t}\left[-\lambda_{1,2}(0)-\mathrm{i}\int_0^t \lambda_{1,2}(t')e^{\mathrm{i}t'}\mathrm{d}t'\right] \\
&= \sqrt{2}R_p(\mp\pi+\mathrm{i}\omega_s)e^{-\mathrm{i}t}+\frac{R_p}{\sqrt{2}}[\mp\theta_p(t)\pm\pi-\mathrm{i}\omega_s]\pm\mathrm{i}\frac{R_p}{\sqrt{2}}\int_0^t \omega_p(t')e^{\mathrm{i}(t'-t)}\mathrm{d}t',
\end{aligned} \tag{A.13}$$

$$\phi_{1,2}(t) = \int_0^t \xi(t')\mathrm{d}t'+\int_0^t \mathrm{Re}\left[\alpha_{1,2}(t')\lambda^*_{1,2}(t')\right]\mathrm{d}t'. \tag{A.14}$$

A.2 2D case

The 2D case is similar. The Hamiltonian before rotation transformation is

$$\hat{H}_{1,2} = -\frac{1}{2}\left(\frac{\partial^2}{\partial x^2}+\frac{\partial^2}{\partial y^2}\right)+\frac{1}{2}\left[x-R_p\cos\Theta_{1,2}(t)\right]^2+\frac{1}{2}\left[y-R_p\sin\Theta_{1,2}(t)\right]^2. \tag{A.15}$$

Transforming with the unitary operator $\hat{U}_{1,2}(t)=\exp\left[\mathrm{i}\omega_s t\hat{L}_z\right]=\exp\left[\omega_s t\left(x\frac{\partial}{\partial y}-y\frac{\partial}{\partial x}\right)\right]$, one have

$$\begin{aligned}
&\left[\omega_s t\left(x\frac{\partial}{\partial y}-y\frac{\partial}{\partial x}\right), \frac{1}{2}\left(x-R_p\cos\Theta_{1,2}(t)\right)^2+\frac{1}{2}\left(y-R_p\sin\Theta_{1,2}(t)\right)^2\right] \\
&= \omega_s t\left(\left[x\frac{\partial}{\partial y}, -R_p y\sin\Theta_{1,2}\right]+\left[-y\frac{\partial}{\partial x}, -R_p x\cos\Theta_{1,2}\right]\right)
\end{aligned}$$

$$
\begin{aligned}
&= \omega_s t R_p \left(-x\sin\Theta_{1,2} + y\cos\Theta_{1,2}\right), \\
&\quad \left[\omega_s t\left(x\frac{\partial}{\partial y} - y\frac{\partial}{\partial x}\right), \omega_s t R_p\left(-x\sin\Theta_{1,2} + y\cos\Theta_{1,2}\right)\right] \\
&= \omega_s^2 t^2 R_p\left(\left[x\frac{\partial}{\partial y}, y\cos\Theta_{1,2}\right] + \left[-y\frac{\partial}{\partial x}, -x\sin\Theta_{1,2}\right]\right) \\
&= \omega_s^2 t^2 R_p\left(x\cos\Theta_{1,2} + y\sin\Theta_{1,2}\right), \\
&\quad \left[\omega_s t\left(x\frac{\partial}{\partial y} - y\frac{\partial}{\partial x}\right), \omega_s^2 t^2 R_p\left(x\cos\Theta_{1,2} + y\sin\Theta_{1,2}\right)\right] \\
&= \omega_s^3 t^3 R_p\left(\left[x\frac{\partial}{\partial y}, y\sin\Theta_{1,2}\right] + \left[-y\frac{\partial}{\partial x}, x\cos\Theta_{1,2}\right]\right) \\
&= \omega_s^3 t^3 R_p\left(x\sin\Theta_{1,2} - y\cos\Theta_{1,2}\right), \\
&\quad \cdots .
\end{aligned}
$$

As $\left[\hat{L}_z, \nabla^2\right] = 0$, we have

$$
\begin{aligned}
&\hat{U}_{1,2}\hat{H}_{1,2}\hat{U}_{1,2}^{\dagger} \\
&= -R_p x\sin\Theta_{1,2}\left(\omega_s t - \frac{1}{3!}\omega_s^3 t^3 + \cdots\right) - R_p x\cos\Theta_{1,2}\left(-\frac{1}{2!}\omega_s^2 t^2 + \frac{1}{4!}\omega_s^4 t^4 - \cdots\right) \\
&\quad + R_p y\cos\Theta_{1,2}\left(\omega_s t - \frac{1}{3!}\omega_s^3 t^3 + \cdots\right) - R_p y\sin\Theta_{1,2}\left(-\frac{1}{2!}\omega_s^2 t^2 + \frac{1}{4!}\omega_s^4 t^4 - \cdots\right) \\
&= -R_p x\sin\Theta_{1,2}\sin\omega_s t - R_p x\cos\Theta_{1,2}\left(\cos\omega_s t - 1\right) \\
&\quad + R_p y\cos\Theta_{1,2}\sin\omega_s t - R_p y\sin\Theta_{1,2}\left(\cos\omega_s t - 1\right) \\
&= -R_p x\cos\theta_p(t) \mp R_p y\sin\theta_p(t) + R_p x\cos\Theta_{1,2} + R_p y\sin\Theta_{1,2}.
\end{aligned} \tag{A.16}
$$

And since

$$
\mathrm{i}\left(\frac{\partial}{\partial t}\hat{U}_{1,2}\right)\hat{U}_{1,2}^{\dagger} = \mathrm{i}\omega_s\left(x\frac{\partial}{\partial y} - y\frac{\partial}{\partial x}\right), \tag{A.17}
$$

the transformed Hamiltonian becomes

$$
\begin{aligned}
\hat{H}'_{1,2} = &-\frac{1}{2}\left(\frac{\partial^2}{\partial x^2} + \frac{\partial^2}{\partial y^2}\right) + \frac{1}{2}\left(x^2 + y^2 + R_p^2\right) - R_p x\cos\theta_p(t) \mp R_p y\sin\theta_p(t) \\
&+ \mathrm{i}\omega_s\left(x\frac{\partial}{\partial y} - y\frac{\partial}{\partial x}\right).
\end{aligned} \tag{A.18}
$$

As there are two variables x, y, we need to introduce two sets of creation and annihilation operators such that

$$
\hat{a} = \frac{1}{2}\left(x + \mathrm{i}y + \frac{\partial}{\partial x} + \mathrm{i}\frac{\partial}{\partial y}\right),\ \hat{a}^{\dagger} = \frac{1}{2}\left(x - \mathrm{i}y - \frac{\partial}{\partial x} + \mathrm{i}\frac{\partial}{\partial y}\right),
$$

$$
\hat{b} = \frac{1}{2}\left(x - \mathrm{i}y + \frac{\partial}{\partial x} - \mathrm{i}\frac{\partial}{\partial y}\right),\ \hat{b}^{\dagger} = \frac{1}{2}\left(x + \mathrm{i}y - \frac{\partial}{\partial x} - \mathrm{i}\frac{\partial}{\partial y}\right),
$$

which simplify the Hamiltonian to Eq. 4.27,

$$\hat{H}'_{1,2} = (1+\omega_s)\,\hat{a}^\dagger\hat{a} + (1-\omega_s)\,\hat{b}^\dagger\hat{b} + 1 + \frac{R_p^2}{2} - \frac{R_p}{2}\left(\hat{a}e^{\mp i\theta_p} + \hat{b}e^{\pm i\theta_p} + \text{H.c.}\right). \quad \text{(A.19)}$$

The constant $1+R_p^2/2$ can be eliminated as it only produces the same phase shift to the two components. The wave function is now a product of two coherent states $\psi_{1,2} = e^{i\phi_{1,2}}\left|\alpha_{1,2}\right\rangle \otimes \left|\beta_{1,2}\right\rangle$. Similar to the 1D solution, we also use the rotation and displacement operators to generate the E.O.M.s. Using $|\alpha\rangle$ as an example,

$$\begin{aligned}
&\hat{R}\left(-i\mathrm{d}t\,(1+\omega_s)\right)\hat{D}\left(i\mathrm{d}t\frac{R_p}{2}e^{\pm i\theta_p}\right)\left|\alpha_{1,2}\right\rangle \\
&= \hat{R}\left(-i\mathrm{d}t\,(1+\omega_s)\right)e^{i\mathrm{d}t\frac{R_p}{4}\left(\alpha_{1,2}e^{\mp i\theta_p}+\alpha_{1,2}^* e^{\pm i\theta_p}\right)}\left|\alpha_{1,2}+i\mathrm{d}t\frac{R_p}{2}e^{\pm i\theta_p}\right\rangle \\
&= e^{i\mathrm{d}t\frac{R_p}{2}\mathrm{Re}\left[\alpha_{1,2}e^{\mp i\theta_p}\right]}\left|\left(\alpha_{1,2}+i\mathrm{d}t\frac{R_p}{2}e^{\pm i\theta_p}\right)e^{-i\mathrm{d}t(1+\omega_s)}\right\rangle \\
&\approx e^{i\mathrm{d}t\frac{R_p}{2}\mathrm{Re}\left[\alpha_{1,2}e^{\mp i\theta_p}\right]}\left|\alpha_{1,2}-i\mathrm{d}t\,(1+\omega_s)\,\alpha_{1,2}+i\mathrm{d}t\frac{R_p}{2}e^{\pm i\theta_p}\right\rangle,
\end{aligned}$$

and the evolution of $|\beta\rangle$ is similar. Finally, we get the E.O.M.s as shown in Eq. 4.28,

$$\frac{\mathrm{d}}{\mathrm{d}t}\alpha_{1,2} = -i\,(1+\omega)\,\alpha_{1,2} + i\frac{R_p}{2}e^{\pm i\theta_p}, \quad \text{(A.20)}$$

$$\frac{\mathrm{d}}{\mathrm{d}t}\beta_{1,2} = -i\,(1-\omega)\,\beta_{1,2} + i\frac{R_p}{2}e^{\mp i\theta_p}, \quad \text{(A.21)}$$

$$\frac{\mathrm{d}}{\mathrm{d}t}\phi_{1,2} = \frac{R_p}{2}\mathrm{Re}\left[\alpha_{1,2}e^{\mp i\theta_p} + \beta_{1,2}e^{\pm i\theta_p}\right]. \quad \text{(A.22)}$$

The initial states, letting $\phi_{1,2}=0$, are

$$\alpha_{1,2}(0) = \frac{R_p}{2(1+\omega)}, \quad \text{(A.23)}$$

$$\beta_{1,2}(0) = \frac{R_p}{2(1-\omega)}, \quad \text{(A.24)}$$

which means the initial position $x = R_p/(1-\omega_s^2)$, $y=0$, and momentum $p_x=0$, $p_y = \omega_s R_p/(1-\omega_s^2)$. The centrifugal effect has already been seen by the factor $1/(1-\omega_s^2)$. The dynamical solutions can be achieved by integration similar to the 1D case, which result in

$$\alpha_{1,2}(t) = \frac{R_p}{2(1+\omega_s)}e^{-i(1+\omega_s)t}\left(1+i(1+\omega_s)\int_0^t \mathrm{d}t' e^{\pm i\theta_p(t')}e^{i(1+\omega_s)t'}\right), \quad \text{(A.25)}$$

$$\beta_{1,2}(t) = \frac{R_p}{2(1-\omega_s)}e^{-i(1-\omega_s)t}\left(1+i(1-\omega_s)\int_0^t \mathrm{d}t' e^{\mp i\theta_p(t')}e^{i(1-\omega_s)t'}\right), \quad \text{(A.26)}$$

$$\phi_{1,2}(t) = -\frac{R_p}{2}\mathrm{Re}\left[\int_0^t \mathrm{d}t'\left(e^{\mp i\theta_p(t')}\alpha_{1,2}(t') + e^{\pm i\theta_p(t')}\beta_{1,2}(t')\right)\right]. \quad \text{(A.27)}$$

Appendix B

Quenched Bose-Hubbard Model

B.1 Derivations for the E.O.M. of the coefficients of GWF

The E.O.M. of f_m^i in Eq. 5.6 is derived below. The wave function is factorized to the direct product

$$\Psi = \prod_i^{\otimes} |\psi_i\rangle = \prod_i^{\otimes} \sum_m f_m^i |i,m\rangle . \tag{B.1}$$

Inserting to Schrödinger equation $\imath\frac{\partial}{\partial t}|\Psi\rangle = H|\Psi\rangle$ with the Hamiltonian of Eq. 5.1, one has

$$\begin{aligned}
\imath\sum_i \frac{\partial}{\partial t}|\psi_i\rangle \otimes \prod_{j\neq i}|\psi_j\rangle &= -J\sum_i\sum_{\langle j\rangle_i}\left(\hat{b}_i^\dagger \hat{b}_j + \hat{b}_j^\dagger \hat{b}_i\right)|\Psi\rangle \\
&\quad + \sum_i\left(\frac{U}{2}\hat{n}_i(\hat{n}_i+1) - \mu\hat{n}_i\right)|\Psi\rangle + \sum_{ij} V_{ij}\hat{n}_i\hat{n}_j|\Psi\rangle , \\
\imath\sum_{i,m}\frac{\partial}{\partial t} f_m^i|i,m\rangle \otimes \prod_{j\neq i}|\psi_j\rangle &= -J\sum_{i,\langle j\rangle_i}\left(\hat{b}_i^\dagger \hat{b}_j + \hat{b}_j^\dagger \hat{b}_i\right)\left(\sum_m f_m^i|k,m\rangle\right)\otimes\prod_{k\neq i}|\psi_k\rangle + \\
&\quad + \sum_i\left(\frac{U}{2}\hat{n}_i(\hat{n}_i+1) - \mu\hat{n}_i\right)\left(\sum_m f_m^i|k,m\rangle\right)\otimes\prod_{k\neq i}|\psi_k\rangle \\
&\quad + \sum_{ij} V_{ij}\hat{n}_i\left(\sum_m f_m^i|i,m\rangle\right)\otimes\prod_{k\neq i}\hat{n}_j|\psi_k\rangle , \\
\imath\sum_{i,m}\frac{\partial}{\partial t} f_m^i|i,m\rangle \otimes \prod_{j\neq i}|\psi_j\rangle &= -J\sum_{i,\langle j\rangle_i}\left[\left(\sum_m f_m^i\sqrt{m+1}\,|i,m+1\rangle\right)\otimes b_j|\psi_j\rangle\right. \\
&\quad \left. + \left(\sum_m f_m^i\sqrt{m}\,|i,m-1\rangle\right)\otimes b_j^\dagger|\psi_j\rangle\right]\otimes\prod_{k\neq i,\langle j\rangle_i}|\psi_k\rangle \\
&\quad + \sum_i\sum_m\left(\frac{U}{2}m(m+1) - \mu m\right)\left(f_m^i|k,m\rangle\right)\otimes\prod_{k\neq i}|\psi_k\rangle , \\
&\quad + \sum_{ij} V_{ij}\left[\left(\sum_m m f_m^i|i,m\rangle\right)\otimes\hat{n}_j|\psi_j\rangle\right]\otimes\prod_{k\neq i,j}|\psi_k\rangle .
\end{aligned}$$

The E.O.M. of f_m^i can be achieved by sandwiching the both sides by $\langle i,m| \otimes \Pi_{j\neq i} \langle \psi_j|$

$$\begin{aligned} \mathrm{i}\frac{\partial}{\partial t} f_m^i = &-J\left(\sqrt{m} f_{m-1}^i \sum_{\langle j\rangle_i} \langle \psi_j | \hat{b}_j | \psi_j \rangle + \sqrt{m+1} f_{m+1}^i \sum_{\langle j\rangle_i} \left\langle \psi_j \middle| b_j^\dagger \middle| \psi_j \right\rangle\right) \\ &+ \left(\frac{U}{2} m(m-1) - \mu m + m \sum_j V_{ij} \langle \psi_j | \hat{n}_j | \psi_j \rangle\right) f_m^i, \end{aligned} \tag{B.2}$$

where $\langle \psi_j | \hat{b}_j | \psi_j \rangle = \phi_j$ is the local superfluid order parameter, and $\langle \psi_j | \hat{n}_j | \psi_j \rangle = n_j$ is the occupation on the j-th site. This results in the Eq. 5.6.

B.2 Derivations for correlation functions under GWF

In this section, we show the derivation of the correlation functions in Eq. 5.33 and Eq. 5.35 under the Gutzwiller ansatz. The expectation value of multiple operators $\langle \hat{A}_i \hat{B}_j \rangle$ can be decomposed if $i \neq j$, but cannot if $i = j$. Therefore, we need to consider all of the situations under GWF.

The first-order correlation, for example, only needs to consider two operators as shown in Eq. 5.31. Regardless the Wannier envelope, we have

$$\begin{aligned} n(\mathbf{x}) &= \sum_{i,j} e^{\mathrm{i}\mathbf{k}\cdot(\mathbf{r}_i - \mathbf{r}_j)} \langle \hat{b}_i^\dagger \hat{b}_j \rangle \\ &= \sum_{i,j} e^{\mathrm{i}\mathbf{k}\cdot(\mathbf{r}_i - \mathbf{r}_j)} \langle \hat{b}_i^\dagger \rangle \langle \hat{b}_j \rangle - \sum_i e^{\mathrm{i}\mathbf{k}\cdot(\mathbf{r}_i - \mathbf{r}_i)} \langle \hat{b}_i^\dagger \rangle \langle \hat{b}_i \rangle + \sum_i e^{\mathrm{i}\mathbf{k}\cdot(\mathbf{r}_i - \mathbf{r}_i)} \langle \hat{b}_i^\dagger \hat{b}_i \rangle \\ &= \sum_{i,j} e^{\mathrm{i}\mathbf{k}\cdot(\mathbf{r}_i - \mathbf{r}_j)} \phi_i^* \phi_j - \sum_i |\phi_i|^2 + \sum_i n_i \\ &= \left| \sum_i e^{-\mathrm{i}\mathbf{k}\cdot\mathbf{r}_i} \phi_i \right|^2 - \sum_i |\phi_i|^2 + \sum_i n_i. \end{aligned}$$

The first term is the discrete Fourier transformation of ϕ_i, which can be written as Eq. 5.33.

The covariance is more complicated. As defined in Eq. 5.35, we need to calculate

$$C(\mathbf{k}, \mathbf{k}+\mathbf{q}) = \sum_{i,j,m,n} e^{\mathrm{i}\mathbf{k}\cdot(\mathbf{r}_i - \mathbf{r}_j) + \mathrm{i}(\mathbf{k}+\mathbf{q})\cdot(\mathbf{r}_m - \mathbf{r}_n)} \left(\langle \hat{b}_i^\dagger \hat{b}_j \hat{b}_m^\dagger \hat{b}_n \rangle - \langle \hat{b}_i^\dagger \hat{b}_j \rangle \langle \hat{b}_m^\dagger \hat{b}_n \rangle \right). \tag{B.3}$$

Let $N = \sum_i n_i$ and $\eta_i = \langle \hat{b}_i \hat{b}_i \rangle$, $\gamma_i = \langle \hat{b}_i^\dagger \hat{b}_i \hat{b}_i \rangle$. Here, we show the segregation of the four-operator terms as following

$$\begin{aligned} &i = j = m = n \Rightarrow \sum_i \langle \hat{b}_i^\dagger \hat{b}_i \hat{b}_i^\dagger \hat{b}_i \rangle = \sum_i \langle \hat{n}_i^2 \rangle \\ &i \neq j = m = n \Rightarrow \sum_{i\neq j} e^{\mathrm{i}\mathbf{k}\cdot(\mathbf{r}_i - \mathbf{r}_j)} \phi_i^* (\gamma_j + \phi_j) \end{aligned}$$

$$= MS(\phi^*;\mathbf{k})S^{-1}(\gamma+\phi;\mathbf{k}) - \sum_i \phi_i^*\gamma_i - \sum_i |\phi_i|^2$$

$$j\neq i=m=n \Rightarrow \sum_{i\neq j} e^{\mathrm{i}\mathbf{k}\cdot(\mathbf{r}_i-\mathbf{r}_j)}\gamma_i^*\phi_j = MS(\gamma^*;\mathbf{k})S^{-1}(\phi;\mathbf{k}) - \sum_i \phi_i\gamma_i^*$$

$$m\neq i=j=n \Rightarrow \sum_{i\neq j} e^{i(\mathbf{k}+\mathbf{q})\cdot(\mathbf{r}_i-\mathbf{r}_j)}\phi_i^*\gamma_j = MS(\phi^*;\mathbf{k}+\mathbf{q})S^{-1}(\gamma;\mathbf{k}+\mathbf{q}) - \sum_i \phi_i^*\gamma_i$$

$$n\neq i=j=m \Rightarrow \sum_{i\neq j} e^{i(\mathbf{k}+\mathbf{q})\cdot(\mathbf{r}_i-\mathbf{r}_j)}(\gamma_i^*+\phi_i^*)\phi_j$$

$$= MS(\gamma^*+\phi^*;\mathbf{k}+\mathbf{q})S^{-1}(\phi;\mathbf{k}+\mathbf{q}) - \sum_i \phi_i\gamma_i^* - \sum_i |\phi_i|^2$$

$$i=j\neq m=n \Rightarrow \sum_{i\neq j}\langle \hat{b}_i^\dagger\hat{b}_i\rangle\langle \hat{b}_j^\dagger\hat{b}_j\rangle = N^2 - \sum_i n_i^2$$

$$i=m\neq j=n \Rightarrow \sum_{i\neq j} e^{i(2\mathbf{k}+\mathbf{q})\cdot(\mathbf{r}_i-\mathbf{r}_j)}\langle \hat{b}_i^\dagger\hat{b}_i^\dagger\rangle\langle \hat{b}_j\hat{b}_j\rangle$$

$$= MS(\eta^*;2\mathbf{k}+\mathbf{q})S^{-1}(\eta;2\mathbf{k}+\mathbf{q}) - \sum_i |\eta_i|^2$$

$$i=n\neq j=m \Rightarrow \sum_{i\neq j} e^{i\mathbf{q}\cdot(\mathbf{r}_i-\mathbf{r}_j)}\langle \hat{b}_i\hat{b}_i^\dagger\rangle\langle \hat{b}_j^\dagger\hat{b}_j\rangle$$

$$= M\left(S(n;\mathbf{q})S^{-1}(n;\mathbf{q}) + F(\mathbf{q})S^{-1}(n;\mathbf{q})\right) - \sum_i \left(n_i^2+n_i\right)$$

$$i=j\neq m\neq n \Rightarrow \sum_{i\neq j\neq m} e^{i(\mathbf{k}+\mathbf{q})\cdot(\mathbf{r}_i-\mathbf{r}_j)}n_m\phi_i^*\phi_j$$

$$= MNS(\phi^*;\mathbf{k}+\mathbf{q})S^{-1}(\phi;\mathbf{k}+\mathbf{q}) - N\sum_i |\phi_i|^2 + 2\sum_i n_i|\phi_i|^2$$

$$- 2M\mathrm{Re}\left[S(\phi^*;\mathbf{k}+\mathbf{q})S^{-1}(n\phi;\mathbf{k}+\mathbf{q})\right]$$

$$m=n\neq i\neq j \Rightarrow \sum_{i\neq j\neq m} e^{\mathrm{i}\mathbf{k}\cdot(\mathbf{r}_i-\mathbf{r}_j)}n_m\phi_i^*\phi_j$$

$$= MNS(\phi^*;\mathbf{k})S^{-1}(\phi;\mathbf{k}) - 2M\mathrm{Re}\left[S(\phi^*;\mathbf{k})S^{-1}(n\phi;\mathbf{k})\right]$$

$$- N\sum_i |\phi_i|^2 + 2\sum_i n_i|\phi_i|^2$$

$$i=m\neq j\neq n \Rightarrow \sum_{i\neq j\neq m} e^{i(2\mathbf{k}+\mathbf{q})\cdot\mathbf{r}_m - \mathrm{i}\mathbf{k}\cdot\mathbf{r}_i - i(\mathbf{k}+\mathbf{q})\cdot\mathbf{r}_j}\eta_m^*\phi_i\phi_j$$

$$= M^{3/2}S(\eta^*;2\mathbf{k}+\mathbf{q})S^{-1}(\phi;\mathbf{k})S^{-1}(\phi;\mathbf{k}+\mathbf{q}) + 2\sum_i \eta_i^*\phi_i^2$$

$$- M\Big[S(\eta^*;2\mathbf{k}+\mathbf{q})S^{-1}(\phi^2;2\mathbf{k}+\mathbf{q}) + S(\eta^*\phi;\mathbf{k})S^{-1}(\phi;\mathbf{k})$$

$$+ S(\eta^*\phi;\mathbf{k}+\mathbf{q})S^{-1}(\phi;\mathbf{k}+\mathbf{q})\Big]$$

$$j=n\neq i\neq m \Rightarrow \sum_{i\neq j\neq m} e^{-i(2\mathbf{k}+\mathbf{q})\cdot\mathbf{r}_m + \mathrm{i}\mathbf{k}\cdot\mathbf{r}_i + i(\mathbf{k}+\mathbf{q})\cdot\mathbf{r}_j}\eta_m\phi_i^*\phi_j^*$$

$$= (i=m\neq j\neq n)^*$$

$$i=n\neq j\neq m \Rightarrow \sum_{i\neq j\neq m} e^{-i\mathbf{q}\cdot\mathbf{r}_m - \mathrm{i}\mathbf{k}\cdot\mathbf{r}_i + i(\mathbf{k}+\mathbf{q})\cdot\mathbf{r}_j}n_m\phi_i\phi_j^*$$

$$
\begin{aligned}
&= M^{3/2} S(\phi^*;\mathbf{k}+\mathbf{q}) S^{-1}(n;\mathbf{q}) S^{-1}(\phi;\mathbf{k}) + 2\sum_i n_i |\phi_i|^2 - \\
&\quad - M\Big[S(|\phi|^2;\mathbf{q}) S^{-1}(n;\mathbf{q}) + S(\phi^*;\mathbf{k}+\mathbf{q}) S^{-1}(n\phi;\mathbf{k}+\mathbf{q}) \\
&\qquad + S(n\phi^*;\mathbf{k}) S^{-1}(\phi;\mathbf{k}) \Big] \\
j = m \neq i \neq n \Rightarrow & \sum_{i\neq j\neq m} e^{i\mathbf{q}\cdot\mathbf{r}_m + \mathbf{i}\mathbf{k}\cdot\mathbf{r}_i - i(\mathbf{k}+\mathbf{q})\cdot\mathbf{r}_j} (n_m+1)\phi_i^*\phi_j \\
&= (i=n\neq j\neq m)^* + M^{3/2} F(\mathbf{q}) S(\phi^*;\mathbf{k}) S^{-1}(\phi;\mathbf{k}+\mathbf{q}) + 2\sum_i |\phi_i|^2 \\
&\quad - M\Big[F(\mathbf{q}) S^{-1}(|\phi|^2;\mathbf{q}) + S(\phi^*;\mathbf{k}) S^{-1}(\phi;\mathbf{k}) \\
&\qquad + S(\phi^*;\mathbf{k}+\mathbf{q}) S^{-1}(\phi;\mathbf{k}+\mathbf{q}) \Big] \\
i \neq j \neq m \neq n \Rightarrow & \sum_{i\neq j\neq m\neq n} e^{i\mathbf{k}\cdot(\mathbf{r}_i-\mathbf{r}_j) + i(\mathbf{k}+\mathbf{q})\cdot(\mathbf{r}_m-\mathbf{r}_n)} \phi_i^*\phi_j\phi_m^*\phi_n \\
&= \left(M S(\phi^*;\mathbf{k}) S^{-1}(\phi;\mathbf{k}) - \sum_i |\phi_i|^2 \right) \times \\
&\quad \left(M S(\phi^*;\mathbf{k}+\mathbf{q}) S^{-1}(\phi;\mathbf{k}+\mathbf{q}) - \sum_i |\phi_i|^2 \right) - 6\sum_i |\phi_i|^4 \\
&\quad - 2M^{3/2}\mathrm{Re}\Big[S(\phi^*;\mathbf{k}) S(|\phi|^2;\mathbf{q}) S^{-1}(\phi;\mathbf{k}+\mathbf{q}) \\
&\qquad + S(\phi^*;\mathbf{k}) S(\phi^*;\mathbf{k}+\mathbf{q}) S^{-1}(\phi^2;2\mathbf{k}+\mathbf{q}) \Big] \\
&\quad + 4M\mathrm{Re}\left[S(\phi^*;\mathbf{k}) S^{-1}(|\phi|^2\phi;\mathbf{k}) + S(\phi^*;\mathbf{k}+\mathbf{q}) S^{-1}(|\phi|^2\phi;\mathbf{k}+\mathbf{q}) \right] \\
&\quad + M\left[S(|\phi|^2;\mathbf{q}) S^{-1}(|\phi|^2;\mathbf{q}) + S(\phi^{*2};2\mathbf{k}+\mathbf{q}) S^{-1}(\phi^2;2\mathbf{k}+\mathbf{q}) \right]
\end{aligned}
$$

The rest two-operator term shows

$$
\begin{aligned}
&\sum_{i,j} e^{\mathbf{i}\mathbf{k}\cdot(\mathbf{r}_i-\mathbf{r}_j)} \langle \hat{b}_i^\dagger \hat{b}_j \rangle \sum_{i,j} e^{i(\mathbf{k}+\mathbf{q})\cdot(\mathbf{r}_i-\mathbf{r}_j)} \langle \hat{b}_i^\dagger \hat{b}_j \rangle \\
&= \Bigg[\left(M S(\phi^*;\mathbf{k}) S^{-1}(\phi;\mathbf{k}) - \sum_i |\phi_i|^2 \right) \left(M S(\phi^*;\mathbf{k}+\mathbf{q}) S^{-1}(\phi;\mathbf{k}+\mathbf{q}) - \sum_i |\phi_i|^2 \right) \\
&\quad + MNS(\phi^*;\mathbf{k}) S^{-1}(\phi;\mathbf{k}) + MNS(\phi^*;\mathbf{k}+\mathbf{q}) S^{-1}(\phi;\mathbf{k}+\mathbf{q}) - 2N\sum_i |\phi_i|^2 + N^2 \Bigg].
\end{aligned}
\tag{B.4}
$$

Therefore, the covariance shows

$$
\begin{aligned}
C(\mathbf{k},\mathbf{k}+\mathbf{q}) = \sum_i \Big(& 8n_i|\phi_i|^2 - 2n_i^2 - n_i - |\eta_i|^2 + \langle \hat{n}_i \hat{n}_i \rangle - 6|\phi_i|^4 + 4\mathrm{Re}\left[\eta^* \phi_i^2 - \gamma_i^* \phi_i \right] \Big) \\
& + M\Bigg(\Big| S(n-|\phi|^2;\mathbf{q}) \Big|^2 + F(\mathbf{q}) S(n-|\phi|^2;\mathbf{q}) + \Big| S(\eta^* - \phi^{*2};2\mathbf{k}+\mathbf{q}) \Big|^2
\end{aligned}
$$

$$
\begin{aligned}
&\quad + 2\chi(\phi^*;\gamma-\eta\phi^*) - 4\chi(\phi^*;(n-|\phi|^2)\phi)\Big) \\
&+ M^{3/2}F(\mathbf{q})S(\phi^*;\mathbf{k})S^{-1}(\phi;\mathbf{k}+\mathbf{q}) \\
&+ 2M^{3/2}\mathrm{Re}\Big[S(\eta^*-\phi^{*2};2\mathbf{k}+\mathbf{q})S^{-1}(\phi;\mathbf{k})S^{-1}(\phi;\mathbf{k}+\mathbf{q}) \\
&\qquad + S(\phi^*;\mathbf{k}+\mathbf{q})S^{-1}(\phi;\mathbf{k})S^{-1}(n-|\phi|^2;\mathbf{q})\Big]. \qquad \text{(B.5)}
\end{aligned}
$$

For simplicity, $\chi(A,B) = \mathrm{Re}\left[S(A;\mathbf{k})S^{-1}(B;\mathbf{k}) + S(A;\mathbf{k}+\mathbf{q})S^{-1}(B;\mathbf{k}+\mathbf{q})\right]$.
In Mott insulator regime, $\phi = 0$, $\eta = 0$, $\gamma = 0$. The covariance is reduced to

$$
C_{\mathrm{Mott}}(\mathbf{k},\mathbf{k}+\mathbf{q}) \sim \sum_i \left(\langle \hat{n}_i^2\rangle - n_i - 2n_i^2\right) + M\left|S(n;\mathbf{q})\right|^2 + MF(\mathbf{q})S(n;\mathbf{q}). \qquad \text{(B.6)}
$$

Appendix C

Hartree-Fock-Bogoliubov Approximation

In this section, we will show the Hartree-Fock-Bogoliubiv (HFB) approximation to simplify the two-body Hamiltonian in Eq. 7.1 to HFB Hamiltonian in Eq. 7.2.
First of all, we need to Fourier transform Eq. 7.1 into the momentum representation. The results read

$$H = \sum_{\mathbf{k}} \left(\frac{\hbar^2 |\mathbf{k}|^2}{2m} + \tilde{V}_{\text{ext}}(\mathbf{k}) - \mu \right) \hat{a}^\dagger_{\mathbf{k}} \hat{a}_{\mathbf{k}} + \sum_{\mathbf{k},\mathbf{k}',\mathbf{q}} \tilde{V}(\mathbf{q}) \hat{a}^\dagger_{\mathbf{k}+\mathbf{q}} \hat{a}^\dagger_{\mathbf{k}'-\mathbf{q}} \hat{a}_{\mathbf{k}'} \hat{a}_{\mathbf{k}}. \tag{C.1}$$

The four-operator term can be simplified using Weiss mean field approximation, such that

$$\begin{aligned} \hat{a}^\dagger_{\mathbf{k}+\mathbf{q}} \hat{a}^\dagger_{\mathbf{k}'-\mathbf{q}} \hat{a}_{\mathbf{k}'} \hat{a}_{\mathbf{k}} \simeq & \langle \hat{a}^\dagger_{\mathbf{k}+\mathbf{q}} \hat{a}_{\mathbf{k}} \rangle \hat{a}^\dagger_{\mathbf{k}'-\mathbf{q}} \hat{a}_{\mathbf{k}'} + \langle \hat{a}^\dagger_{\mathbf{k}'-\mathbf{q}} \hat{a}_{\mathbf{k}'} \rangle \hat{a}^\dagger_{\mathbf{k}+\mathbf{q}} \hat{a}_{\mathbf{k}} && \text{(Hartree)} \\ & - \langle \hat{a}^\dagger_{\mathbf{k}+\mathbf{q}} \hat{a}_{\mathbf{k}'} \rangle \hat{a}^\dagger_{\mathbf{k}'-\mathbf{q}} \hat{a}_{\mathbf{k}} - \langle \hat{a}^\dagger_{\mathbf{k}'-\mathbf{q}} \hat{a}_{\mathbf{k}} \rangle \hat{a}^\dagger_{\mathbf{k}+\mathbf{q}} \hat{a}_{\mathbf{k}'} && \text{(Fock)} \\ & + \langle \hat{a}^\dagger_{\mathbf{k}+\mathbf{q}} \hat{a}^\dagger_{\mathbf{k}'-\mathbf{q}} \rangle \hat{a}_{\mathbf{k}'} \hat{a}_{\mathbf{k}} + \langle \hat{a}_{\mathbf{k}'} \hat{a}_{\mathbf{k}} \rangle \hat{a}^\dagger_{\mathbf{k}+\mathbf{q}} \hat{a}^\dagger_{\mathbf{k}'-\mathbf{q}} && \text{(Bogoliubov)}, \end{aligned} \tag{C.2}$$

The expectation of $\langle \hat{a}^\dagger_{\mathbf{k}} \hat{a}_{\mathbf{k}'} \rangle = n_{\mathbf{k}} \delta_{\mathbf{k}\mathbf{k}'}$, and the superconductor order exists when $\langle \hat{a}_{-\mathbf{k}} \hat{a}_{\mathbf{k}} \rangle \neq 0$. Therefore, the Hartree terms requires $\mathbf{q} = 0$, the Fock term requires $\mathbf{k}+\mathbf{q} = \mathbf{k}'$ and the Bogoliubov term requires $\mathbf{k} = -\mathbf{k}'$. Thus we have the simplified Hamiltonian

$$H = \sum_{\mathbf{k}} \left(\frac{\hbar^2 |\mathbf{k}|^2}{2m} + \tilde{V}_{\text{ext}}(\mathbf{k}) - \mu + U_H + U_F(\mathbf{k}) \right) \hat{a}^\dagger_{\mathbf{k}} \hat{a}_{\mathbf{k}} + {\sum_{\mathbf{k}}}' \left(\Delta(\mathbf{k}) \hat{a}^\dagger_{\mathbf{k}} \hat{a}^\dagger_{-\mathbf{k}} + \Delta^*(\mathbf{k}) \hat{a}_{-\mathbf{k}} \hat{a}_{\mathbf{k}} \right), \tag{C.3}$$

where $\sum'$ is the sum over half of the momentum space to avoid repeating, and

$$U_H = \rho \tilde{V}(0), \tag{C.4a}$$

$$U_F(\mathbf{k}) = -{\sum_{\mathbf{k}'}}' \tilde{V}(\mathbf{k}-\mathbf{k}') \langle \hat{a}^\dagger_{\mathbf{k}'} \hat{a}_{\mathbf{k}'} \rangle, \tag{C.4b}$$

$$\Delta(\mathbf{k}) = {\sum_{\mathbf{k}'}}' \tilde{V}(\mathbf{k}-\mathbf{k}') \langle \hat{a}_{-\mathbf{k}'} \hat{a}_{\mathbf{k}'} \rangle. \tag{C.4c}$$

In our work, we assume the density in real space is homogeneous, $U_H = \text{const.}$, and thereby, the Hartree energy and the external field are absorbed into the chemical potential.

The HFB Hamiltonian can be diagonalised by Bardeen–Cooper–Schrieffer (BCS) theory. It is expected to achieve a new particle $\hat{c}_{\mathbf{k}}$ from the superposition of $\hat{a}_{\mathbf{k}}$ and $\hat{a}^{\dagger}_{-\mathbf{k}}$ such that

$$\hat{c}_{\mathbf{k}} = u_{\mathbf{k}}\hat{a}_{\mathbf{k}} + v_{\mathbf{k}}\hat{a}^{\dagger}_{-\mathbf{k}}, \quad \hat{c}^{\dagger}_{\mathbf{k}} = v^{*}_{\mathbf{k}}\hat{a}_{-\mathbf{k}} + u^{*}_{\mathbf{k}}\hat{a}^{\dagger}_{\mathbf{k}}. \tag{C.5}$$

In order to maintain $\hat{c}_{\mathbf{k}}$ being fermionic, i.e., $\left\{\hat{c}_{\mathbf{k}}, \hat{c}^{\dagger}_{\mathbf{k}}\right\} = 1$, there is a constraint

$$|u_{\mathbf{k}}|^2 + |v_{\mathbf{k}}|^2 = 1. \tag{C.6}$$

We also impose that $u_{\mathbf{k}} = u_{-\mathbf{k}}$, $v_{\mathbf{k}} = -v_{-\mathbf{k}}$. The minus sign comes from the anti-symmetry of the wave function. Substituting the new operator back to the Hamiltonian, one has

$$\begin{aligned} H = &\sum_{\mathbf{k}} \left(\frac{\hbar^2 |\mathbf{k}|^2}{2m} - \mu + U_F(\mathbf{k}) \right) \left(|u_{\mathbf{k}}|^2 \hat{c}^{\dagger}_{\mathbf{k}}\hat{c}_{\mathbf{k}} + |v_{\mathbf{k}}|^2 \hat{c}_{-\mathbf{k}}\hat{c}^{\dagger}_{-\mathbf{k}} - u^{*}_{\mathbf{k}}v^{*}_{\mathbf{k}}\hat{c}_{-\mathbf{k}}\hat{c}_{\mathbf{k}} - u_{\mathbf{k}}v_{\mathbf{k}}\hat{c}^{\dagger}_{\mathbf{k}}\hat{c}^{\dagger}_{-\mathbf{k}} \right) \\ &+ \sum_{\mathbf{k}}{}' \left[\Delta(\mathbf{k}) u_{\mathbf{k}} v^{*}_{\mathbf{k}} - \Delta^{*}(\mathbf{k}) u^{*}_{\mathbf{k}} v_{\mathbf{k}} \right] \left(\hat{c}^{\dagger}_{\mathbf{k}}\hat{c}_{\mathbf{k}} - \hat{c}_{-\mathbf{k}}\hat{c}^{\dagger}_{-\mathbf{k}} \right) \\ &+ \sum_{\mathbf{k}}{}' \left[\Delta(\mathbf{k}) \left({u_{\mathbf{k}}}^2 \hat{c}^{\dagger}_{\mathbf{k}}\hat{c}^{\dagger}_{-\mathbf{k}} - {v^{*}_{\mathbf{k}}}^2 \hat{c}_{-\mathbf{k}}\hat{c}_{\mathbf{k}} \right) - \Delta^{*}(\mathbf{k}) \left({v_{\mathbf{k}}}^2 \hat{c}^{\dagger}_{\mathbf{k}}\hat{c}^{\dagger}_{-\mathbf{k}} - {u^{*}_{\mathbf{k}}}^2 \hat{c}_{-\mathbf{k}}\hat{c}_{\mathbf{k}} \right) \right]. \end{aligned} \tag{C.7}$$

To diagonalise the Hamiltonian, we need to let the coefficients in front of $\hat{c}\hat{c}$ and $\hat{c}^{\dagger}\hat{c}^{\dagger}$ vanish. Therefore, we get

$$2\left(\frac{\hbar^2 |\mathbf{k}|^2}{2m} - \mu + U_F(\mathbf{k}) \right) u_{\mathbf{k}} v_{\mathbf{k}} + \Delta(\mathbf{k}) {u_{\mathbf{k}}}^2 - \Delta^{*}(\mathbf{k}) {v_{\mathbf{k}}}^2 = 0. \tag{C.8}$$

Let $\xi(\mathbf{k}) = \hbar^2 |\mathbf{k}|^2 / (2m) - \mu + U_F(\mathbf{k})$, we can get the solution to $u_{\mathbf{k}}$ and $v_{\mathbf{k}}$

$$|v_{\mathbf{k}}|^2 = \frac{1}{2}\left(1 - \frac{\xi(\mathbf{k})}{\sqrt{\xi(\mathbf{k})^2 + |\Delta(\mathbf{k})|^2}} \right), \quad |u_{\mathbf{k}}|^2 = \frac{1}{2}\left(1 + \frac{\xi(\mathbf{k})}{\sqrt{\xi(\mathbf{k})^2 + |\Delta(\mathbf{k})|^2}} \right). \tag{C.9}$$

Furthermore, it can be verified that the density distribution $n_{\mathbf{k}} = \langle \hat{a}^{\dagger}_{\mathbf{k}}\hat{a}_{\mathbf{k}} \rangle = |v_{\mathbf{k}}|^2$, and the order parameter $\Delta(\mathbf{k}) = \sum_{\mathbf{k}'}{}' \tilde{V}(\mathbf{k} - \mathbf{k}') u_{\mathbf{k}} v_{\mathbf{k}}$. The ground state is $|\text{BCS}\rangle = \prod_{\mathbf{k}} \left(u_{\mathbf{k}} + v_{\mathbf{k}}\hat{a}^{\dagger}_{\mathbf{k}}\hat{a}^{\dagger}_{-\mathbf{k}} \right) |0\rangle$, where $\gamma_{\mathbf{k}}$ denotes the quasi-particles excited from the Fermi sea that minimize the thermal potential.

Bibliography

1. Zhou, Y., Lesanovsky, I., Fernholz, T., *et al.* Controlling the dynamical scale factor in a trapped atom Sagnac interferometer. *Phys. Rev. A* **101,** 012517 (2020).
2. Zhou, Y., Li, Y., Nath, R., *et al.* Quench dynamics of Rydberg-dressed bosons on two-dimensional square lattices. *Phys. Rev. A* **101,** 013427 (2020).
3. Zhou, Y., Welch, N., Crawford, R., *et al.* Design of Magneto-optical Traps for Additive Manufacture by 3D Printing. arXiv: 1704.00430. (2017).
4. Saint, R., Evans, W., Zhou, Y., *et al.* 3D-printed components for quantum devices. *Sci. Rep.* **8,** 8368 (2018).
5. Lewenstein, M., You, L. & Cooper, J. Quantum Optics of a Bose-Einstein Condensate. *Acta Phys. Pol. A* **86,** 173 (1994).
6. Moore, M. G., Zobay, O. & Meystre, P. Quantum optics of a Bose-Einstein condensate coupled to a quantized light field. *Phys. Rev. A* **60,** 1491 (1999).
7. Jaksch, D. & Zoller, P. The cold atom Hubbard toolbox. *Ann. Phys.* **315,** 52 (2005).
8. Bloch, I., Dalibard, J. & Zwerger, W. Many-body physics with ultracold gases. *Rev. Mod. Phys.* **80,** 885 (2008).
9. Cronin, A. D., Schmiedmayer, J. & Pritchard, D. E. Optics and interferometry with atoms and molecules. *Rev. Mod. Phys.* **81,** 1051 (2009).
10. Bongs, K., Holynski, M., Vovrosh, J., *et al.* Taking atom interferometric quantum sensors from the laboratory to real-world applications. *Nat. Rev. Phys.* **1,** 731 (2019).
11. Jaksch, D., García-Ripoll, J. J., Cirac, J. I., *et al.* in *Quantum Inf.* 483 (Wiley, 2016).
12. Einstein, A. Quantentheorie des einatomigen idealen Gases. Zweite Abhandlung. *Sitzungsberichte der Preuss. Akad. der Wissenschaften (Berlin), Phys. Klasse,* 3 (1925).
13. Anderson, M. H., Ensher, J. R., Matthews, M. R., *et al.* Observation of Bose-Einstein Condensation in a Dilute Atomic Vapor. *Science* **269,** 198 (1995).
14. Bradley, C. C., Sackett, C. A., Tollett, J. J., *et al.* Evidence of Bose-Einstein Condensation in an Atomic Gas with Attractive Interactions. *Phys. Rev. Lett.* **75,** 1687 (1995).
15. Davis, K. B., Mewes, M. O., Andrews, M. R., *et al.* Bose-Einstein Condensation in a Gas of Sodium Atoms. *Phys. Rev. Lett.* **75,** 3969 (1995).

16. Chin, C., Grimm, R., Julienne, P., *et al.* Feshbach resonances in ultracold gases. *Rev. Mod. Phys.* **82,** 1225 (2010).
17. Einstein, A. Quantentheorie des einatomigen idealen Gases. *Sitzungsberichte der Preuss. Akad. der Wissenschaften (Berlin), Phys. Klasse,* 261 (1924).
18. Einstein, A. Quantentheorie des idealen Gases. *Sitzungsberichte der Preuss. Akad. der Wissenschaften (Berlin), Phys. Klasse,* 18 (1925).
19. Bose, S. N. Plancks Gesetz und Lichtquantenhypothese. *Zeitschrift für Phys.* **26,** 178 (1924).
20. Pathria, R. & Beale, P. D. *Statistical Mechanics* 3rd ed. (Academic Press, 2011).
21. Dalfovo, F., Giorgini, S., Pitaevskii, L. P., *et al.* Theory of Bose-Einstein condensation in trapped gases. *Rev. Mod. Phys.* **71,** 463 (1999).
22. Phillips, W. D. Nobel Lecture: Laser cooling and trapping of neutral atoms. *Rev. Mod. Phys.* **70,** 721 (1998).
23. Metcalf, H. J. & van der Straten, P. *Laser Cooling and Trapping* (Springer New York, New York, NY, 1999).
24. Metcalf, H. J. & van der Straten, P. in *Opt. Encycl.* (Wiley-VCH Verlag GmbH & Co. KGaA, Weinheim, Germany, 2007).
25. Pitaevskii, L. & Stringari, S. *Bose-Einstein Condensation and Superfluidity* (Oxford University Press, 2016).
26. Erdős, L., Schlein, B. & Yau, H.-T. Rigorous Derivation of the Gross-Pitaevskii Equation. *Phys. Rev. Lett.* **98,** 040404 (2007).
27. Pérez-García, V. M., Michinel, H, Cirac, J. I., *et al.* Low Energy Excitations of a Bose-Einstein Condensate: A Time-Dependent Variational Analysis. *Phys. Rev. Lett.* **77,** 5320 (1996).
28. Thomas, L. H. The calculation of atomic fields. *Math. Proc. Cambridge Philos. Soc.* **23,** 542 (1927).
29. Fermi, E. Un Metodo Statistic per la Determinazione di Alcune Paioriete dell' Atome. *Rend. dell Accad. del Lincei* **6,** 602 (1927).
30. Lifshitz, E. M. & Pitaevskii, L. P. *Statistical Physics: Theory of the Condensed State* (Butterworth-Heinemann, 1980).
31. Roth, R. & Burnett, K. Superfluidity and interference pattern of ultracold bosons in optical lattices. *Phys. Rev. A* **67,** 031602 (2003).
32. Damski, B, Zakrzewski, J, Santos, L, *et al.* Atomic Bose and Anderson Glasses in Optical Lattices. *Phys. Rev. Lett.* **91,** 080403 (2003).
33. Rokhsar, D. S. & Kotliar, B. G. Gutzwiller projection for bosons. *Phys. Rev. B* **44,** 10328 (1991).
34. Kühner, T. D. & Monien, H. Phases of the one-dimensional Bose-Hubbard model. *Phys. Rev. B* **58,** R14741 (1998).
35. Gao, F. & Han, L. Implementing the Nelder-Mead simplex algorithm with adaptive parameters. *Comput. Optim. Appl.* **51,** 259 (2012).
36. Jaksch, D, Bruder, C, Cirac, J. I., *et al.* Cold Bosonic Atoms in Optical Lattices. *Phys. Rev. Lett.* **81,** 3108 (1998).

37. Fisher, M. P., Weichman, P. B., Grinstein, G., *et al.* Boson localization and the superfluid-insulator transition. *Phys. Rev. B* **40,** 546 (1989).
38. Batrouni, G. G., Larson, B, Scalettar, R. T., *et al.* Universal conductivity in the two-dimensional boson Hubbard model. *Phys. Rev. B* **48,** 9628 (1993).
39. Scarola, V. W. & Das Sarma, S. Quantum Phases of the Extended Bose-Hubbard Hamiltonian: Possibility of a Supersolid State of Cold Atoms in Optical Lattices. *Phys. Rev. Lett.* **95,** 033003 (2005).
40. Iskin, M. & Freericks, J. K. Strong-coupling perturbation theory for the extended Bose-Hubbard model. *Phys. Rev. A* **79,** 053634 (2009).
41. Boudjemâa, A. & Shlyapnikov, G. V. Two-dimensional dipolar Bose gas with the roton-maxon excitation spectrum. *Phys. Rev. A* **87,** 025601 (2013).
42. Raventós, D., Graß, T., Lewenstein, M., *et al.* Cold bosons in optical lattices: a tutorial for exact diagonalization. *J. Phys. B* **50,** 113001 (2017).
43. Krauth, W. Quantum Monte Carlo Calculations for a Large Number of Bosons in a Harmonic Trap. *Phys. Rev. Lett.* **77,** 3695 (1996).
44. Anders, P., Gull, E., Pollet, L., *et al.* Dynamical mean-field theory for bosons. *New J. Phys.* **13,** 075013 (2011).
45. Kocharovsky, V. V., Kocharovsky, V. V. & Scully, M. O. Condensation of N bosons. III. Analytical results for all higher moments of condensate fluctuations in interacting and ideal dilute Bose gases via the canonical ensemble quasiparticle formulation. *Phys. Rev. A* **61,** 053606 (2000).
46. Sinatra, A., Lobo, C. & Castin, Y. The truncated Wigner method for Bose-condensed gases: limits of validity and applications. *J. Phys. B* **35,** 3599 (2002).
47. Gallagher, T. F. *Rydberg Atoms* (Cambridge University Press, 1994).
48. Balmer, J. J. Notiz über die Spectrallinien des Wasserstoffs. *Ann. Phys.* **261,** 80 (1885).
49. Bohr, N. I. On the constitution of atoms and molecules. *London, Edinburgh, Dublin Philos. Mag. J. Sci.* **26,** 1 (1913).
50. Rydberg, J. R. XXXIV. On the structure of the line-spectra of the chemical elements. *London, Edinburgh, Dublin Philos. Mag. J. Sci.* **29,** 331 (1890).
51. Marinescu, M., Sadeghpour, H. R. & Dalgarno, A. Dispersion coefficients for alkali-metal dimers. *Phys. Rev. A* **49,** 982 (1994).
52. Robicheaux, F., Hernández, J. V., Topçu, T., *et al.* Simulation of coherent interactions between Rydberg atoms. *Phys. Rev. A* **70,** 042703 (2004).
53. Simos, T. E. & Mousadis, G. A two-step method for the numerical solution of the radial Schrödinger equation. *Comput. Math. Appl.* **29,** 31 (1995).
54. Šibalić, N., Pritchard, J., Adams, C., *et al.* ARC: An open-source library for calculating properties of alkali Rydberg atoms. *Comput. Phys. Commun.* **220,** 319 (2017).
55. Robertson, E. J., Šibalić, N., Potvliege, R. M., *et al.* ARC 3.0: An expanded Python toolbox for atomic physics calculations. arXiv: 2007.12016. (2020).

56. Nguyen, T. L. *Study of dipole-dipole interaction between Rydberg atoms - Toward quantum simulation with Rydberg atoms* Thèse (Université Pierre et Marie Curie UPMC Paris VI, 2016).
57. Adams, C. S., Pritchard, J. D. & Shaffer, J. P. Rydberg atom quantum technologies. *J. Phys. B* **53,** 012002 (2019).
58. Bransden, B. H. & Joachain, C. J. *Physics of Atoms and Molecules* 2nd ed. (Pearson Education, 2003).
59. Hahn, Y. Polarizability of Rydberg atoms and the dominant long-range interactions. *Phys. Rev. A* **62,** 042703 (2000).
60. Jackson, J. *Classical electrodynamics* 3rd ed. (Wiley, New York, 1999).
61. Johnson, J. E. & Rolston, S. L. Interactions between Rydberg-dressed atoms. *Phys. Rev. A* **82,** 033412 (2010).
62. Balewski, J. B., Krupp, A. T., Gaj, A., *et al.* Rydberg dressing: understanding of collective many-body effects and implications for experiments. *New J. Phys.* **16,** 063012 (2014).
63. Aman, J. A., DeSalvo, B. J., Dunning, F. B., *et al.* Trap losses induced by near-resonant Rydberg dressing of cold atomic gases. *Phys. Rev. A* **93,** 043425 (2016).
64. Gaul, C, DeSalvo, B. J., Aman, J. A., *et al.* Resonant Rydberg Dressing of Alkaline-Earth Atoms via Electromagnetically Induced Transparency. *Phys. Rev. Lett.* **116,** 243001 (2016).
65. Clauser, J. F. Ultra-high sensitivity accelerometers and gyroscopes using neutral atom matter-wave interferometry. *Phys. B+C* **151,** 262 (1988).
66. Lenef, A., Hammond, T. D., Smith, E. T., *et al.* Rotation Sensing with an Atom Interferometer. *Phys. Rev. Lett.* **78,** 760 (1997).
67. Gustavson, T. L., Bouyer, P. & Kasevich, M. A. Precision Rotation Measurements with an Atom Interferometer Gyroscope. *Phys. Rev. Lett.* **78,** 2046 (1997).
68. Yao, Z. W., Lu, S. B., Li, R. B., *et al.* Continuous Dynamic Rotation Measurements Using a Compact Cold Atom Gyroscope. *Chinese Phys. Lett.* **33,** 083701 (2016).
69. Kasevich, M. & Chu, S. Measurement of the gravitational acceleration of an atom with a light-pulse atom interferometer. *Appl. Phys. B Photophysics Laser Chem.* **54,** 321 (1992).
70. Snadden, M., McGuirk, J., Bouyer, P, *et al.* Measurement of the Earth's Gravity Gradient with an Atom Interferometer-Based Gravity Gradiometer. *Phys. Rev. Lett.* **81,** 971 (1998).
71. Peters, A, Chung, K. Y. & Chu, S. High-precision gravity measurements using atom interferometry. *Metrologia* **38,** 25 (2001).
72. Hauth, M., Freier, C., Schkolnik, V., *et al.* First gravity measurements using the mobile atom interferometer GAIN. *Appl. Phys. B Lasers Opt.* **113,** 49 (2013).
73. Biedermann, G. W., Wu, X., Deslauriers, L., *et al.* Testing gravity with cold-atom interferometers. *Phys. Rev. A* **91,** 033629 (2015).

74. Barrett, B., Chan, I. & Kumarakrishnan, A. Atom-interferometric techniques for measuring uniform magnetic field gradients and gravitational acceleration. *Phys. Rev. A* **84,** 063623 (2011).

75. Milke, A., Kubelka-Lange, A., Gürlebeck, N., *et al.* Atom interferometry in space: Thermal management and magnetic shielding. *Rev. Sci. Instrum.* **85,** 083105 (2014).

76. Morinaga, A., Murakami, M., Nakamura, K., *et al.* Scalar Aharonov-Bohm Phase in Ramsey Atom Interferometry under Time-Varying Potential. *Atoms* **4,** 23 (2016).

77. Bertoldi, A., Lamporesi, G., Cacciapuoti, L., *et al.* Atom interferometry gravity-gradiometer for the determination of the Newtonian gravitational constant G. *Eur. Phys. J. D* **40,** 271 (2006).

78. Fixler, J. B., Foster, G. T., McGuirk, J. M., *et al.* Atom Interferometer Measurement of the Newtonian Constant of Gravity. *Science* **315,** 74 (2007).

79. Lamporesi, G., Bertoldi, A., Cacciapuoti, L., *et al.* Determination of the Newtonian Gravitational Constant Using Atom Interferometry. *Phys. Rev. Lett.* **100,** 050801 (2008).

80. Prevedelli, M., Cacciapuoti, L., Rosi, G., *et al.* Measuring the Newtonian constant of gravitation G with an atomic interferometer. *Philos. Trans. R. Soc. A* **372,** 20140030 (2014).

81. Dimopoulos, S., Graham, P. W., Hogan, J. M., *et al.* Testing General Relativity with Atom Interferometry. *Phys. Rev. Lett.* **98,** 111102 (2007).

82. Dimopoulos, S., Graham, P. W., Hogan, J. M., *et al.* General relativistic effects in atom interferometry. *Phys. Rev. D* **78,** 042003 (2008).

83. Dimopoulos, S., Graham, P. W., Hogan, J. M., *et al.* Gravitational wave detection with atom interferometry. *Phys. Lett. B* **678,** 37 (2009).

84. Hogan, J. M., Johnson, D. M. S., Dickerson, S., *et al.* An atomic gravitational wave interferometric sensor in low earth orbit (AGIS-LEO). *Gen. Relativ. Gravit.* **43,** 1953 (2011).

85. Cladé, P., de Mirandes, E., Cadoret, M., *et al.* Determination of the Fine Structure Constant Based on Bloch Oscillations of Ultracold Atoms in a Vertical Optical Lattice. *Phys. Rev. Lett.* **96,** 033001 (2006).

86. Cadoret, M., de Mirandes, E., Cladé, P., *et al.* Combination of Bloch Oscillations with a Ramsey-Bordé Interferometer: New Determination of the Fine Structure Constant. *Phys. Rev. Lett.* **101,** 230801 (2008).

87. Bordé, C. Atomic interferometry with internal state labelling. *Phys. Lett. A* **140,** 10 (1989).

88. Kasevich, M. & Chu, S. Atomic interferometry using stimulated Raman transitions. *Phys. Rev. Lett.* **67,** 181 (1991).

89. Riehle, F., Kisters, T., Witte, A., *et al.* Optical Ramsey spectroscopy in a rotating frame: Sagnac effect in a matter-wave interferometer. *Phys. Rev. Lett.* **67,** 177 (1991).

90. Gross, C., Zibold, T., Nicklas, E., *et al.* Nonlinear atom interferometer surpasses classical precision limit. *Nature* **464,** 1165 (2010).

91. Carnal, O. & Mlynek, J. Youngs double-slit experiment with atoms: A simple atom interferometer. *Phys. Rev. Lett.* **66,** 2689 (1991).

92. Keith, D. W., Ekstrom, C. R., Turchette, Q. A., *et al.* An interferometer for atoms. *Phys. Rev. Lett.* **66,** 2693 (1991).

93. Barrett, B., Geiger, R., Dutta, I., *et al.* The Sagnac effect: 20 years of development in matter-wave interferometry. *Comptes Rendus Phys.* **15,** 875 (2014).

94. Zobay, O. & Garraway, B. M. Two-Dimensional Atom Trapping in Field-Induced Adiabatic Potentials. *Phys. Rev. Lett.* **86,** 1195 (2001).

95. Lesanovsky, I., Schumm, T., Hofferberth, S., *et al.* Adiabatic radio-frequency potentials for the coherent manipulation of matter waves. *Phys. Rev. A* **73,** 033619 (2006).

96. Lesanovsky, I. & von Klitzing, W. Time-Averaged Adiabatic Potentials: Versatile Matter-Wave Guides and Atom Traps. *Phys. Rev. Lett.* **99,** 083001 (2007).

97. Gildemeister, M., Nugent, E., Sherlock, B. E., *et al.* Trapping ultracold atoms in a time-averaged adiabatic potential. *Phys. Rev. A* **81,** 031402 (2010).

98. Sherlock, B. E., Gildemeister, M., Owen, E., *et al.* Time-averaged adiabatic ring potential for ultracold atoms. *Phys. Rev. A* **83,** 043408 (2011).

99. Navez, P, Pandey, S, Mas, H, *et al.* Matter-wave interferometers using TAAP rings. *New J. Phys.* **18,** 075014 (2016).

100. Sakurai, J. J. Comments on quantum-mechanical interference due to the Earth's rotation. *Phys. Rev. D* **21,** 2993 (1980).

101. Rizzi, G. & Ruggiero, M. L. The Sagnac Phase Shift Suggested by the Aharonov-Bohm Effect for Relativistic Matter Beams. *Gen. Relativ. Gravit.* **35,** 1745 (2003).

102. Salasnich, L., Parola, A. & Reatto, L. Effective wave equations for the dynamics of cigar-shaped and disk-shaped Bose condensates. *Phys. Rev. A* **65,** 043614 (2002).

103. Egorov, M., Opanchuk, B., Drummond, P., *et al.* Measurement of s-wave scattering lengths in a two-component Bose-Einstein condensate. *Phys. Rev. A* **87,** 053614 (2013).

104. Ragole, S. & Taylor, J. M. Interacting Atomic Interferometry for Rotation Sensing Approaching the Heisenberg Limit. *Phys. Rev. Lett.* **117,** 203002 (2016).

105. Stevenson, R., Hush, M., Bishop, T., *et al.* Sagnac interferometry with a single atomic clock. *Phys. Rev. Lett.* **115,** 163001 (2015).

106. Boeringer, D. W. & Werner, D. H. *Particle swarm optimization of a modified Bernstein polynomial for conformal array excitation synthesis* in *IEEE Antennas Propag. Soc. Symp. 2004.* (IEEE, 2004), 2293.

107. Bao, W., Jaksch, D. & Markowich, P. A. Numerical solution of the Gross–Pitaevskii equation for Bose–Einstein condensation. *J. Comput. Phys.* **187,** 318 (2003).

108. Bao, W., Jin, S. & Markowich, P. A. Numerical Study of Time-Splitting Spectral Discretizations of Nonlinear Schrödinger Equations in the Semiclassical Regimes. *SIAM J. Sci. Comput.* **25,** 27 (2003).

109. Frigo, M. & Johnson, S. The Design and Implementation of FFTW3. *Proc. IEEE* **93,** 216 (2005).

110. Auzinger, W., Kassebacher, T., Koch, O., *et al.* Adaptive splitting methods for nonlinear Schrödinger equations in the semiclassical regime. *Numer. Algorithms* **72,** 1 (2016).

111. Wang, H. A time-splitting spectral method for coupled Gross-Pitaevskii equations with applications to rotating Bose-Einstein condensates. *J. Comput. Appl. Math.* **205,** 88 (2007).

112. Thalhammer, M., Caliari, M. & Neuhauser, C. High-order time-splitting Hermite and Fourier spectral methods. *J. Comput. Phys.* **228,** 822 (2009).

113. Bloch, I. Ultracold quantum gases in optical lattices. *Nat. Phys.* **1,** 23 (2005).

114. Greiner, M. & Fölling, S. Condensed-matter physics: Optical lattices. *Nature* **453,** 736 (2008).

115. Lewenstein, M., Sanpera, A., Ahufinger, V., *et al.* Ultracold atomic gases in optical lattices: Mimicking condensed matter physics and beyond. *Adv. Phys.* **56,** 243 (2007).

116. Greiner, M., Mandel, O., Esslinger, T., *et al.* Quantum phase transition from a superfluid to a mott insulator in a gas of ultracold atoms. *Nature* **415,** 39 (2002).

117. Kashurnikov, V. A., Prokof'ev, N. V. & Svistunov, B. V. Revealing the superfluid–Mott-insulator transition in an optical lattice. *Phys. Rev. A* **66,** 031601 (2002).

118. Sengupta, P., Pryadko, L. P., Alet, F., *et al.* Supersolids versus Phase Separation in Two-Dimensional Lattice Bosons. *Phys. Rev. Lett.* **94,** 207202 (2005).

119. Scarola, V. W., Demler, E. & Das Sarma, S. Searching for a supersolid in cold-atom optical lattices. *Phys. Rev. A* **73,** 051601 (2006).

120. Yi, S., Li, T. & Sun, C. P. Novel Quantum Phases of Dipolar Bose Gases in Optical Lattices. *Phys. Rev. Lett.* **98,** 260405 (2007).

121. Keilmann, T., Cirac, I. & Roscilde, T. Dynamical Creation of a Supersolid in Asymmetric Mixtures of Bosons. *Phys. Rev. Lett.* **102,** 255304 (2009).

122. Iskin, M. Route to supersolidity for the extended Bose-Hubbard model. *Phys. Rev. A* **83,** 051606 (2011).

123. Li, W., Hamadeh, L. & Lesanovsky, I. Probing the interaction between Rydberg-dressed atoms through interference. *Phys. Rev. A* **85,** 053615 (2012).

124. Landig, R., Hruby, L., Dogra, N., *et al.* Quantum phases from competing short- and long-range interactions in an optical lattice. *Nature* **532,** 476 (2016).

125. Léonard, J., Morales, A., Zupancic, P., *et al.* Supersolid formation in a quantum gas breaking a continuous translational symmetry. *Nature* **543,** 87 (2017).

126. Li, J.-R., Lee, J., Huang, W., *et al.* A stripe phase with supersolid properties in spin-orbit-coupled Bose-Einstein condensates. *Nature* **543,** 91 (2017).

127. Li, Y., Geißler, A., Hofstetter, W., *et al.* Supersolidity of lattice bosons immersed in strongly correlated Rydberg dressed atoms. *Phys. Rev. A* **97,** 023619 (2018).

128. Wu, B. & Niu, Q. Superfluidity of Bose-Einstein condensate in an optical lattice: Landau-Zener tunnelling and dynamical instability. *New J. Phys.* **5,** 104 (2003).

129. Tomadin, A., Mannella, R. & Wimberger, S. Many-body Landau-Zener tunneling in the Bose-Hubbard model. *Phys. Rev. A* **77,** 013606 (2008).

130. Deng, H., Dai, H., Huang, J., *et al.* Cluster Gutzwiller study of the Bose-Hubbard ladder: Ground-state phase diagram and many-body Landau-Zener dynamics. *Phys. Rev. A* **92,** 023618 (2015).

131. Zurek, W. H., Dorner, U. & Zoller, P. Dynamics of a Quantum Phase Transition. *Phys. Rev. Lett.* **95,** 105701 (2005).

132. Dziarmaga, J., Tylutki, M. & Zurek, W. H. Quench from Mott insulator to superfluid. *Phys. Rev. B* **86,** 144521 (2012).

133. Del Campo, A. & Zurek, W. H. Universality of phase transition dynamics: Topological defects from symmetry breaking. *Int. J. Mod. Phys. A* **29,** 1430018 (2014).

134. Shimizu, K., Kuno, Y., Hirano, T., *et al.* Dynamics of a quantum phase transition in the Bose-Hubbard model: Kibble-Zurek mechanism and beyond. *Phys. Rev. A* **97,** 033626 (2018).

135. Shimizu, K., Hirano, T., Park, J., *et al.* Dynamics of first-order quantum phase transitions in extended Bose-Hubbard model: from density wave to superfluid and vice versa. *New J. Phys.* **20,** 083006 (2018).

136. Shimizu, K., Hirano, T., Park, J., *et al.* Out-of-equilibrium dynamics of multiple second-order quantum phase transitions in an extended Bose-Hubbard model: Superfluid, supersolid, and density wave. *Phys. Rev. A* **98,** 063603 (2018).

137. Weiss, W., Gerster, M., Jaschke, D., *et al.* Kibble-Zurek scaling of the one-dimensional Bose-Hubbard model at finite temperatures. *Phys. Rev. A* **98,** 063601 (2018).

138. Scherg, S, Kohlert, T, Herbrych, J, *et al.* Nonequilibrium Mass Transport in the 1D Fermi-Hubbard Model. *Phys. Rev. Lett.* **121,** 130402 (2018).

139. Brown, P. T., Mitra, D., Guardado-Sanchez, E., *et al.* Bad metallic transport in a cold atom Fermi-Hubbard system. *Science* **363,** 379 (2019).

140. Fujiwara, C. J., Singh, K., Geiger, Z. A., *et al.* Transport in Floquet-Bloch Bands. *Phys. Rev. Lett.* **122,** 010402 (2019).

141. Léonard, J., Morales, A., Zupancic, P., *et al.* Monitoring and manipulating Higgs and Goldstone modes in a supersolid quantum gas. *Science* **358,** 1415 (2017).

142. Di Liberto, M., Recati, A., Trivedi, N., *et al.* Particle-Hole Character of the Higgs and Goldstone Modes in Strongly Interacting Lattice Bosons. *Phys. Rev. Lett.* **120,** 073201 (2018).

143. Gutzwiller, M. C. Effect of Correlation on the Ferromagnetism of Transition Metals. *Phys. Rev. Lett.* **10,** 159 (1963).

144. Gutzwiller, M. C. Correlation of Electrons in a Narrow *s* Band. *Phys. Rev.* **137,** A1726 (1965).

145. Haldane, F. D. M. Exact Jastrow-Gutzwiller resonating-valence-bond ground state of the spin-$\frac{1}{2}$ antiferromagnetic Heisenberg chain with $1/r^2$ exchange. *Phys. Rev. Lett.* **60,** 635 (1988).

146. Shastry, B. S. Exact solution of an S =1/2 Heisenberg antiferromagnetic chain with long-ranged interactions. *Phys. Rev. Lett.* **60,** 639 (1988).

147. Bünemann, J., Gebhard, F. & Thul, R. Landau-Gutzwiller quasiparticles. *Phys. Rev. B* **67,** 075103 (2003).

148. Krauth, W., Caffarel, M. & Bouchaud, J.-P. Gutzwiller wave function for a model of strongly interacting bosons. *Phys. Rev. B* **45,** 3137 (1992).

149. Sheshadri, K, Krishnamurthy, H. R, Pandit, R, *et al.* Superfluid and Insulating Phases in an Interacting-Boson Model: Mean-Field Theory and the RPA. *Europhys. Lett.* **22,** 257 (1993).

150. Bandyopadhyay, S., Bai, R., Pal, S., *et al.* Quantum phases of canted dipolar bosons in a two-dimensional square optical lattice. *Phys. Rev. A* **100,** 053623 (2019).

151. Rey, A. M., Burnett, K., Roth, R., *et al.* Bogoliubov approach to superfluidity of atoms in an optical lattice. *J. Phys. B* **36,** 825 (2003).

152. Macrì, T., Maucher, F., Cinti, F., *et al.* Elementary excitations of ultracold soft-core bosons across the superfluid-supersolid phase transition. *Phys. Rev. A* **87,** 061602 (2013).

153. Hsueh, C.-H., Lin, T.-C., Horng, T.-L., *et al.* Quantum crystals in a trapped Rydberg-dressed Bose-Einstein condensate. *Phys. Rev. A* **86,** 013619 (2012).

154. Kibble, T. W. B. Topology of cosmic domains and strings. *J. Phys. A. Math. Gen.* **9,** 1387 (1976).

155. Zurek, W. H. Cosmological experiments in superfluid helium? *Nature* **317,** 505 (1985).

156. Dziarmaga, J. & Zurek, W. H. Quench in the 1D Bose-Hubbard model: Topological defects and excitations from the Kosterlitz-Thouless phase transition dynamics. *Sci. Rep.* **4,** 5950 (2015).

157. Baier, S., Mark, M. J., Petter, D., *et al.* Extended Bose-Hubbard models with ultracold magnetic atoms. *Science* **352,** 201 (2016).

158. Van Oosten, D., van der Straten, P. & Stoof, H. T. C. Quantum phases in an optical lattice. *Phys. Rev. A* **63,** 053601 (2001).

159. Elstner, N & Monien, H. Dynamics and thermodynamics of the Bose-Hubbard model. *Phys. Rev. B* **59,** 12184 (1999).

160. Hohenadler, M, Aichhorn, M, Schmidt, S, *et al.* Dynamical critical exponent of the Jaynes-Cummings-Hubbard model. *Phys. Rev. A* **84,** 041608 (2011).

161. Toth, E, Rey, A. M. & Blakie, P. B. Theory of correlations between ultracold bosons released from an optical lattice. *Phys. Rev. A* **78,** 013627 (2008).

162. Fölling, S., Gerbier, F., Widera, A., *et al.* Spatial quantum noise interferometry in expanding ultracold atom clouds. *Nature* **434,** 481 (2005).

163. Rom, T, Best, T., Van Oosten, D., *et al.* Free fermion antibunching in a degenerate atomic Fermi gas released from an optical lattice. *Nature* **444,** 733 (2006).

164. Keil, M., Amit, O., Zhou, S., *et al.* Fifteen years of cold matter on the atom chip: promise, realizations, and prospects. *J. Mod. Opt.* **63,** 1840 (2016).

165. Pritchard, D. E. Cooling neutral atoms in a magnetic trap for precision spectroscopy. *Phys. Rev. Lett.* **51,** 1336 (1983).

166. Helmerson, K., Martin, A. & Pritchard, D. E. Laser cooling of magnetically trapped neutral atoms. *J. Opt. Soc. Am. B* **9,** 1988 (1992).

167. Santandréa, L. & Le Bihan, Y. *Using COMSOL-Multiphysics in Eddy Current Non Destructive Testing Context* in *COMSOL Conf. PARIS* (PARIS, France, 2010), 3576.

168. Baranova, V. E. & Baranov, P. F. *The Helmholtz coils simulating and improved in COMSOL* in *2014 Dyn. Syst. Mech. Mach.* (IEEE, 2014), 1.

169. Reeve, W. D. *Subscriber Loop Signaling and Transmission Handbook* eng (ed IEEE Communications Society) (IEEE, Piscataway, NJ : New York, 1995).

170. Corcoran, J & Nagy, P. B. Compensation of the Skin Effect in Low-Frequency Potential Drop Measurements. *J. Nondestruct. Eval.* **35,** 58 (2016).

171. Oganesyan, V., Kivelson, S. A. & Fradkin, E. Quantum theory of a nematic Fermi fluid. *Phys. Rev. B* **64,** 195109 (2001).

172. Kinnunen, J. J., Baarsma, J. E., Martikainen, J.-P., *et al.* The Fulde-Ferrell-Larkin-Ovchinnikov state for ultracold fermions in lattice and harmonic potentials: a review. *Rep. Prog. Phys.* **81,** 046401 (2018).

173. Li, W.-H., Hsieh, T.-C., Mou, C.-Y., *et al.* Emergence of a Metallic Quantum Solid Phase in a Rydberg-Dressed Fermi Gas. *Phys. Rev. Lett.* **117,** 035301 (2016).

174. Ronen, S. & Bohn, J. L. Zero sound in dipolar Fermi gases. *Phys. Rev. A* **81,** 033601 (2010).

175. Chan, C.-K., Wu, C., Lee, W.-C., *et al.* Anisotropic-Fermi-liquid theory of ultracold fermionic polar molecules: Landau parameters and collective modes. *Phys. Rev. A* **81,** 023602 (2010).

176. Aikawa, K., Baier, S., Frisch, A., *et al.* Observation of Fermi surface deformation in a dipolar quantum gas. *Science* **345,** 1484 (2014).

177. Keleş, A., Zhao, E. & Li, X. f-wave superfluidity from repulsive interaction in Rydberg-dressed Fermi gas. *Phys. Rev. A* **101,** 023624 (2020).

178. Kittel, C. *Introduction to Solid State Physics* 8th ed. (Wiley, 2004).

179. Zhao, C., Jiang, L., Liu, X., *et al.* Hartree-Fock-Bogoliubov theory of dipolar Fermi gases. *Phys. Rev. A* **81,** 063642 (2010).